



Università degli Studi di Salerno

FACOLTÀ DI SCIENZE MATEMATICHE, FISICHE E NATURALI

Dipartimento di Fisica “E.R. Caianiello”

Dottorato di Ricerca in Fisica

X Ciclo, II Serie

**Interplay of spin-orbital correlations and
structural distortions in Ru- and Cr- based
perovskite systems**

Thesis submitted for the degree of Doctor Philosophiae

Candidate
Dr. Carmine Autieri

Supervisor
Prof. Canio Noce

Dr. Mario Cuoco

Coordinator
Prof. Giuseppe Grella

ACADEMIC YEAR 2011/2012

Contents

1	Introduction	1
2	Metamagnetism of itinerant electrons: theory and effective models	7
2.1	Introduction	7
2.2	Mean-field theory of itinerant uniform ferro/metamagnetism	9
2.2.1	The Stoner criterion and its generalization	12
2.2.2	<i>QCEP</i> and effect of the temperature on susceptibility	14
2.3	Effective models	16
2.3.1	The M^6 theory	16
2.3.2	The one-dimensional density of state	19
2.4	Conclusions	24
3	Collective properties of eutectic ruthenates: role of nanometric inclusions	26
3.1	Introduction	26
3.2	Model	29
3.3	Results	35
3.4	Conclusions	41

4	Metamagnetism of itinerant electrons: the realistic case of multy-layer ruthenates	45
4.1	Introduction	45
4.2	Metamagnetism in three band Hubbard model	46
4.3	$M(U)$ for ruthenates, role of Hubbard repulsion	49
4.3.1	Metamagnetic properties of pure phases	49
4.3.2	Magnetization at interface	52
4.4	Conclusions	54
5	Ab-initio study of the interface properties $\text{Sr}_2\text{RuO}_4/\text{Sr}_3\text{Ru}_2\text{O}_7$	56
5.1	Introduction	56
5.2	Computational details	58
5.3	Results	58
5.3.1	Bulk Sr_2RuO_4 phase	59
5.3.2	Bulk $\text{Sr}_3\text{Ru}_2\text{O}_7$ phase	60
5.3.3	Sr_2RuO_4 - $\text{Sr}_3\text{Ru}_2\text{O}_7$ hybrid structures	62
5.4	Conclusions	67
6	First principles study of KCrF_3	68
6.1	Introduction	68

6.2	Crystal structures and magnetism	69
6.3	Computational details: <i>DFT</i> , <i>PAW</i> and <i>LSDA + U</i>	71
6.4	Ground state, orbital order and magnetic properties	72
6.5	Volume relax	76
6.5.1	<i>LDA</i>	76
6.5.2	<i>LSDA</i> and <i>LSDA + U</i>	78
6.5.3	High volume	79
6.5.4	The hypothetical ferromagnetic phase	79
6.6	Conclusions	79
7	Calculation of model Hamiltonian parameters for KCrF_3	81
7.1	Introduction	81
7.2	e_g basis	83
7.2.1	Tetragonal phase	84
7.2.2	Monoclinic phase	85
7.2.3	Cubic phase	86
7.3	The <i>MLWF</i> basis	87
7.3.1	Tetragonal phase	88
7.3.2	Monoclinic phase	89

7.4	Cococcioni method	91
7.5	Spin-orbit coupling and magnetic anisotropy	91
7.6	Conclusions	92
8	Orbital order and ferromagnetism in $\text{LaMn}_{1-x}\text{Ga}_x\text{O}_3$	93
8.1	Introduction	93
8.2	Computational details	94
8.3	The ab-initio study of the electronic and structural properties of $\text{LaMn}_{1-x}\text{Ga}_x\text{O}_3$	96
8.3.1	Octahedral Distortion	96
8.3.2	Density of states	98
8.3.3	Orbital order	98
8.4	Magnetism	102
8.4.1	Low concentration of Ga	102
8.4.2	Intermediate concentration of Ga	103
8.5	Conclusions	105
9	Conclusions	106
	Acknowledgement	109
A	Properties of one-dimensional density of state	110

B Gibbs free energy of the one-dimensional Hubbard model in mean field approximation	111
---	------------

1 Introduction

The transition metal oxides (*TMO*) are emerging as the natural playground where the intriguing effects induced by electron correlations can be addressed. Since the s electron of the transition metals are transferred to the oxygen ions, the remaining electrons near the Fermi level have strongly correlated d character and are responsible for the physical properties of *TMO*. These electron correlations, together with dimensionality and relativistic effect, play a crucial role in the formation and the competition of different electronic, magnetic and structural phases, giving rise to a rich phase diagram: Mott insulators, charge, spin and orbital orderings, metal-insulator transitions, multiferroics and superconductivity [1, 2]. The investigation of *TMO* correlated electron physics usually refers to 3d *TMO*, mainly because of high-temperature superconductivity in the cuprates and in the iron-pnictides, and colossal magneto-resistance in manganites, but also because the highly extended 4d-shells would a priori suggest a weaker ratio between the intra-atomic Coulomb interaction and the electron bandwidth. Nevertheless, the extension of the 4d-shells also points towards a strong coupling between the 4d-orbitals and the neighbouring oxygen orbitals, implying that these TMO have the tendency to form distorted structure with respect to the ideal one. As a consequence, the change in the M-O-M bond angle often leads to a narrowing of the d -bandwidth, bringing the system on the verge of a metal-insulator transition or into an insulating state. Hence, 4d materials share common features with 3d systems having additionally a significant sensitivity of the electronic states to the lattice structure, effective dimensionality and, most importantly, to relativistic effects due to stronger spin-orbit coupling.

Recently, the increased capability to construct oxide heterostructures [3], and technical achievements in the nanometre-scale synthesis improved the possibility to explore the above mentioned properties but also new phenomena that may emerge at interface, opening too the possibility to make new devices [4]. Furthermore, the different symmetry, the reconstruction of the charge, spin and orbital states at interfaces produce new phenomena not always found in the bulk. Moreover, also the two-dimensionality of this kind of systems enhances the effects of electron correlations by reducing the kinetic energy electrons. As an example, it is known that at the interfaces new magnetism and new gauge structures can appear. A natural starting point to study the heterostructures is to determine their configuration at interfaces. For instance, a charge transfer is observed, if the planes parallel to the interface have different charge. In this case, the charge transfers to equilibrate the electron

chemical interface potential, leading to interface screening in metals. The region over which the local carrier density varies can traverse entire phase diagrams, spanning metallic, magnetic and superconducting phases. The rearrangement of charge at oxide interfaces is driven primarily by electrostatic interactions, if is present. Because of the strong correlation between charge, spin and orbital degrees of freedom, modulations of the charge density in *TMO* can lead to spin or orbital polarization. Another source of orbital and spin polarization in oxide heterostructures is the epitaxial strain resulting from the mismatch of the two lattice parameters of the two *TMO* constituents. In analogy to the size mismatch between anions and cations in bulk TMO, this strain is accommodated by a combination of uniform deformations and staggered rotations of the metal-oxide octahedra in perovskite compound, which influence the orbital occupation through the crystal field. The lattice deformations resulting from epitaxial strain are present in all the heterostructures. However, unlike the charge-driven reconstructions discussed above, which can be effectively screened at least in metallic or highly polarizable dielectric *TMO*, the strain-driven spin and orbital polarization has a spatial range of tens of nanometres.

The main purpose of this thesis is a study of the mechanisms and the fundamental interactions that control the formation and the competition of different magnetic and structural phase driven by the electronic correlations, dimensionality and relativistic effects in Ru-, Cr- and Mn- based perovskite systems, also considering what happens in hybrid or eutectic structures.

Ruthenium oxide based perovskite materials are quite unique in the realm of oxides because their properties change drastically as a function of the number of RuO_2 layers and the way spin-orbital and lattice degrees of freedom get coupled to each other. The number n of RuO_2 layers in the unit cell of the Ruddlesden-Popper family $A_{n+1}\text{Ru}_n\text{O}_{3n+1}$ [$A=\text{Sr}, \text{Ca}$ with $n=1,2,\dots$,] of perovskite materials, indeed, represents a critical parameter for obtaining distinct collective phenomena as spin triplet chiral superconductivity, anisotropic metamagnetism, coexisting ferro/metamagnetism, orbital selective Mottness, as well as complex spin-orbital correlated states exhibiting colossal magnetoresistance (*CMR*) behaviour. The role played by the purity of the single crystal ruthenate samples is crucial for determining their physical properties. In typical oxide perovskite materials, the transition metal ions are surrounded by oxygen ions forming octahedra. In the ruthenates the deformations and relative orientations of these corner-shared octahedra is depending on the number of RuO_2 layers and in turn determines the crystalline-field splitting, the band structure, and hence the magnetic and transport properties. As a result, the $\text{Sr}_{n+1}\text{Ru}_n\text{O}_{3n+1}$ are

metallic and tend to be ferromagnetic or metamagnetic with the exception of the $n=1$ member that is a spin triplet superconductor [5], whereas the isoelectronic $Ca_{n+1}Ru_nO_{3n+1}$, with Ca replacing the larger Sr, tends to be at the verge of a metal-insulator transition and prone to antiferromagnetism and orbital ordering. Furthermore, the Curie temperature T_C in the $Sr_{n+1}Ru_nO_{3n+1}$ increases with n , whereas the Néel temperature, T_N , in the $Ca_{n+1}Ru_nO_{3n+1}$ decreases with increasing n . In all these systems we have an intricate behaviour emerging from multi-orbitals layered correlated systems. The possibility of synthesizing eutectic systems, as naturally occurring mesoscopic and nanoscopic interfaces, has opened novel routes for functionalities based on the potential tuning of quantum collective properties. Indeed, the modification of the pairing wave function in the proximity of normal or magnetic systems as well as that of the quantum configurations and the collective phenomena that might emerge at the interface between the embedded phases may lead to exotic quantum phases. The main drive behind eutectic growth is given by the possibility of developing composite materials with distinct properties from those of the pure constituents. In this case, the presence of one phase embedding in another phase is not considered a random impurity but a correlated impurity, that permits the emerging of eventual new properties of the system. In all the elements of the Ruddlesden-Popper series, the Ruthenium is in the form Ru^{4+} with four electrons in the 4d shell. This is the same configuration of the manganese in $LaMnO_3$ and the chromium in $KCrF_3$, but the stronger electronic correlations of the 3d shell giving rise to high spin configuration at low temperature. In perovskite manganite oxides, the particular physical properties of the *CMR* materials are related to the fact that their parent compound $LaMnO_3$ contains Mn^{3+} ions. On the one hand, the presence of these Jahn-Teller active ions leads to a strong coupling between the electrons and the lattice, giving rise to polaron formation which is widely perceived to be essential for the *CMR* effect. On the other hand, when doped, the d^4 high spin state leads, via the double exchange mechanism, to a ferromagnetic metallic state with a large magnetic moment, making the system easily susceptible to externally applied magnetic fields. The presence of strong electron correlations and an orbital degree of freedom, to which the Jahn-Teller effect is directly related, adds to the complexity and gives rise to an extraordinarily rich phase diagram, displaying a wealth of spin, charge, orbital, and magnetically ordered phases. Formally, high spin Cr^{2+} is electronically equivalent to Mn^{3+} , however, due to its low ionization potential divalent Cr^{2+} is rarely found in solid state systems. $KCrF_3$ is a rare and intriguing example, revealing strong structural, electronic, and magnetic similarities with $LaMnO_3$ including the presence of Jahn-Teller distortions, orbital ordering and orbital melting at high temperature. It was estimated that electronic correlations are bigger in $KCrF_3$ re-

spect to LaMnO_3 . This observation is an indication that the monoclinic-tetragonal transition can be driven from electronic correlation, differently from LaMnO_3 where Jahn-Teller effect is fundamental. Also, the LaMnO_3 doped with gallium presents a reduced Jahn-Teller effect. The interplay of spin-orbital correlations, structural distortions and the correlation between the gallium impurity make emerging a new ferromagnetic ground state at intermediate concentration.

Take in account all the degrees of freedom of these compound it is a very difficult task. Nevertheless, we have found that Density Functional Theory (*DFT*) [6] and many body theory [7] may be used in a clever way to capture the relevant physics of *TMO*. We recall that the *DFT* allows for an evaluation from first principles of the proprieties of these systems, while the model Hamiltonian approach permits to stress the crucial role of the electronic correlation. From a methodological point of view, we have applied ab-initio approaches using plane wave codes [8, 9, 10] for the bulk systems and heterostructures to analyse the electronic structure and also the magnetic and orbital order. Although one of the simplest approach is the generalized gradient approximation (*GGA*), the large part of this thesis is developed within techniques going beyond *GGA*. Furthermore, we have used many-body techniques (based on multi-orbitals Hamiltonian) to describe itinerant electrons on the verge of magnetic or superconducting instabilities both for bulk and inhomogenous systems. In the attempt to describe the low-energy physics in a way that combine the ab-initio with many-body approaches, we have used the maximally-localised Wannier functions the extract the effective tight-binding Hamiltonian.

The dissertation is arranged as follows. In Chapter 2-5 we study the phenomena at interface Sr_2RuO_4 - $\text{Sr}_3\text{Ru}_2\text{O}_7$, and the results obtained are compared with the bulk case. In Chapter 6-8 we study the interplay between the spin-orbital correlations and the structural distortions in bulk perovskite systems. Each chapter is organized as follows: an abstract, an introduction, the results, the discussion and the conclusions.

In particular, in Chapter 2, the mean field theory of itinerant uniform ferro/ metamagnetism and its consequences are introduced. We present two analytically solvable models: the M^6 Landau theory and the full analytical solution of one-dimensional tight binding density of state. We compute the analytical thermodynamic functional, the phase diagram, the quantum critical endpoint and the critical magnetic field. Necessary and sufficient conditions to have itinerant metamagnetism are examined.

In Chapter 3, we want to analyse the interface Sr_2RuO_4 - $\text{Sr}_3\text{Ru}_2\text{O}_7$. We study the

modification of the electronic structure induced by nanometric inclusions of Sr_2RuO_4 embedded as c -axis stacking fault in $\text{Sr}_3\text{Ru}_2\text{O}_7$ and viceversa. The change of the density of states near the Fermi level is investigated as a function of the electron density, the strength of the charge transfer at the interfaces between the inclusion and the host, and of the distance from the inclusion. Then, we examine how the tendency towards long range orders is affected by the presence of the nanometric inclusions. This is done by looking at the basic criteria for broken symmetry states such as superconductivity, ferromagnetism and metamagnetism. We show that, according to the strength of the charge transfer coupling, the ordered phases may be enhanced or hindered, as a consequence of the interplay between the host and the inclusion, and we clarify the role played by the orbital degree of freedom showing an orbital selective behaviour within the t_{2g} bands. A discussion on the connections between the theoretical outcome and the experimental observations is also presented.

Chapter 4 has the scope to study the effect of electronic correlation at interface Sr_2RuO_4 - $\text{Sr}_3\text{Ru}_2\text{O}_7$. We study in detail the role of the electronic correlation in systems based on nanometric inclusions of Sr_2RuO_4 embedded as c -axis stacking fault in $\text{Sr}_3\text{Ru}_2\text{O}_7$ and viceversa. The metamagnetic properties in mean field theory approach using the realistic density of state are analyzed.

In Chapter 5, the main topic is the analysis of the electronic reconstruction at the interface Sr_2RuO_4 - $\text{Sr}_3\text{Ru}_2\text{O}_7$. We study the fermiology of Sr_2RuO_4 and $\text{Sr}_3\text{Ru}_2\text{O}_7$ from first principles: comparison, main features and calculation of effective hopping Ru-Ru are performed. Effect of the octahedral rotation and dimensionality are analyzed studying ab-initio the interface Sr_2RuO_4 - $\text{Sr}_3\text{Ru}_2\text{O}_7$. We show that the rotations strongly reduce the main hopping parameter of the d_{xy} band, making near the Van Hove singularity to the Fermi level.

In Chapter 6, we study the tetragonal-monoclinic transition in the compound KCrF_3 . We present the electronic structure and the volume relaxation study for the KCrF_3 in the two different crystalline phases. Following the usual definition of the e_g orbital $|\theta\rangle = \cos\frac{\theta}{2}|3z^2-1\rangle + \sin\frac{\theta}{2}|x^2-y^2\rangle$, the calculation of the orbital gives $\theta = 110.5^\circ$ for the tetragonal structure, that is similar to LaMnO_3 . For the monoclinic phase, we find $\theta = 120.9^\circ$ and 102.2° for the two types of octahedron. We discuss similarities with KCuF_3 and LaMnO_3 in the orbital order.

In Chapter 7, we deepen the study of KCrF_3 studying the low-energy physics and the non-collinear properties of its antiferromagnetic ground state. We present and

compare the hopping parameters for the cubic, tetragonal and monoclinic structures of KCrF_3 using the e_g basis and the Maximally localised Wannier functions. Moreover, we analyse the strength of electronic correlation using the Cococcioni method based on linear response approach. Although, the atomic number of chromium is relatively small, it is observed experimentally that the spin-orbit effect can play a non trivial role at low temperature. We go beyond the spin collinear approximation, the spin-orbit coupling and the weak ferromagnetism are also examined.

In Chapter 8, we study from first principles the magnetic, electronic, orbital and structural properties of the LaMnO_3 doped with gallium atoms. The gallium atoms reduce the Jahn-Teller effect, and accordingly reduce the charge gap. Surprisingly, the system does not go towards a metallic phase. The doping tends to reduce the orbital order by weakening the antiferromagnetic phase and by favoring an unusual insulating ferromagnetic phase due to the effect of the correlated disorder.

The final chapter contains a general discussion on the results obtained and some comments on prospective and open questions.

2 Metamagnetism of itinerant electrons: theory and effective models

The mean field theory of itinerant uniform ferro/metamagnetism and its consequences are introduced. We present two analytically solvable models: the M^6 Landau theory and the full analytical solution of one-dimensional tight binding density of state. We compute the analytical thermodynamic functional, the phase diagram, the quantum critical endpoint and the critical magnetic field. Necessary and sufficient conditions to have itinerant metamagnetism are examined.

2.1 Introduction

Most of the non-magnetic materials are Pauli paramagnets and their magnetization presents a linear behaviour in applied magnetic field. Nevertheless non linear effects occur. This property is observed when the system is near to two different possible configurations for its ground state. The transition that happens when there is a superlinear behaviour (or a jump at $T = 0$) in the magnetization is called metamagnetic transition. The magnetic field induces a crossover in the system from the ground state to another state close in energy, the abrupt change of ground state strongly modifies magnetic ordering, specific heat, critical temperature, resistivity, etc... As the actual magnetic fields reproducible in laboratory are relatively small, the two competing phases must be very close in energy to give rise to this kind of transition.

The main mechanisms that generate the metamagnetism are three:

1. small crystal field splitting
2. electronic correlations
3. band structure effects

The first case occurs when the magnetic field is comparable to the crystal field splitting, and therefore it can produce a drastic effect on the level structure, including the possibility to field-induced transition due to level crossing. The metamagnetic

transition appears if the crystal field separates two electron configurations, with different spin quantum numbers, that respond differently under magnetic field. This mechanism can generate multiple jumps of the order of $1 \mu_B$ in the magnetization as experimentally found in URu_2Si_2 [12].

The second mechanism is the most studied and most present in nature. This phenomena is very interesting because can drive the system towards a metal-insulator transition or insulator-metal transition. Let us consider strongly correlated antiferromagnetic insulators; it is known that electronic correlations create metamagnetic transition [13, 14], but, the mean field theory can not describe metamagnetism in antiferromagnetic insulator [15] and we need to overcome it. Therefore the metamagnetic properties of antiferromagnetic insulators have to be derive from the full physics of the Hubbard model. Using dynamical mean field theory, it is possible to describe qualitatively several scenario: metamagnetic transition from antiferromagnetic insulator to paramagnetic insulator, insulator to metal transition, metallic antiferromagnetic to paramagnetic metal [15]. The uniform magnetic field favours competing phase compared to the antiferromagnetism. In the antiferromagnetic case, there is a competition between the antiferromagnetic insulator ground state and the paramagnetic (or ferromagnetic) phase, that at low temperatures can co-exist in a mixed phase [13]. The jump in the magnetization destroys the staggered magnetization, i.e. the order parameter of the antiferromagnetic phase [15], creating a completely new phase for the system. Metamagnetic effects are found in the Hubbard model without band structure effects [16]. Now, let us consider a correlated metallic state close to the antiferromagnetic insulator instabilities described by the Hubbard model. Then the switching on of the magnetic field has a similar effect as increasing U . If the system is near the Brinkman-Rice transition the magnetic field can induce localization. At half filling, the system jumps from a metallic state with a finite number of double occupancy to an insulating state without double occupancy [14, 17].

Having in mind to study the realistic system $Sr_3Ru_2O_7$, we will analyse in detail the metamagnetism caused by band structure effects in the weak coupling limit. The Coulomb repulsion is also important, but, differently from the other mechanisms is mandatory to take in account the shape of the density of state. In some compounds metamagnetic transitions, smeared over a wide range of fields and occurring with hysteresis, are observed. This theory can explain also the hysteresis in metamagnetic transition [18]. Our results for the magnetization as a function of field, temperature and the band filling are in qualitative agreement with observed properties of the two-

and three-layer ruthenate compounds [19, 20], and suggest that the general magnetic phase diagram of n-layer ruthenates might be understood in terms of band structure properties. Respect to the previous mechanism the transition is less drastic, because the system goes from the paramagnetic ground state to the ferromagnetic phase.

The chapter is organized as follows. In paragraph 2 we introduce the mean field theory of itinerant uniform ferro/metamagnetism and its consequences as the Stoner criterion. In paragraph 3 the theory is applied to two cases: the phase diagram, the quantum critical endpoint (*QCEP*) and the critical magnetic field are also shown. Paragraph 4 is devoted to general considerations about this approach.

2.2 Mean-field theory of itinerant uniform ferro/metamagnetism

Here, we will examine in detail all the aspects of mean field theory of itinerant uniform ferro/metamagnetism and its consequences as the Stoner criterion, *QCEP* and the maximum in the susceptibility.

The thermodynamic potential which is extremely useful for the study of quantum system is the grand potential Ω . It is a thermodynamic potential energy for process carried out in open system where particle number and magnetic field can vary but the temperature T , the magnetization M and the chemical potential μ are fixed. T , M , μ are the variable of the this thermodynamic potential, and calculations are easy to perform in this ensemble. If we call U the internal energy, then the grand potential is

$$\Omega(T, \mu, M) = U - TS - \mu N \quad (1)$$

Now, we are interested in fixing particle number and magnetic field because this is the experimental situation. So, we will change the thermodynamic potential by Legendre transformation:

$$G(T, N, h) = \Omega + \mu N - hM \quad (2)$$

where $h = g_0\mu_B H$ is the reduced field and H is the magnetic field. We consider a single-band model of electrons interacting via on-site Coulomb repulsion U in mean

field approximation. We consider an Hubbard term \hat{H}_U in the Hamiltonian:

$$\hat{H}_U = U\hat{n}_\uparrow\hat{n}_\downarrow \quad (3)$$

$$\hat{H}_U^{MF} = U\langle\hat{n}_\uparrow\rangle\hat{n}_\downarrow + U\hat{n}_\uparrow\langle\hat{n}_\downarrow\rangle - U\langle\hat{n}_\uparrow\rangle\langle\hat{n}_\downarrow\rangle \quad (4)$$

$$\langle\hat{H}_U^{MF}\rangle = U\langle\hat{n}_\uparrow\rangle\langle\hat{n}_\downarrow\rangle \quad (5)$$

We add the Hubbard term to the thermodynamic potential, consider the two spin channels and obtain:

$$G(T, n_\uparrow, n_\downarrow, h) = \sum_{\sigma=\uparrow,\downarrow} (\Omega(\mu_\sigma, T) + \mu_\sigma n_\sigma) + U n_\uparrow n_\downarrow - hM \quad (6)$$

The thermodynamically stable solution minimizes the Gibbs free energy in equation (6). The only information about the band structure which enters in the mean field theory is the density of state (*DOS*) for spin as a function of energy $\rho(\varepsilon)$. Given the *DOS*, one obtains the grand canonical functional:

$$\Omega(\mu_\sigma, T) = -k_B T \int d\varepsilon \rho(\varepsilon) \ln(1 + e^{-\beta(\varepsilon - \mu_\sigma)}) \quad (7)$$

where k_B is the Boltzmann constant and $\beta = \frac{1}{k_B T}$. The chemical potential is given implicitly by

$$n_\sigma(\mu_\sigma) = -\partial_{\mu_\sigma} \Omega_0(\mu_\sigma, T) = \int d\varepsilon \rho(\varepsilon) f(\varepsilon - \mu_\sigma, T) \quad (8)$$

where $f(\varepsilon, T)$ is the Fermi function. Once the Gibbs free energy is determined, we obtain the thermodynamic equation of state for magnetic systems. We can develop the Taylor series for $G(M)$ about the point $M = 0$:

$$G(M, T, n) = \sum_{k=0}^{\infty} \frac{G^{(k)}(M=0, T, n)}{k!} M^k \quad (9)$$

To calculate the derivatives $G^{(n)}(0)$, we need to make explicit the dependence of M from the variables n_\uparrow and n_\downarrow by

$$\begin{cases} M = \frac{n_\uparrow - n_\downarrow}{2} \\ n = \frac{n_\uparrow + n_\downarrow}{2} \end{cases} \quad (10)$$

We note that the maximum of the magnetization M_{max} is n if $n < \frac{1}{2}$ and $1 - n$ if $n > \frac{1}{2}$ for single band model.

Another quantity that is needed to calculate is $\frac{\partial \mu_\sigma}{\partial M}$; we can determine this quantity by using two ways:

$$\begin{cases} \frac{\partial n_\sigma}{\partial M} = \frac{\partial(n + \sigma M)}{\partial M} = \sigma \\ \frac{\partial n_\sigma}{\partial M} = \frac{\partial \int d\varepsilon \rho(\varepsilon) f(\varepsilon - \mu_\sigma, T)}{\partial M} = \int d\varepsilon \rho(\varepsilon) \frac{\partial f(\varepsilon - \mu_\sigma, T)}{\partial(\varepsilon - \mu_\sigma)} \frac{\partial(\varepsilon - \mu_\sigma)}{\partial \mu_\sigma} \frac{\partial \mu_\sigma}{\partial M} = A_0(\mu_\sigma, T) \frac{\partial \mu_\sigma}{\partial M} \end{cases}$$

where

$$A_n(\mu, T) = \int d\varepsilon \rho^{(n+1)}(\varepsilon) f(\varepsilon - \mu, T) \quad (11)$$

We note that

$$\lim_{T \rightarrow 0} A_n(\mu, T) = \rho^{(n)}(\mu) = \rho^{(n)}(\varepsilon_F) \quad (12)$$

where $\rho^{(n)}(\mu)$ denotes the n -th derivative of the *DOS* at the Fermi level. Putting together the two expressions for $\frac{\partial n_\sigma}{\partial M}$ we have:

$$\frac{\partial \mu_\sigma}{\partial M} = \frac{\sigma}{A_0(\mu_\sigma, T)} \quad (13)$$

$$\frac{\partial A_n(\mu_\sigma, T)}{\partial M} = \frac{\sigma A_{n+1}(\mu_\sigma, T)}{A_0(\mu_\sigma, T)} \quad (14)$$

Now, we can take the derivative of the equation (6) and using (7), (8) and (10) we get:

$$G^{(1)}(M, T) = \sum_{\sigma=\uparrow, \downarrow} \sigma \mu_\sigma - 2UM - h \quad (15)$$

and we can make high order derivative using (11), (13) and (14) to get at $M = 0$:

$$\left\{ \begin{array}{l} G^{(1)}(M = 0, T) = -h \\ G^{(2)}(M = 0, T) = \sum_{\sigma=\uparrow, \downarrow} \left(\frac{1}{A_0(\varepsilon_F, T)} \right) - 2U = 2 \left(\frac{1}{A_0(\varepsilon_F, T)} - U \right) \\ G^{(3)}(M = 0, T) = 0 \\ G^{(4)}(M = 0, T) = \sum_{\sigma=\uparrow, \downarrow} \left(\frac{3A_1^2 - A_0 A_2}{A_0^3} \right) = 2 \left(\frac{3A_1^2 - A_0 A_2}{A_0^3} \right) \\ \dots \end{array} \right.$$

We stress that $G(M = 0)$ is an arbitrary constant that we set to zero, and we can obtain the entire functional $G(M, T)$ from equation (9).

$$G(M, T, \varepsilon_F) = \frac{1}{A_0(\varepsilon_F, T)} M^2 + \left(\frac{\left(\frac{A_1}{A_0} \right)^2 - \left(\frac{A_2}{3A_0} \right)}{A_0^3} \right) \frac{M^4}{4} + \dots - UM^2 - hM \quad (16)$$

All the derivatives of the *DOS* give contribution, in different way, to make the thermodynamic functional $G(M)$. Increasing U from 0, magnetization sets in if for some M , $G(M, T)$ can have an absolute minimum for M different from zero. This paramagnetic-ferromagnetic transition may be either first-order or second-order, depending on the band structure. We can observe that magnetic field and Coulomb repulsion have a similar effect on the thermodynamic potential, so, also the magnetic field can induce first-order transition. The two differences between h and U are the energy range and power of the coefficient. Indeed, U is around 1 eV and h can induces effects around 10^{-4} eV. The linear power of h in the polynomial is responsible for the linear character of $M(h)$, when h goes to zero.

2.2.1 The Stoner criterion and its generalization

Let us set the external field $h = 0$. The Gibbs free energy for $M \rightarrow 0$

$$G(M, T, \varepsilon_F) \approx \left(\frac{1}{A_0(\varepsilon_F, T)} - U \right) M^2 \quad (17)$$

consists of two terms: spin polarization costs band energy which goes as M^2 and it gains interaction energy which is also proportional to M^2 . When U is smaller than the critical value

$$U_{Stoner} = \frac{1}{A_0(\varepsilon_F, T)} \quad (18)$$

the energy is minimized by $M = 0$, while for $U > U_{Stoner}$, the energy is lowered making M finite. The paramagnetic state becomes unstable against the onset of ferromagnetic ordering. Equation (18) is the well known Stoner criterion [21]. Using the Stoner criterion, we conclude that it is favourable for the appearance of ferromagnetism if ε_F is sitting in a sharp peak of the density of state. If this criterion is verified, a second order transition occurs: the magnetization changes continuously if increases U or decreases T . Now, we can find the critical temperature T_C for the second-order transition. Using the finite temperature criterion,

$$U_{Stoner} = \frac{1}{A_0(\varepsilon_F, T_C)} \quad (19)$$

we find that T_C is overestimated by a factor of ~ 5 . The essential reason for the discrepancy is that the mean field theory grossly underestimates the entropy of the paramagnetic metal: we consider only the entropy coming from electron-hole excitation, but neglect the fact that disordered moments exist also above T_C giving rise to a high spin entropy.

However, the second order transition occurs if the system is not already ferromagnetic when the Stoner criterion is verified. Sometimes, it is possible to have a first-order transition before the Stoner transition. A first order transition means that the non-magnetic state becomes unstable against a finite- M state. When the transition occurs in presence of magnetic field, the magnetization presents a jump for a critical magnetic field H_c and the transition is called metamagnetic. In this case, the onset of ferromagnetism is governed by the finite-magnetization Stoner criterion [7] for a first order onset:

$$\frac{2UM}{\mu_\uparrow - \mu_\downarrow} = 1 \quad (20)$$

The finite magnetization criterion holds for all M once the system is polarized, irrespective of the order of the onset. Just how large M will be, can not be decided

unless we return to the full energy expression (16). This finite-magnetization criterion is less powerful than the Stoner criterion, because we need to calculate μ_\uparrow and μ_\downarrow . The presence of a Van Hove singularity (*VHS*), or at least a pronounced maximum in the *DOS*, in the first order transition is necessary. When μ_σ nearer the *VHS*, there is no stable solution for the system and μ_σ goes from one side to another side of the *VHS* to create the jump in the magnetization. The critical magnetic field strongly depends from the distance of *VHS* from Fermi energy. If the Fermi energy is far from *VHS*, the system can exhibit metamagnetism just at huge critical magnetic field because the chemical potential needs to arrive to *VHS* to create the jump in the magnetization. If we introduce the mean value of the *DOS* $\bar{\rho}$:

$$2M = n_\uparrow - n_\downarrow = \int_{\mu_\uparrow}^{\mu_\downarrow} \rho(\varepsilon) d\varepsilon = \bar{\rho}(\mu_\uparrow - \mu_\downarrow) \quad (21)$$

we can recover the original form of the Stoner criterion

$$U\bar{\rho} = 1 \quad (22)$$

If there is a *VHS* near the Fermi level, the mean value can be higher than the *DOS* evaluated at Fermi energy. In this case, the first-order criterion is verified for U smaller than U_{Stoner} . The first-order transition occurs before the Stoner transition. It is possible to find other generalizations of the Stoner criterion for non uniform magnetization and spin waves [7]. When the density of state decreases, then U_{Stoner} increases and the system goes far from ferromagnetism. On the other hand, when the density of state decreases, the modulus of fourth order coefficient increases. We will demonstrate that, if the conditions for metamagnetism are verified, the metamagnetic properties of the systems increase when the modulus of the fourth order coefficient increases. For this reason, a high value of density of state favours ferromagnetism in comparison to metamagnetism.

In the case of zero temperature, the expression of the functional becomes easy to understand. The Ω functional is given by

$$\Omega(\mu_\sigma, T = 0) = \int_{-\infty}^{\mu_\sigma} (\varepsilon - \mu_\sigma) \rho(\varepsilon) d\varepsilon \quad (23)$$

We can calculate explicitly all the coefficients of the functional using equation (12).

Here, we report the coefficients of the low order terms

$$G^{(2)}(M = 0, T = 0) = 2 \left(\frac{1}{\rho(\varepsilon_F)} - U \right) \quad (24)$$

$$G^{(4)}(M = 0, T = 0) = 2 \frac{3\rho'(\varepsilon_F)^2 - \rho''(\varepsilon_F)\rho(\varepsilon_F)}{\rho(\varepsilon_F)^5} \quad (25)$$

$$G^{(6)}(M = 0, T = 0) = 2 \frac{105\rho'^4 - 105\rho\rho'^2\rho'' + 10\rho^2\rho''^2 + 15\rho^2\rho'\rho''' - \rho^3\rho''''}{\rho(\varepsilon_F)^9} \quad (26)$$

where the factor 2 is due to spin degeneracy. If all the coefficients of the functional $G(M, T = 0)$ are known, the complete function DOS can be evaluated by Taylor series expansion. We have the Stoner transition when $G^{(2)}(M = 0, T = 0) = 0$. However, it is very difficult to calculate numerically high derivatives of the DOS , in particular, the ab-initio evaluation of $G^{(6)}(M = 0, T = 0)$ and higher terms.

2.2.2 QCEP and effect of the temperature on susceptibility

First-order transitions do not normally show critical fluctuations as the material moves discontinuously from one phase into another one. However, if the first order phase transition does not involve a change of symmetry, then the phase diagram can contain a critical endpoint where the first-order phase transition terminates. Such an endpoint has a divergent susceptibility. The transition between the liquid and gas phases is an example of a first-order transition without a change of symmetry and the critical endpoint is characterized by critical fluctuations known as critical opalescence. A quantum critical endpoint arises when a finite temperature critical point is tuned to zero temperature. One of the best studied examples occurs in the layered ruthenate metal, $\text{Sr}_3\text{Ru}_2\text{O}_7$ in a magnetic field [22]. This material shows metamagnetism with a low-temperature first-order metamagnetic transition where the magnetization jumps when a magnetic field is applied within the directions of the layers. The first-order jump terminates in a critical endpoint at $T \approx 1\text{K}$. By switching the direction of the magnetic field so that it points almost perpendicular to the layers, the critical endpoint is tuned to zero temperature at a field of about 8 teslas. The resulting quantum critical fluctuations dominate the physical properties of this material at nonzero temperatures and away from the critical magnetic field. Finally, the resistivity shows a non-Fermi liquid response.

The susceptibility in the Hubbard model at zero temperature in mean field approx-

imation is

$$\chi = \frac{(g\mu_B)^2 \rho(\varepsilon_F)}{2} \frac{1}{1 - U\rho(\varepsilon_F)} \quad (27)$$

where the first factor is the usual Pauli susceptibility. The susceptibility is enhanced by the electron-electron interaction, and this factor is called exchange enhancement factor. If U is somewhat smaller than U_{Stoner} , then the exchange enhancement factor is large and we expect to see a nearly ferromagnetic metal with a large susceptibility. It is thought that the anomalously large susceptibility of Palladium is basically of such a nature. Now, if we consider the Sommerfeld expansion we obtain in two limit cases [7]

$$\frac{\chi}{2\mu_B^2} \approx \rho(\varepsilon_F) + \frac{\pi^2}{12} \left(\frac{\rho(\varepsilon_F)\rho''(\varepsilon_F) - 2\rho'(\varepsilon_F)^2}{\rho(\varepsilon)} \right) (k_B T)^2 \quad \text{for } T \rightarrow 0 \quad (28)$$

$$\frac{\chi}{2\mu_B^2} \approx \frac{1}{4k_B T} \quad \text{for } T \rightarrow +\infty \quad (29)$$

If the condition

$$G^{(4)}(M = 0, T = 0) \propto 3\rho'(\varepsilon_F)^2 - \rho(\varepsilon_F)\rho''(\varepsilon_F) < 0 \quad (30)$$

is verified, $\chi(T, M = 0)$ is not monotonous, but has a maximum as a function of T as we can see from equations (28) and (29). Moreover, the entropy $S = -\frac{\partial F}{\partial T}$ at low temperatures does not decrease monotonously with the magnetization, but has a maximum at a finite M . An example of not monotonous susceptibility is presented in Fig. 1.

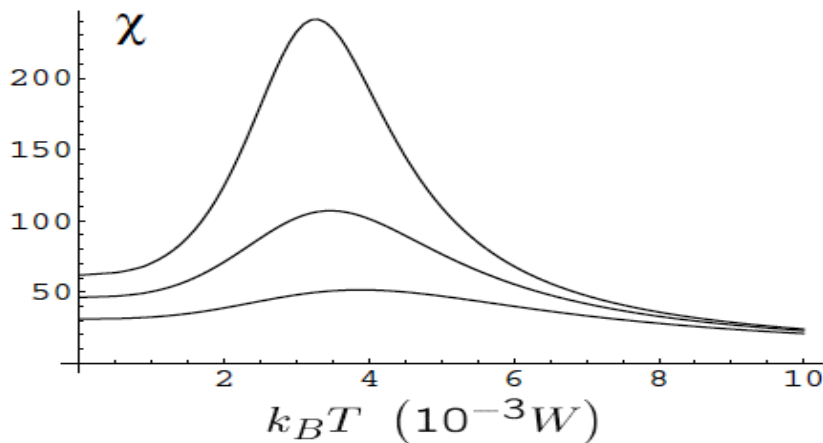


Figure 1: Zero-field spin susceptibility as a function of temperature for three different fillings, the top curve is for filling nearer the VHS from [23]. The same maximum appear if U increases [7]. We can observe experimentally a similar maximum in the $Sr_3Ru_2O_7$ susceptibility [24].

2.3 Effective models

We will analyse two effective models at $T = 0$. The first is the oversimplified model M^6 , the second is the complete theory for a particular case: the one-dimensional density of state for tight binding. In both cases, we will see that the metamagnetic phase is realized in a wide region in the phase diagram between the paramagnetic and the ferromagnetic regions. We will see that the quantity $G^{(4)}(M = 0)$ is fundamental for the magnetic properties, but is not necessary and not sufficient to produce metamagnetic transition, because other quantity like $G^{(6)}(M = 0)$ can give rise the same properties. If the negative value $G^{(4)}(M = 0)$ decreases, then the metamagnetic properties increase and the critical magnetic field will be lower.

2.3.1 The M^6 theory

The M^6 theory was introduced by Landau, who described multicritical behaviour within his phenomenological theory of phase transition [25]. This simple model shows how the $G^{(4)}(M = 0, T = 0)$ coefficient is essential to understand the metamagnetism for itinerant electrons. The magnetization M in the single band model must be less than $\frac{1}{2}$ by definition (10). Because M is small, we can consider an approximation of the Taylor series cutting higher terms. We study a M^6 theory because is it the minimal model to have metamagnetism. Within the mean field approximation, let us consider:

$$G(M) = AM^2 - BM^4 + CM^6 - hM \quad (31)$$

where A and C are respectively $G^{(2)}(M = 0, T = 0)$ and $G^{(6)}(M = 0, T = 0)$. Instead, we set $B = -G^{(4)}(M = 0, T = 0)$. For simplicity, we take C to be a positive fixed constant; whereas A and B are variable parameters. The only case where we can find metamagnetism is for A and B positive. In this M^6 approximation, the fourth order coefficient negative is condition necessary but not sufficient to have metamagnetism [26]. In the complete case, this condition is not necessary because other term like the 6-order coefficient or the 8-order coefficient can have the same role. The simplified M^6 model can reproduce just two minima: one paramagnetic minimum and one ferromagnetic minimum. For this reason, it is possible to reproduce just one jump from a paramagnetic solution to a ferromagnetic solution. To reproduce two metamagnetic jumps or a jump between two ferromagnetic solutions, we need a M^8 theory [27]. The M^6 model does not contain important information,

like the distance of *VHS* from Fermi energy, because we lost information about the *DOS* in the Taylor series cutting. In this simplified model just the first four derivatives are present, instead, in the complete model the functional contains all the derivatives of the *DOS* and the distance from the *VHS* is an important parameter.

We will consider the case without magnetic field, and we will find when there is the ferromagnetic solution. Because $G(0) = 0$, we have a ferromagnetic solution if there are other values of magnetization so that $G(M) = 0$. We will find a magnetization different from zero if the determinant of the equation (31) is greater than zero. So, the ferromagnetic solution is stable if

$$B^2 - 4AC > 0 \implies B > 2\sqrt{AC} \quad (32)$$

When we switch on the magnetic field, it is possible to find the metamagnetic phase. The limit case that separates the paramagnetic and metamagnetic cases is when, in presence of magnetic field, the paramagnetic minimum and the ferromagnetic minimum degenerate in the same magnetization \bar{M} . In this case, the functional will assume the form $G(M) = D(M)(M - \bar{M})^4$ where $D(M)$ is a second order polynomial. The analytic condition to find this separation line in the diagram phase is

$$\begin{aligned} G'(\bar{M}) &= 0 \\ G''(\bar{M}) &= 0 \\ G'''(\bar{M}) &= 0 \end{aligned} \quad (33)$$

From these equations we obtain the separation line between the paramagnetic and the ferromagnetic region in the phase diagram, the critical magnetic field at the onset of the transition and the value of \bar{M} as function of A, B, C and h . The critical magnetic field at the onset of the transition is nothing else than the magnetic field at quantum critical end point h_{QCEP} . The separation line is given by:

$$B = \sqrt{\frac{5}{3}AC}$$

and h_{QCEP} is given by:

$$h_{QCEP} = \frac{16}{5} \left(\frac{1}{3}\right)^{\frac{3}{2}} \sqrt{\frac{A^3}{B}} \cong 0.616 \sqrt{\frac{A^3}{B}} \quad (34)$$

or make explicit the magnetic field H :

$$H_{QCEP} = \frac{16}{10\mu_B} \left(\frac{1}{3}\right)^{\frac{3}{2}} \sqrt{\frac{A^3}{B}} \cong 5.32 \times 10^4 \frac{Tesla}{eV} \sqrt{\frac{A^3}{B}} \quad (35)$$

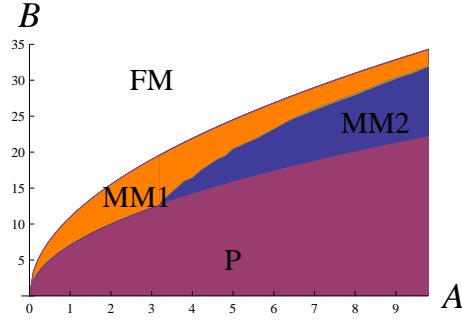


Figure 2: Phase Diagram of the M^6 theory with respect to A and B (arbitrary units). The phase are FM: ferromagnetic, P: paramagnetic, MM1: metamagnetic region with critical magnetic field under 10^4 Tesla, MM2: metamagnetic region with critical magnetic field above 10^4 Tesla. The y-axis is the Stoner criterion equation.

The H_{QCEP} is not always physically accessible, the only possibility is that the system is near the Stoner instability or we need a very high value for the coefficient B . The limit for $h \rightarrow 0$ is:

$$h = \sqrt{2} \frac{4AC - B^2}{4AC} \sqrt{\frac{A^3}{B}} \quad (36)$$

The conclusion we have reached are summarized in the phase diagram in the AB plane, in Fig. 2. The point $A = B = 0$ marks the termination of second-order Stoner phase transition, and the ordinary critical point of a first order transition. Landau called it a "critical point of the second-order transition", but now is adopted the common designation "tricritical point" suggested by Griffiths [28]. We need B between $\sqrt{\frac{5}{3}}\sqrt{AC}$ and $2\sqrt{AC}$ to have metamagnetism, or equivalently

$$\frac{5}{3}AC < B^2 < 4AC \quad (37)$$

but the critical magnetic field can be very high. The orange region in the Fig. 2 has critical magnetic field less than 10^4 Tesla (for typical C value). We can understand that the physical accessible region is much narrow in the phase diagram. We can speculate that some materials that, today, we suppose to be paramagnetic are metamagnetic with a very high critical metamagnetic field. A general issue is that the metamagnetic region is between the paramagnetic and ferromagnetic regions, but to be physically accessible we need low critical magnetic field; therefore the system must be near the ferromagnetic instability. When we go close to the ferromagnetic phase, then the critical magnetic field gets lower and lower. At the ferromagnetic instabilities the critical magnetic field is zero. When $\rho(\varepsilon_F)$ increases, the value of A and B decrease. The position of the system on the phase diagram moves towards the origin and the system tends to lost the metamagnetism. We can

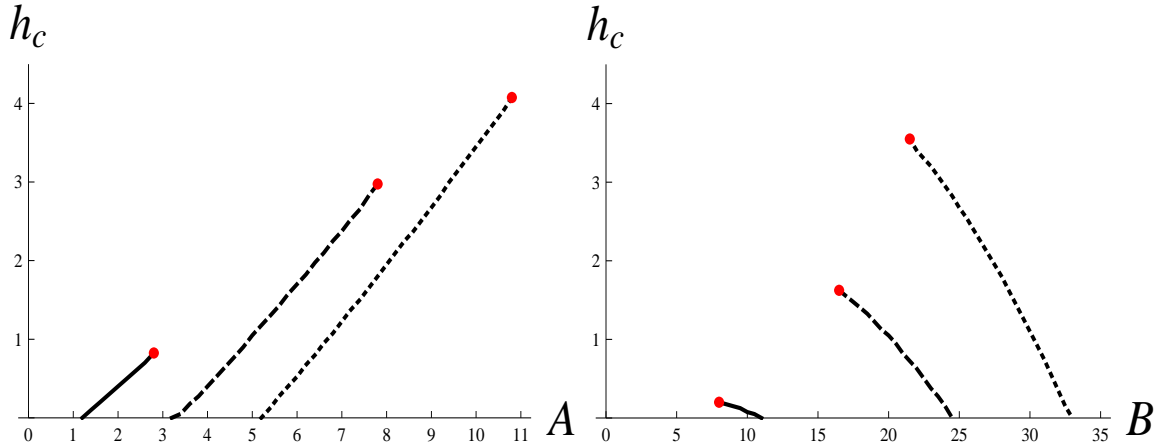


Figure 3: Critical metamagnetic field function of coefficient A (left panel) and B (right panel) setting $C=30$. In the left panel we fix $B=12$ (solid line), $B=20$ (dashed line) and $B=26$ (dotted line). In the right panel we fix $A=1$ (solid line), $A=5$ (dashed line) and $A=9$ (dotted line). The circle red dots are the quantum critical endpoints.

conclude that an elevated DOS at Fermi level reduces the probability of obtaining metamagnetism. To have a high value of the B coefficient we need:

$$\rho(\varepsilon_F) \ll 1 \quad (38)$$

$$\rho'(\varepsilon_F) \cong 0 \quad (39)$$

$$\rho''(\varepsilon_F) \gg 1 \quad (40)$$

We will see that, when all these conditions are verified, is it possible to have metamagnetism for any $U > 0$.

In Fig. 3, we show the critical magnetic field as a function of A and B . We can observe that, near to ferromagnetic instability, a very low magnetic field can induce first-order phase transition.

2.3.2 The one-dimensional density of state

We can observe that in the mean field theory, we just need the density of state to calculate the phase diagram and the thermodynamic properties [18]. In this paragraph, we will consider the density of state

$$\rho(\varepsilon) = \frac{1}{\pi \sqrt{(2t)^2 - (\varepsilon - \varepsilon_0)^2}} \quad (41)$$

that comes from the one-dimensional tight binding dispersion relation

$$\varepsilon(k) = \varepsilon_0 - 2t \cos(k) \quad (42)$$

and we will calculate analytically the functional $G(M)$, the phase diagram and the magnetization as a function of magnetic field and Coulomb repulsion. Though the one-dimensional Hubbard model is antiferromagnetic, we analyze just the competition between the paramagnetic and the ferromagnetic phase. At half filling, the function (41) presents a low value for $\rho(\varepsilon_F)$, $\rho'(\varepsilon) = 0$ and $\rho''(\varepsilon) \gg 1$. These conditions makes G^4 optimal to find the metamagnetism in the system. Considering that the odd terms of $G(M)$ Taylor expansion are zero, we can calculate all the terms of the series using:

$$G^{(n+2)}(M=0, T=0, \varepsilon_F) = \frac{1}{\rho(\varepsilon)} \frac{d}{d\varepsilon} \left(\frac{1}{\rho(\varepsilon)} \frac{dG^{(n+2)}(M=0, T=0, \varepsilon)}{d\varepsilon} \right) \Big|_{\varepsilon=\varepsilon_F} \quad (43)$$

from which, we obtain:

$$G^{(2)}(M=0, T=0, \varepsilon_F) = 2 \left(\pi \sqrt{(2t)^2 - (\varepsilon_F - \varepsilon_0)^2} - U \right) = 2(2t\pi \sin(\pi n) - U)$$

$$G^{(4)}(M=0, T=0, \varepsilon_F) = 2 \left(-\pi^3 \sqrt{(2t)^2 - (\varepsilon_F - \varepsilon_0)^2} \right)$$

$$G^{(6)}(M=0, T=0, \varepsilon_F) = 2 \left(\pi^5 \sqrt{(2t)^2 - (\varepsilon_F - \varepsilon_0)^2} \right) \quad (44)$$

The quartic term is always negative, therefore it is very likely that we will find metamagnetism for any filling. Now, we can use the equation (103) from Appendix A to remove the explicit dependence from the Fermi energy:

$$G^{(2)}(M=0, T=0, \varepsilon_F) = 2(2t\pi \sin(\pi n) - U) \quad (45)$$

When the second order term $G^{(2)}(M=0, T=0, \varepsilon_F)$ is zero, we have the Stoner criterion. The Stoner solution appears for $U > 2t\pi \sin(\pi n)$, but we will show that it is not the ground state, because the ground state is the solution coming from first-order transition. We introduce the filling variable instead of ε_F in the whole functional and we have:

$$G(M, T=0, n) = 2(2t \sin(\pi n)) \left(\frac{\pi}{2!} M^2 - \frac{\pi^3}{4!} M^4 + \frac{\pi^5}{6!} M^6 + \dots \right) - UM^2 - hM \quad (46)$$

We are able to factorize the dependence from the filling, this simplification happens accidentally because all the coefficients in equation (44) have the same dependence from the filling. Introducing the cosine's Taylor series, we obtain:

$$G(M, T=0, n) = \frac{4t \sin(\pi n)}{\pi} \cos(\pi M) - UM^2 - hM \quad (47)$$

An other way to obtain (47) with an easier way to understand the magnetic solution is presented in appendix B.

Now, we will compute the separation line between the metamagnetic and the paramagnetic solutions. We need to replace the equations (33) used in the previous paragraph with:

$$\begin{cases} G'(\bar{M}) = 0 \\ G''(\bar{M}) = 0 \\ \bar{M} = M_{max} \end{cases}$$

From these equations we obtain the separation line, the critical magnetic field at the quantum critical endpoint and the value of \bar{M} as function of n and U . Thus the paramagnetic solution is the ground state for

$$\frac{U}{t} < \begin{cases} \pi \sin(2n\pi) & \text{for } n < \frac{1}{2} \\ \pi \sin(2(1-n)\pi) & \text{for } n > \frac{1}{2} \end{cases}$$

and the critical magnetic field at the quantum critical endpoint is

$$\frac{h_{QCEP}}{t} = \begin{cases} 2 \sin(\pi n)(2 \sin(\pi n) - \pi n \cos(\pi n)) & \text{for } n < \frac{1}{2} \\ 2 \sin(\pi(1-n))(2 \sin(\pi(1-n)) - \pi(1-n) \cos(\pi(1-n))) & \text{for } n > \frac{1}{2} \end{cases}$$

Comparing the energy, it is possible to show that the partially polarized solution (the Stoner solution) is never the ground state, but, the fully polarized ferromagnetic solution is the ground state for

$$\frac{U}{t} > \begin{cases} 2 \frac{2|\sin(n\pi)| - \sin(2n\pi)}{n^2\pi} & \text{for } n < \frac{1}{2} \\ 2 \frac{2|\sin((1-n)\pi)| - \sin(2(1-n)\pi)}{(1-n)^2\pi} & \text{for } n > \frac{1}{2} \end{cases}$$

We put all these information in the phase diagram in Fig. 4. We can observe the particle-hole symmetry and the Stoner criterion verified when the system is already ferromagnetic. The metamagnetic region is very wide, but the magnetic field is not always physically accessible. We can see that the magnetic properties increase at half filling, where the system is metamagnetic for every $U > 0$. This happens because the fourth order coefficient is maximum at half-filling. Though the Fermi energy is far from *VHS*'s, the large value of this coefficient increases the metamagnetic properties. We need at least a *VHS* to have metamagnetism, but the fourth order coefficient is also important. At the edge of the filling, the high value of the *DOS* favours the ferromagnetism deleting the metamagnetism. It was already known that this system exhibits metamagnetic behaviour up to saturation at half filling [29], but now we find the exact solution for every filling. We stress that for every filling, the

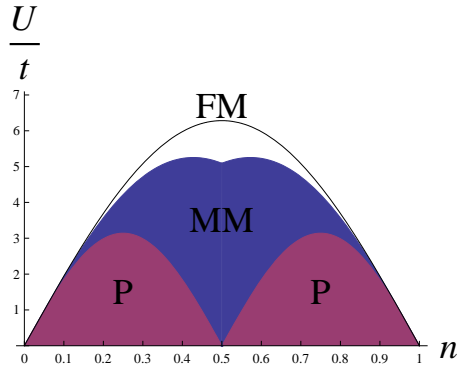


Figure 4: Phase diagram of the one-dimensional density of state. The phase are FM: ferromagnetic, P: paramagnetic, MM: metamagnetic region. The black solid line is the Stoner criterion equation. The phase diagram is symmetrical about half-filling.

system goes from a state with zero magnetization to a fully polarized state tuning U at zero magnetic field.

This result is not trivial because metamagnetism can be found far from the VHS too, and can not be found for all types of density of state. For instance, using this technique with the infinite dimension tight binding model there is no metamagnetism. Where the DOS for the infinite dimension is given by:

$$\rho(\varepsilon) = \frac{1}{\sqrt{2\pi t^2}} \exp\left(-\frac{\varepsilon^2}{2t^2}\right) \quad (48)$$

But, using dynamical mean field theory, Held *et al* [15] found the metamagnetic transition for antiferromagnets also when the non-interacting DOS is (48). This demonstrates that the metamagnetism that comes from band structure effects is different from metamagnetism coming from the full physics of the Hubbard model.

Now, we will calculate the magnetization as function of the magnetic field, filling and the Hubbard repulsion. In Fig. 5, we show the jump in the magnetization that occurs for every U at half filling (right panel), but just for $\frac{U}{t} > \pi$ at quarter filling (left panel). A change in the microscopic properties of the system can shift the critical metamagnetic field. After the jump, the system is always in a fully polarized state because the chemical potential jumps to the other side of the VHS . This is a confirmation that the jump is possible because the presence of the VHS . The position of the VHS at the edge of the DOS causes the fully polarized state after the jump. We can stress the different roles of h and U observing the difference between $M(U)$ and $M(h)$. $M(U)$ is a stepwise function that is 0 until the critical value of U and is equal to M_{max} after the jump. Instead, $M(h)$ has a linear (paramagnetic) behaviour as h approaches to zero and a smaller jump at critical magnetic field.

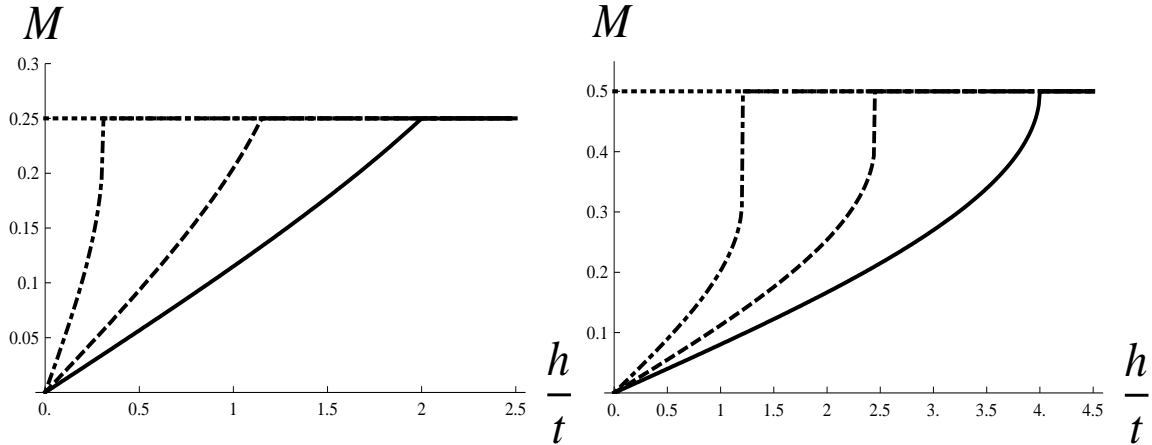


Figure 5: Magnetization vs. magnetic field for the one-dimensional model. We show the jump in the magnetization at quarter filling (left panel) and at half filling (right panel). We tune $\frac{U}{t}=0$ (solid line), $\frac{U}{t}=1.7$ (dashed line), $\frac{U}{t}=3.4$ (dot-dashed line) and $\frac{U}{t}=6.8$ (dotted line).

These considerations can be generalized for every system: if there is a jump in $M(U)$ then there is always a smaller jump in $M(h)$. In Fig. 6, we show the critical magnetic field as function of n and U . We observe that the critical magnetic field at half filling can arrive to $h = 4$, and decreases with the increase of U . The critical magnetic field goes to zero at the ferromagnetic instabilities. If we examine the phase diagram respect to h and n at $\frac{U}{t}=2.9$ eV (Fig. 6 left panel), we have that the system can be paramagnetic, metamagnetic or ferromagnetic. The interesting region is around half filling, where we are far from VHS 's but the great value of $G^{(4)}$ makes possible to achieve a metamagnetic transition condition. For instance, at quarter-filled the Fermi level is nearer to VHS 's but is not metamagnetic. These observation make clear that the conditions for metamagnetism are a complicated mix where VHS , Coulomb repulsion and derivatives of the DOS play different, but equally important roles.

Finding that the $T = 0$ paramagnetic-ferromagnetic transition is first-order, is in itself not unphysical at all. However, it does not necessarily follow that M should immediately jump to the saturation value M_{max} . The DOS model in equation (41) meant to imitate merely a sharp structure around the Fermi energy but not the entire band structure. If the VHS 's or maximums are in the middle of DOS , we should have an abrupt first-order transition to an $M < M_{max}$. A similar case is solved numerically by Fazekas [7], he found similar result using a double-peak DOS

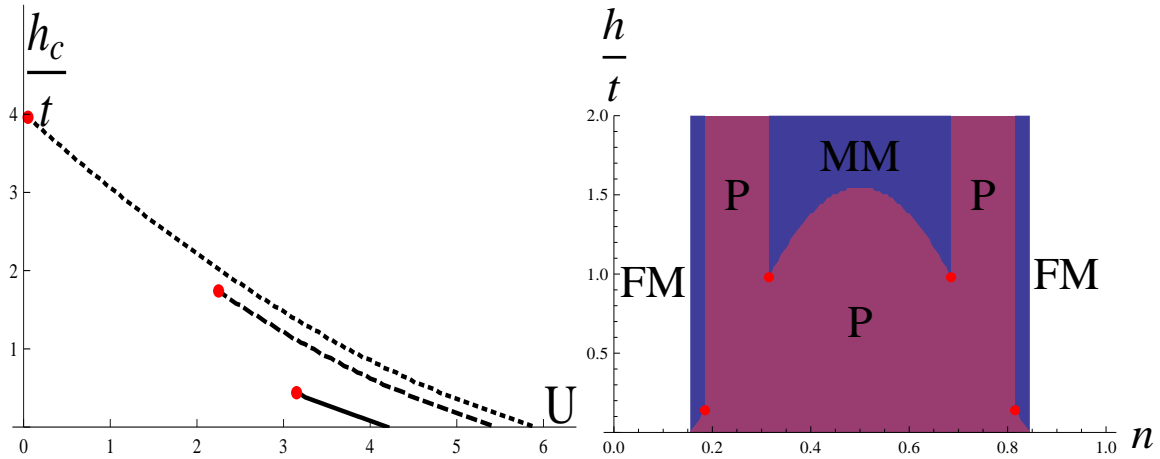


Figure 6: Critical metamagnetic field function of U for $n = \frac{1}{4}$ (solid line), $n = \frac{3}{8}$ (dashed line) and $n = \frac{1}{2}$ dotted line (left panel). Phase diagram at $\frac{U}{t}=2.9$. The phases are FM: ferromagnetic, P: paramagnetic, MM: metamagnetic region (right panel). The red circles are the quantum critical endpoints.

at half-filled:

$$\rho(\varepsilon) = \frac{15}{26} \left(\frac{1}{4} + \frac{7}{16}\varepsilon^2 - \frac{1}{8}\varepsilon^4 \right) \quad \text{for } |\varepsilon| \leq 2 \quad (49)$$

and solving it numerically. The Stoner criterion is satisfied for $U = \frac{104}{15}$. However, the condition for the appearance of finite-amplitude ferromagnetism is much less stringent. For $H = 0$, the first-order transition to saturation magnetization sets in at $U = 4.23$. Choosing a marginally subthreshold value $U = 3.8$, a metamagnetic transition occurs at $h \approx 0.225$.

2.4 Conclusions

We summarise the necessary and sufficient conditions to have metamagnetism in the mean field theory. We need three necessary and sufficient conditions for first-order transition:

1. Presence of a *VHS* (or at least a pronounced maximum in the DOS) to lead to a jump in the magnetization as a function of the magnetic field.
2. Closeness to ferromagnetism to have a physically accessible critical magnetic field. The Coulomb repulsion must be near the critical value for the ferromagnetic transition.

3. Presence of a second minimum at M different from zero in the functional $G(M)$.
The simplest way is to have a negative fourth order coefficient but other terms in the Taylor expansion can generate it.

Moreover, if there is a $M(U)$ with jump, then the $M(h)$ always presents a smaller jump. The calculation of $M(U)$ is an easy way to find metamagnetism. In principle, for the metamagnetic transition is not necessary to have a VHS close to the Fermi level. But, if the VHS is far from Fermi energy, we can have metamagnetism just at huge critical magnetic field. A short distance of VHS from the Fermi level and the closeness to ferromagnetism lower the critical magnetic field. Because the experimental magnetic fields are relatively low in comparison to typical DOS scale energy, this helps the appearance of metamagnetism. The biggest limitation following this approach is the mean field approximation of the Hubbard model. All these conditions might be verified in ruthenates, but the orthorhombic structure pulls the d_{xy} VHS close to the Fermi level favouring the first-order transition at relatively low magnetic field. For completeness, we notice that this approach does not consider instabilities toward nematic or spin spiral phase, and quantum critical effects present in $\text{Sr}_3\text{Ru}_2\text{O}_7$.

3 Collective properties of eutectic ruthenates: role of nanometric inclusions

We study the modification of the electronic structure induced by nanometric inclusions of Sr_2RuO_4 embedded as c -axis stacking fault in $Sr_3Ru_2O_7$ and viceversa. The change of the density of states near the Fermi level is investigated as a function of the electron density, the strength of the charge transfer at the interfaces between the inclusion and the host, and of the distance from the inclusion. Then, we examine how the tendency towards long range orders is affected by the presence of the nanometric inclusions. This is done by looking at the basic criteria for broken symmetry states such as superconductivity, ferromagnetism and metamagnetism. We show that, according to the strength of the charge transfer coupling, the ordered phases may be enhanced or hindered, as a consequence of the interplay between the host and the inclusion, and we clarify the role played by the orbital degree of freedom showing an orbital selective behaviour within the t_{2g} bands. A discussion on the connections between the theoretical outcome and the experimental observations is also presented.

3.1 Introduction

The Ruddlesden-Popper (R-P) ruthenates $A_{n+1}Ru_nO_{3n+1}$ are layered perovskite oxides exhibiting a large variety of electric and magnetic phenomena as the cationic element A and the number n of Ru-O layers forming the unit cell are varied.

Sr_2RuO_4 , the $n=1$ member, is the only layered perovskite oxide that becomes superconductor without Cu and it is an exemplary case of odd-parity spin-triplet pairing among the solid state materials.[5] It is also quite peculiar among the perovskite derived ruthenates since it occurs in an ideal undistorted structure. As a result, substantially nested Fermi surfaces may be anticipated, both because of the two-dimensional nature of the compound and because of the bonding topology of the layered perovskite structure. This in fact is confirmed by different calculations [30, 31, 32, 33, 34, 35, 36] and experimental evidences [37, 38] There are three bands, crossing the Fermi energy, that correspond to the three 4d t_{2g} orbitals, d_{xy} , d_{xz} and d_{yz} . The Fermi surface consists of three sections: these are a nearly circular cylindrical section centered around Γ , denoted as γ and two nearly square cylindrical sections, α and β centered around Γ and X points, respectively.

The $n=2$ R-P member, $\text{Sr}_3\text{Ru}_2\text{O}_7$, is an enhanced Pauli paramagnet[24] on the verge of a magnetic instability, which exhibits at low-temperature a field induced anisotropic metamagnetic transition. Quantum critical behaviour and unconventional properties with possible emergent nematic states occur in proximity of the transition points.[19, 22] According to de Haas-van Alphen[39] and ARPES experiments [40] the Fermi surface is rather complex if compared to the $n = 1$ system with in total twelve sheets reflecting the large unit cell and the character of the octahedral distortions.

Finally, the $n = 3$ R-P member, $\text{Sr}_4\text{Ru}_3\text{O}_{10}$, exhibits a ferromagnetic behaviour when an external magnetic field is applied along the c -axis; besides it manifests a metamagnetic transition for applied magnetic field parallel to the Ru-O plane.[20, 41, 42] SrRuO_3 ($n = \infty$) is the cubic member of the family, and it is an isotropic ferromagnetic metal with $T_c = 160$ K.[43]

The electronic structure changes in a significant way moving from the $n=1$ to the $n=3$ member of the Sr-based RP series especially as a consequence of the unit cell increase and of the crystal symmetry modification from tetragonal to orthorhombic. Evidence of a considerable orbital rearrangement within the t_{2g} and in the hybridizing O(2p) bands has been theoretically addressed and observed by means of polarization-dependent O(1s) x-ray absorption spectroscopy.[44] This analysis reveals a complex interplay of dimensionality, structural distortions and correlations that occur in the Sr-RP series as a function of n .

Concerning the collective behaviour, the crystal purity in ruthenate oxides turns out to be of key importance in connection to the nature and the occurrence of broken symmetry phases. For instance, the superconducting phase in Sr_2RuO_4 emerge only in samples with extreme low residual resistivity.[45] Besides, highly pure single-crystals of $\text{Sr}_3\text{Ru}_2\text{O}_7$ have enabled the observation of quantum oscillations in the resistivity both above and below the critical metamagnetic field.[46]

Recently, high quality eutectic systems based on ruthenates have been synthesized in the shape of naturally occurring mesoscopic and nanoscopic interfaces between members of the RP series or embedding domains with different chemical and structural composition. Such materials represent a natural way to interpolate between the different integer members of the RP series opening novel routes for a quantum tuning of collective properties due to unit cell substitution or to intrinsic interfaces embedded within the same single crystalline phase. Indeed, the modification of the

pairing wave function in the proximity of normal or magnetic systems as well as that of the magnetic long range (ferromagnetism or metamagnetism) due to the interface between the embedded phases may lead to novel quantum states of matter. The main drive behind eutectic growth is given by the possibility of developing composite materials with distinct properties from those of the pure constituents. The first outcome in this direction concerning the ruthenates has been provided by the fabrication of an eutectic phase where islands of pure Ru metal are embedded in a single-crystal matrix of Sr_2RuO_4 . [47, 48, 49] The superconductivity in the newly grown eutectic system has been shown to occur at 3 K instead of 1.5 K as in the pure Sr_2RuO_4 system. The increase in T_c is mainly believed to be due to interface states between the Ru metallic islands and the host Sr_2RuO_4 domain though the lack of the expected proximity behaviour has led to propose that the domains hosting the 3-K superconducting state are away from the Ru- Sr_2RuO_4 interface. [50, 51].

Then, the search for different types of eutectic systems with atomically sharp interfaces has led to the synthesis of $\text{Sr}_2\text{RuO}_4/\text{Sr}_3\text{Ru}_2\text{O}_7$. [52, 53, 54] In this material the two RP phases grow along their common c -axis. The performed magnetic and transport analyses have provided evidence of an unusual behaviour related to the degree of embedding of one phase into the other. [52, 53, 54] Furthermore, $\text{Sr}_4\text{Ru}_3\text{O}_{10}/\text{Sr}_3\text{Ru}_2\text{O}_7$ eutectic crystals have been also successfully achieved. [55] As for the $n = 1$ - $n = 2$ eutectic system, the properties of the resulting material do not correspond to the *sum* of the two constituents. For example, in a sample with a majority of the $n = 2$ R-P phase with respect to the $n = 3$, the system is ferromagnetic with magnetization along the c -axis and a single metamagnetic transition is observed at a critical magnetic field that is smaller to that obtained in the pure $\text{Sr}_3\text{Ru}_2\text{O}_7$ but greater than that in the $\text{Sr}_4\text{Ru}_3\text{O}_{10}$. [56]

The eutectic material on the micrometric scale are made by domains of one crystalline phase with $n=1$ that almost perfectly arrange via sharp interfaces at the boundary with the regions of the $n=2$ members of the R-P family along the c -axis, due to the good matching of the in plane crystallographic axes. Nevertheless, at the nanometric scale the system present defects where one or two unit cells of one phase is replaced by that one of the other crystalline state of the eutectic. The presence of nanometric stacking faults has been experimentally demonstrated by means of transmission electron microscopy. [57, 58] The role of such planar impurity can be highly not trivial in determining the collective behaviour of the system. Indeed, for the $\text{Sr}_2\text{RuO}_4/\text{Sr}_3\text{Ru}_2\text{O}_7$ eutectic the planar Sr_2RuO_4 defects in the $\text{Sr}_3\text{Ru}_2\text{O}_7$ matrix have been considered as a source of resonant centers for pair scattering in

a way that long-range pair correlations can be developed on a distance that it is typically larger than that it is usually expected in a conventional proximity scenario where the Cooper pairs can travel in the normal host up to a distance of the order of the coherence length.[57]

Due to the observed differences in the collective behaviour of the eutectic systems and to the light of the crystallographic composition it is worth to address the following issues: i) how does it change the electronic structure close to the Fermi level due to the presence of c -axis stacking faults for both the defect and the host, ii) how the low energy corrections influence the collective behaviour. To handle these questions we study the electronic structure for inhomogeneous systems and we address the change of the ordered configurations by means of basic criteria for broken symmetry states based on the weak coupling theory of itinerant electron systems. In particular, the analysis aims at underlining the role of the density n_e of the Ru bands and the orbital dependent charge transfer between the host and the impurity assuming they are of the $n=1$ and $n=2$ type of the RP series. We demonstrate that due to spectral weight redistribution the overall response is inhomogeneous and not always concordant between the impurity and the host. Moreover, due to the multi-orbital character of the ruthenates electronic structure the consequences on the broken symmetry instabilities turns out to be highly orbital dependent too.

The chapter is organized as follows. In the paragraph 2 we introduce the model used to analyse the change in the electronic structure and the consequences on the collective properties. In the paragraph 3 the results related to the modification of the density of states at the Fermi level for the planar inclusion and nearby the defect are presented. The paragraph 4 is devoted to the concluding remarks.

3.2 Model

The eutectic system is modelled by means of an effective tight-binding inhomogeneous multiband Hamiltonian. The Hamiltonian includes only the orbital degree of freedom close to the Fermi level originated from the t_{2g} bands of the Ru ion and takes into account the connectivity between the Ru atoms in terms of its first- and second-nearest neighbors within both the single- and the bilayer domains.

We assume an orbital dependent hopping parameterization for the Ru-Ru kinetic

Table 1: Hopping integrals along the direction $[lmn]$ and on-site energy in eV associated to the three orbitals of the t_{2g} sector of the bulk Sr_2RuO_4 at experimental atomic positions [59]. The connecting vector is expressed in terms of the integer set $[lmn]$ and the lattice constants a and c as $\mathbf{d} = l a \mathbf{x} + m a \mathbf{y} + n c \mathbf{z}$. [9, 60, 11]

orbital index	amplitude							
$[lmn]$	[000]	[100]	[010]	[110]	[200]	[020]	$[\frac{1}{2} \frac{1}{2} \frac{1}{2}]$	[001]
xy-xy	-0.4750	-0.3867	-0.3867	-0.1384	0.0094	0.0094	0.0017	-0.0013
yz-xy	0	0	0	0	0	0	0.0057	0
xz-yz	0	0	0	0	0	0	0.0057	0
yz-yz	-0.3224	-0.0389	-0.2914	0.0165	0.0010	0.0612	-0.01876	0.0006
yz-xz	0	0	0	-0.0121	0	0	-0.01356	0
xz-xz	-0.3224	-0.2914	-0.0389	0.0165	0.0612	0.0010	-0.01876	0.0006

term taking as reference the values obtained from a maximally localised Wannier functions approach performed after having obtained the electronic structure by means of *GGA* approximation. Otherwise, due to the lack of first principles analysis of the interface between the two R-P members, the charge transfer across the interface between the $n = 1$ and $n = 2$ domain is considered as a tunable parameter. Its variation can be ascribed to the degree of the octahedral distortions and to the mismatch between the single and the bilayer unit cell occurring at the interface.

The system investigated is depicted in the Fig. 7 where it is reported the structure with one $n = 2$ bilayer inclusion inside the $n = 1$ domain (Fig. 7a) as well as the structure with one $n = 1$ monolayer inclusion inside the $n = 2$ domain (Fig. 7b). The numerical simulation has been performed for a system having a total volume of $L_a \times L_b \times L_c$ with a number of sites for each direction given by $L_a = L_b = 150$ and $L_c = 120$ and 150. We have also modified the number of sites along the c -axis to verify the dependence of the results by the boundary conditions.

The generic Hamiltonian describing our system can be expressed as:

$$H = H_1 + H_2 + H_{12} - \lambda \sum_{\mathbf{i}} n_{\mathbf{i}}$$

where H_n for the $n = 1$ and $n = 2$ components has the following tight-binding structure,

$$H_n = \sum_{\sigma \{ \mathbf{i}, \mathbf{d}_n \}} \sum_{\{ \lambda, \nu \}} t_{\lambda \beta}(\mathbf{d}_n) (c_{\mathbf{i} \lambda \sigma}^\dagger c_{\mathbf{i} + \mathbf{d}_n \nu \sigma} + h.c.) \quad (50)$$

while H_{12} for the part connecting the $n = 1$ and $n = 2$ domains is given by:

$$H_{12} = \sum_{\sigma\{\mathbf{i},\mathbf{d}_{12}\}} \sum_{\{\lambda,\nu\}} \tilde{t}_{\lambda\beta}(\mathbf{d}_{12})(c_{\mathbf{i}\lambda\sigma}^\dagger c_{\mathbf{i}+\mathbf{d}_{12}\nu\sigma} + h.c.).$$

This term is the charge transfer from the Ru bands in the $n = 1$ phase to the first neighbour of the $n = 2$ phase or viceversa.

We have adopted the following notation: $c_{\mathbf{i}\alpha\sigma}^\dagger$ is the creation operator of an electron with spin σ in the band α on the site \mathbf{i} . \mathbf{d} is a generic connecting vector given by $\mathbf{d} = l a \mathbf{x} + m a \mathbf{y} + n c \mathbf{z}$ in terms of integer triple l, m, n and the lattice constants a, c with respect to the basis of the Bravais lattice associated to the single and bilayer system. The indices $\alpha = xy, xz, yz$ label the three orbitals belonging to the t_{2g} sector. The chemical potential μ is fixed in a way to have the local electronic density uniform and constant in each unit cell along the c -axis. The connectivity matrix depends not only on the orbital index but also on the domain where the Ru atom is placed, that is, if it belongs to the $n = 1$ or $n = 2$ crystalline phase, respectively.

Hereafter, we have performed a *GGA* analysis followed by a maximally localised Wannier function approach to determine the overlap amplitudes of the Ru t_{2g} orbitals both for the $n=1$ and the $n=2$ system. We have verified that for $n=1$, the results are in agreement with those obtained by a down-folding procedure as in Ref. [36], while, for the $n = 2$, the results obtained reproduce the Fermi surface features as given in Ref. [40]. We would like to point out that the amplitude of the relevant hopping parameters for the single layer and the bilayer are quantitatively similar along the various symmetry directions. Finally, since we do not have information about how the electronic structure is modified at the interface of the $n=1$ and $n=2$ domain, we do assume that the orbital dependent hopping amplitude along the $[\frac{1}{2} \frac{1}{2} \frac{1}{2}]$ direction across the interface, $\tilde{t}_{\alpha\beta}(\frac{1}{2} \frac{1}{2} \frac{1}{2})$ is a tuning parameter that may be used to mimic the changes of the charge transfer occurring at the interface. The results are presented as a function of $\tilde{t}_{\alpha\beta}(\frac{1}{2} \frac{1}{2} \frac{1}{2})$, with respect to the hopping amplitudes of the $n = 1$ system.

To analyse the changes in the collective behaviour induced by the presence of a planar defect in the broken symmetry phases, we adopt the following procedure: for the superconducting state we take into account the modification of the density of states $\rho(\varepsilon_F)$ at the Fermi level ε_F , considering that for a BCS-type superconductor the critical temperature and the order parameter are exponential functions of the amplitude of the density of states (DOS) at ε_F as $T_{SC} \sim \exp[-1/\lambda\rho(\varepsilon_F)]$. Indeed,

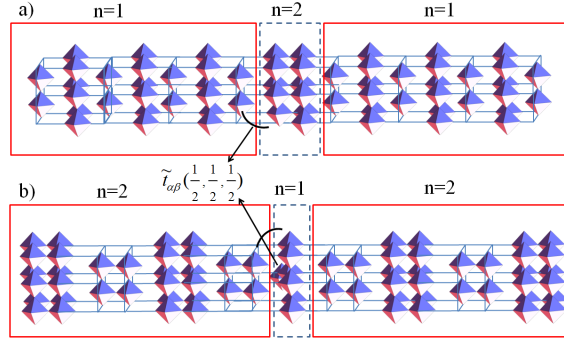


Figure 7: Schematic structure of the eutectic system with stacking faults along the c -axis. a) panel indicates the bilayer ($n = 2$) inclusion inserted in a monolayer ($n = 1$) matrix. In the panel b) it is reported the schematic structure of the monolayer ($n = 1$) inclusion embedded in a bilayer ($n = 2$) matrix. $\tilde{t}_{\alpha\beta}(\frac{1}{2}, \frac{1}{2}, \frac{1}{2})$ stands for the charge transfer amplitude between the α and β bands of Ru atoms at the interface between the $n = 1$ and $n = 2$ layers.

assuming that there is no change in the pairing coupling and for the pairing mechanism, the most significant effect on the strength of the superconducting order comes from the modification of the DOS at the Fermi level on the band where the electrons get paired. Hence, simply one would get an increase/decrease of T_{SC} if the DOS at ε_F grows or it becomes suppressed. This is typically considered in the analysis of the superconducting critical temperatures when the size of the system is tuned from micrometric to nanometric dimension or, for example, when superconductivity occurs in reduced dimension and at the interface.[61, 62, 63, 64]

Referring to the magnetic part, taking into account the expansion of the free energy for an interacting itinerant electron system within the Hartree-Fock approximation in terms of the magnetization and in the presence of an applied field, it is possible to identify the basic quantities that determine the tendency to the magnetic instability. The Gibbs free energy $G(T, h)$ can be expanded up to the sixth order in the total magnetization as follows:[65]

$$G(T, h) = F_0(M, T) - I M^2 - h M \quad (51)$$

$$F_0(M, T) = F_0(0, T) + \frac{M^2}{2\chi_0(T)} + g(T) \frac{M^4}{4} + c(T) M^6 \dots \quad (52)$$

$$\chi_0(T) = \frac{1}{2}\rho(\varepsilon_F)[1 - \frac{\pi^2}{6}RT^2 + \dots] \quad (53)$$

$$g(T) = \left[\frac{F_1}{\rho(\varepsilon_F)^3} \right] \left[1 + \frac{\pi^2}{6}R_1 T^2 + \dots \right] \quad (54)$$

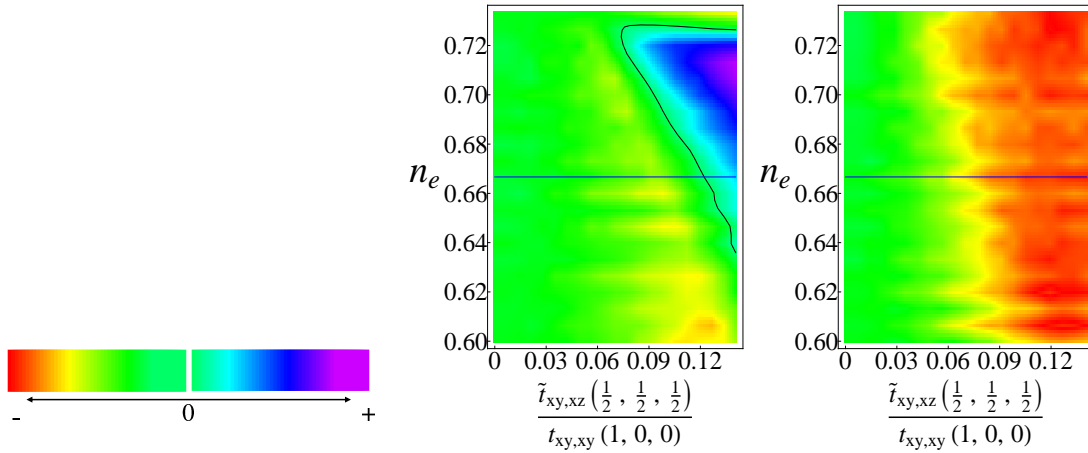


Figure 8: (Color online) Left panel depicts the contour map of the density of states for the d_{xy} band at the Fermi level for the single bilayer inclusion embedded in the $n = 1$ host. The DOS is normalized to that of the analogue band of the uniform bilayer. Right panel reports the DOS variation for the first neighbour of the defect, thus belonging to the host of $n=1$ type, with respect to that for the analogue band of the uniform single layered system. The map of the relative DOS variation is analyzed in terms of the total electron density and as a function of the charge transfer ratio across the $n=1$ and $n = 2$ interface. Top panel is the scale with maximum/minimum values of the order of about 2% with respect to the amplitude of DOS in the uniform case. The solid line is the locus of zeros (i.e. no change with respect to the uniform case) within the contour map. The area inside the solid line corresponds to positive variation of the DOS . The map in the right panel contains only negative values.

$$R = \left(\frac{\rho'(\varepsilon_F)}{\rho(\varepsilon_F)} \right)^2 - \left(\frac{\rho''(\varepsilon_F)}{\rho(\varepsilon_F)} \right) \quad (55)$$

$$F_1 = \left(\frac{\rho'(\varepsilon_F)}{\rho(\varepsilon_F)} \right)^2 - \left(\frac{\rho''(\varepsilon_F)}{3\rho(\varepsilon_F)} \right) \quad (56)$$

$$R_1 = 2F_1 + 3R - F_1^{-1} \left[3 \left(\frac{\rho'(\varepsilon_F)^2 \rho''(\varepsilon_F)}{\rho(\varepsilon_F)^3} \right) - \left(\frac{\rho''(\varepsilon_F)}{3\rho(\varepsilon_F)^2} \right) \right] \quad (57)$$

$$-7 \left[\left(\frac{\rho'(\varepsilon_F) \rho'''(\varepsilon_F)}{3\rho(\varepsilon_F)^2} \right) + \left(\frac{\rho''''(\varepsilon_F)}{3\rho} \right) \right]. \quad (58)$$

Here, $F_{HF}(M, T)$ is the free energy obtained by decoupling the quartic term by means of the Hartree-Fock approximation, the coupling I indicates the Coulomb interaction, and h is the magnetic field, respectively. $\chi_0(T)$ is the zero momentum susceptibility that, together with the Coulomb interaction, sets the instability towards the formation of a ferromagnetic state since it enters the Stoner criterium $2I\chi_0(T) - 1 = 0$.

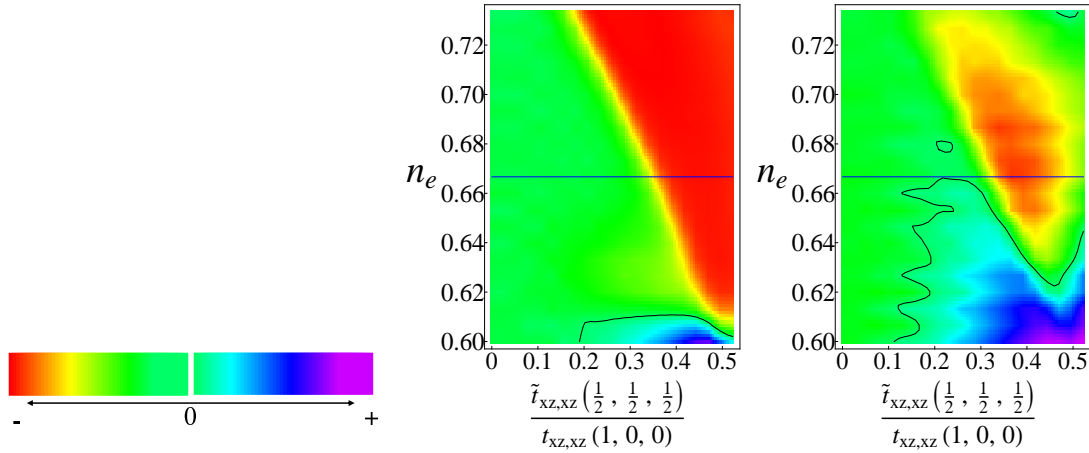


Figure 9: (Color online) As for the Fig. 8 but for $\{d_{xz}, d_{yz}\}$ bands. The area inside the solid line corresponds to positive variation of the *DOS*.

The coefficient F_1 of the term proportional to M^4 is related to the instability towards a metamagnetic state according to its sign and amplitude.[66, 23] Indeed, the condition for the occurrence of a metamagnetic transition as a function of the magnetic field requires that the coefficient F_1 is negative assuming that the temperature is enough low that it is possible to neglect the contribution from the term $\sim R_1 T^2$. From equation (37), we have that if the relation $\frac{5c(T)[1-2\chi_0(T)I]}{6\chi_0(T)} < (\frac{g(T)}{4})^2 < \frac{2c(T)[1-2\chi_0(T)I]}{\chi_0(T)}$ holds for the amplitudes of the free energy coefficients, then the system may undergo a metamagnetic transition, moving from a paramagnetic state to another one at a given finite magnetization via a first order transition. It is worth pointing out that the dependence on the Coulomb interaction I of the previous relation makes accessible the metamagnetic regime especially in the vicinity of the paramagnetic to ferromagnetic Stoner transition.

It is possible to show from equation (34) that the maximum allowed critical metamagnetic field $h_{c,max}$, in unit of the Bohr magneton, is a function of the only quadratic and quartic terms of the free energy expansion as given by:

$$h_{c,max} \cong 1.2 \sqrt{\frac{(\frac{1}{2\chi_0(T)} - I)^3}{|g(T)|}}. \quad (59)$$

Hence, the critical metamagnetic field amplitude can be put in direct relation with the modification of the density of states at the Fermi level as well as on its curvature in such a way that at low temperature it decreases (increases) if the F_1 or $\rho(\varepsilon_F)$ amplitudes grow (get suppressed). Due to the structure of the free energy, the monotonic dependence of the metamagnetic critical field on $\rho(\varepsilon_F)$ and its derivatives still

holds for intermediate amplitudes in the range $[0, h_{c,max}]$. Concerning the amplitude of the critical magnetic field, the strength of the applied field is physically accessible only if the system is within the metamagnetic region of the phase diagram but close to a ferromagnetic instability.

The strategy we adopt is the following: we determine the amplitude of the *DOS* at the Fermi level and the strength of F_1 at the planar position where the defect is placed and nearby it, then we compare them to the values they assume in the uniform case in order to provide indications on the modification of the collective behaviour. This is done by determining the projections on the various bands that are present at the Fermi level for the single and the bilayer system in order to extract the orbital character of the contributions to the collective behaviour.

3.3 Results

Let us study the changes of the electronic structure at the defect and in its vicinity by focusing on the *DOS* at the Fermi level as well as on its curvature being related to the coefficient F_1 in the expansion of the magnetic free energy.

The evolution of the electronic structure around the Fermi level, both for the planar impurity and the neighbors, will be discussed in terms of the charge transfer amplitude and of the change of the total electron filling n_e in the Ru bands. Concerning the study in terms of the hopping amplitude, we have analyzed how the electronic structure for a given band is modified by changing the amplitude of the charge transfer along the $[\frac{1}{2}, \frac{1}{2}, \frac{1}{2}]$ direction. We notice that the t_{2g} bands can communicate across the interface within various charge transfer processes: since the xy band is mainly two-dimensional, the most relevant process involves the hybridization, via the apical oxygens, with the γz bands; on the other hand, (xz, yz) orbitals mainly link each other across the c -axis interface. For the renormalized *DOS* we focus on the modifications induced by the change in the main channels of communication across the interface for each band of the t_{2g} Ru sector. To simplify the study of the *DOS* we introduce a variable q that tunes the ratio between the symmetry allowed hopping contributions of the xy and the γz bands, evaluated with respect to the correspondent in-plane hopping parameters. Then, we take into account the changes of the electron density at the Ru site. This analysis can be performed in two possible way: i) it can be directly related to changes in the stoichiometry occurring at

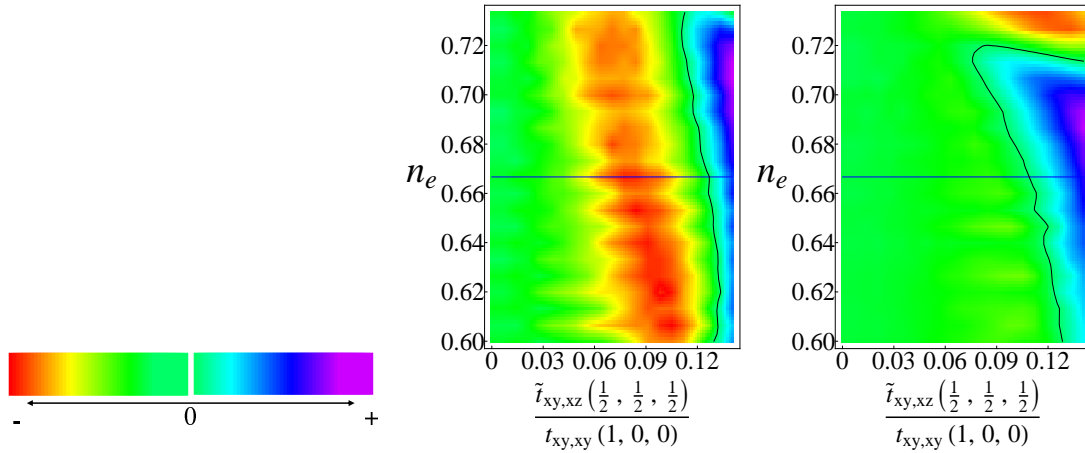


Figure 10: (Color online) Left panel depicts the contour map of the density of states for the d_{xy} band at the Fermi level for the $n = 1$ inclusion embedded in the $n = 2$ host. The DOS is normalized to that of the analogue band of the uniform bilayer. Right panel reports the DOS variation for the first neighbour of the defect, thus belonging to the host of $n=1$ type, with respect to that for the analogue band of the uniform single layered system. The map of the relative DOS variation is analyzed in terms of the total electron density and as a function of the charge transfer ratio across the $n=1$ and $n = 2$ interface. Top panel is the scale with maximum/minimum values of the order of about 2% with respect to the amplitude of DOS in the uniform case. The solid line is the locus of zeros (i.e. no change with respect to the uniform case) within the contour map. The area inside the solid line corresponds to positive variation of the DOS .

the interface, due to oxygen vacancies or other types of defects that might lead to valence fluctuations on the Ru ion; ii) it can be realized considering the modification of the total Ru density can be seen as an effective energy scan for the DOS above and below the Fermi level in the electron and the hole doping region.

We firstly consider the modification of the $\rho_{imp,\alpha,2}(\varepsilon_F)$ DOS at the Fermi level for the α band at the $n=2$ impurity embedded in the host of $n=1$ type, corresponding to the case represented in Fig. 7a). The DOS , renormalized to the value $\rho_{u,\alpha,2}(\varepsilon_F)$ taken at the Fermi level for the corresponding band of the uniform bilayer system, for the xy and the γz bands is then separately determined.

In the left panel of Fig. 8 it is reported the ratio $(\rho_{imp,xy,2}(\varepsilon_F) - \rho_{u,xy,2}(\varepsilon_F)) / \rho_{u,xy,2}(\varepsilon_F)$ for the d_{xy} band as a function of the charge transfer across the interface due to the hybridization of the xy and the γz bands at various filling (or effective energy shifts). As one can see, there is a slight decrease with a smooth variation as a function of the hopping ratio at the interface up to a value of about 0.1 above which the DOS

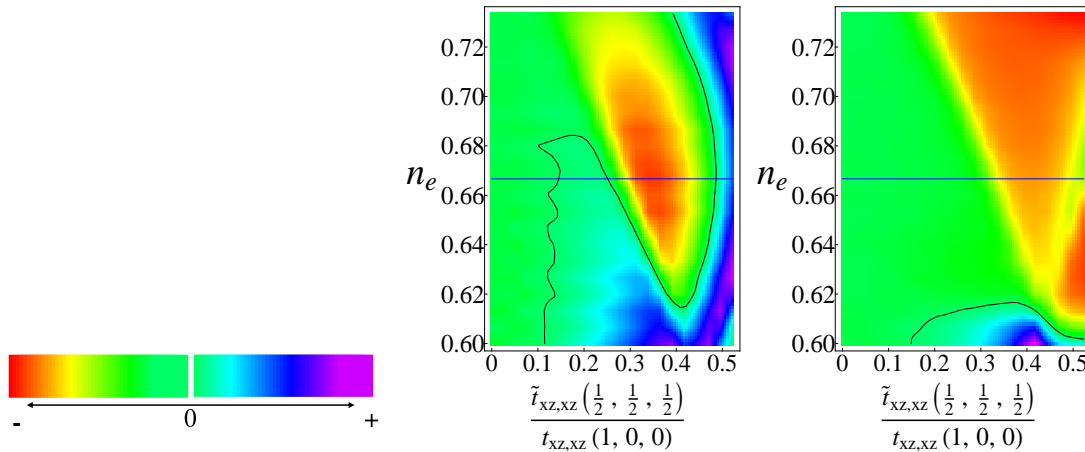


Figure 11: (Color online) As for the Fig. 10 but for $\{d_{xz}, d_{yz}\}$ bands. The area inside the solid line corresponds to positive variation of the DOS .

amplitude grows significantly both at the Fermi level and at energies (filling) above it. The regime where the renormalized DOS increases can be thought as a region where the structural change at the interface are such to yield a good interfacing between the inclusion and the $n = 1$ domain. Thus a larger ratio for the hopping matrix elements along the c -axis is required compared to the uniform systems. The large increase of the DOS ratio above the Fermi level can be ascribed the shift of the van Hove-like maximum in the density of states for the xy band due to the changes in the charge transfer across the interface between the two R-P members domains.

The modification of the DOS for the γz bands is completely different from the same quantity previously obtained for the xy band. because, close to the Fermi level, the DOS is always reduced, compared to the uniform bilayer system. However, there exists a small window, far from the Fermi level, where the DOS increases as for the case of the xy band, as consequence of the energy shifts of the Van Hove singularities in the quasi one-dimensional t_{2g} bands.

The behaviour of the electronic structure for the first neighbour to the $n=2$ inclusion is reported in the right panels of the Figs. 8, 9 for the xy and γz bands, respectively. As one can notice the xy DOS decreases in the whole range of the parameters space and it shows a significant reduction already in the regime where the ratio of the interface hopping to the in-plane one becomes larger than about 0.06. On the contrary, the normalized DOS for the γz bands does not change much at the Fermi level, up to a value of the charge transfer ratio of about 0.3; above this value it exhibits a significative reduction. We may conclude that an increase (a decrease) of the renormalized DOS with respect to the uniform case occurs above (below) the

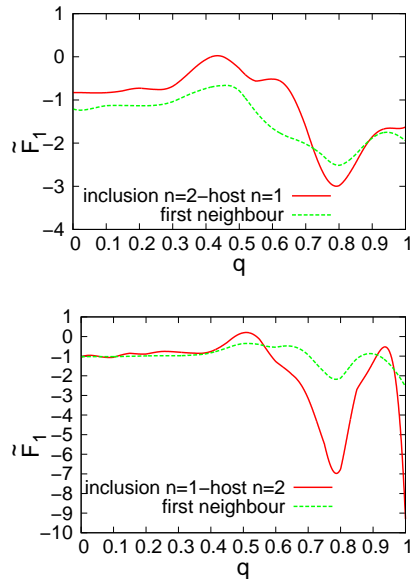


Figure 12: Evolution of the amplitude \tilde{F}_1 as a function of the ratio between the hopping $\tilde{t}(1/2, 1/2, 1/2)$ and the corresponding planar one, as parameterized by q . \tilde{F}_1 is the value of the coefficient F_1 at a specific position normalized to its strength for the correspondent uniform phase.

Fermi level, respectively.

Therefore, if we look at the modifications at the inclusion and near to it, for the $n = 2$ impurity embedded in the $n = 1$ host, the change in the *DOS* is orbital and position dependent. In the regime of bad/normal interfacing between the inclusion and the $n = 1$ domain, the renormalized *DOS* is always suppressed for the inclusion and its first neighbour both for the xy and γz bands. On the other hand, in a regime of good matching at the host-inclusion interface, only the renormalized *DOS* for the xy band has a significant enhancement at the Ru site placed in the $n = 2$ inclusion.

The results for the $n = 1$ inclusion interfaced to the $n = 2$ type domain, corresponding to configuration depicted in Fig. 7b), are reported in Figs. 10, 11. As one can notice, the renormalized *DOS* for the xy band (Fig. 10) of the $n = 1$ inclusion within the $n = 2$ host gets firstly reduced as the charge transfer is varied from the regime of bad interfacing towards that of good matching along the c -axis. In this last case, there is a significant increase of the *DOS* when the effective charge transfer amplitude overcomes the value of about 0.1. Such behaviour turns out to be quite insensitive to the change in the electron filling at the Ru site or equivalently in the energy region around the Fermi level, both above and below it. The γz bands for the Ru atoms at the $n = 1$ inclusion exhibit a similar trend though with

Table 2: Tendency to strengthen or weaken the ordered configurations due to the presence of monolayer (bilayer) defects in a bilayer (monolayer) host, respectively. The criteria are based on the evolution of the density of states at the Fermi level and on its curvature around the Fermi level. \nearrow (\searrow) indicates the increase (decrease) of the tendency to get ordered for the different broken symmetry solutions. $\nearrow\text{--}\searrow$ stands for a non-monotonous behaviour.

Bad interface regime ($q \rightarrow 0$)	n=2 impurity/n=1 host				n=1 impurity/n=2 host			
	Single layer		Bilayer		Single layer		Bilayer	
	$d_{\gamma z}$	d_{xy}	$d_{\gamma z}$	d_{xy}	$d_{\gamma z}$	d_{xy}	$d_{\gamma z}$	d_{xy}
Superconductivity(BCS)	\searrow	\searrow	\searrow	\searrow	\searrow	\searrow	\searrow	\searrow
Ferromagnetism(Stoner)	\searrow	\searrow	\searrow	\searrow	\searrow	\searrow	\searrow	\searrow
Metamagnetism		\nearrow		\searrow	$\nearrow\text{--}\searrow$	\searrow	$\nearrow\text{--}\searrow$	\searrow

Good interface regime ($q \rightarrow 1$)	n=2 impurity/n=1 host				n=1 impurity/n=2 host			
	Single layer		Bilayer		Single layer		Bilayer	
	$d_{\gamma z}$	d_{xy}	$d_{\gamma z}$	d_{xy}	$d_{\gamma z}$	d_{xy}	$d_{\gamma z}$	d_{xy}
Superconductivity(BCS)	\searrow	\searrow	\searrow	\nearrow	\nearrow	\nearrow	\searrow	\nearrow
Ferromagnetism(Stoner)	\searrow	\searrow	\searrow	\nearrow	\nearrow	\nearrow	\searrow	\nearrow
Metamagnetism		\nearrow		\nearrow	\nearrow	\nearrow		\nearrow

a non-monotonous behaviour, changing from positive to negative when the hopping amplitude is varied, thus indicating a more subtle dependence on the interface matching between the inclusion and the host. Further, the oscillatory effect is quite stable around the Fermi level.

Concerning the first neighbour of the $n = 1$ inclusion, we notice that, while the DOS for the xy band has a behaviour qualitative similar to that of the same band at the Ru site of the inclusion, the γz ones exhibit a different behaviour again pointing to the possibility of an inhomogeneous spatial tendency in the setting of broken symmetry configurations. In particular, the renormalization of the DOS for the γz orbitals is always negative getting significantly suppressed at large values of the effective interface hopping.

The overall change of the DOS at and near the inclusion is the result of a subtle interplay between the electronic structure mismatch at the interface, the different Fermi surface between the inclusion and the host, as well as the charge redistribution within the different bands in the two domains to keep the local charge homogeneity.

To move further in the analysis, we have considered the change of the curvature at the Fermi level by evaluating the ratio \tilde{F}_1 between the amplitude of the coefficient F_1 in the expansion of the free energy for the *DOS* at the inclusion and close to it normalized to the absolute value of the uniform solution $|F_1(n=1)|$ or $|F_1(n=2)|$, both for the monolayer and the bilayer systems, respectively. For the analysis we have followed the same procedure as that for the normalized *DOS*. However, we noticed that, due to the symmetry of the t_{2g} bands, the overall behaviour can be captured and summarized in a more convenient way by introducing a single parameter q that may tune, at the same time, the ratios $\tilde{t}_{xy,xz}(\frac{1}{2} \frac{1}{2} \frac{1}{2})/t_{xy,xy}(100)$ and $\tilde{t}_{xz,xz}(\frac{1}{2} \frac{1}{2} \frac{1}{2})/t_{xz,xz}(100)$. With this parameterization, we may scan different interesting cases, moving from the bad charge transfer conditions, at the inclusion-host interface ($q \rightarrow 0$), to the extreme situation of high hopping amplitude through the interface ($q \rightarrow 1$).

Fig. 12 reports \tilde{F}_1 , as a function of q , for the case of the $n=1$ inclusion in the $n=2$ host and viceversa, both evaluated at the inclusion and in its vicinity. We have also determined the orbital dependence of F_1 by projecting its amplitude on the different t_{2g} bands of the Ru atoms at the inclusion and in the host. The effects on the curvature for the case of the $n=1$ inclusion in the $n=2$ host are not significantly modified with respect to the uniform case at small q . In the intermediate regime ($q \sim 0.5$), \tilde{F}_1 , evaluated at the inclusion, tends to be zero or positive, while that for its neighbour stays negative. This means that in such region, the inclusion tends to lose the possibility to exhibit a metamagnetic behaviour due to its sign change, whereas the modification of the bands close is still compatible with a metamagnetic transition. It is interesting to notice that for such regime the possibility of a quantum tricritical behaviour may emerge, if the quadratic coefficient is also tuned in proximity of a paramagnet-ferromagnet transition.

For larger values of q , \tilde{F}_1 becomes again negative with a large renormalization compared to the uniform value. On a general ground, we may conclude that the increase of the amplitude with respect to the uniform case means that the system can exhibit a metamagnetic transition at a critical magnetic field having a smaller threshold.

The trend for the case of the $n=2$ inclusion in the $n=1$ host is similar to the previous one with the exception of the small q regime where, if compared to the uniform solution, the normalized coefficient is larger (smaller) at the inclusion (host), respectively. This means that the effects of the inclusion in the host is to modify the amplitude of the critical field in the opposite direction for the inclusion and its first neighbour.

A summary of the possible consequences of the electronic structure modification of the *DOS* at the Fermi level, with respect to the onset or the change of the collective behaviour

for the eutectic system compared with the uniform one, is reported in the Table 2. In this Table, we have sum up the trend of the broken symmetry configurations for the different Ru bands evaluated at the inclusion and at the first neighbour of the inclusion within the host. The broken symmetry states considered are the ferromagnetic, the superconducting and the metamagnetic ones as discussed in Sect. II. Therefore, assuming for example that the uniform $n = 1$ or $n = 2$ system exhibits a ferromagnetic or a superconducting ordering, according to the dependence of the critical temperature within the BCS picture or the quantum critical point associated to the ferromagnet-paramagnet transition within the Stoner, the change in the *DOS* may reinforce or hinder the stability of the broken symmetry states under investigation.

Let us then discuss the tendency toward the metamagnetism. The result previously obtained for the total *DOS* can be decomposed within the different orbital channels. In this way it is possible to understand which bands is responsible for the metamagnetic behaviour. We also notice that the orbital dependence plays an important role when one wants to infer the anisotropic character of the metamagnetic response as due for example to spin-orbit coupling. The results obtained reveal that the metamagnetic response, differently from the case of the ferromagnetic and superconductor orders, is much more sensitive to the type of the inclusion with respect to the host, to the orbital where the electrons couple to lead to the metamagnetic response upon an applied field, as well as to the strength of the charge transfer amplitude. As a general remark we point out that the critical magnetic field decreases for the case of good inclusion-host matching, while for the bad interface regime between host and inclusion behaves differently leading to a distribution of critical magnetic fields above which the system discontinuously reaches a non zero magnetization.

3.4 Conclusions

In conclusion we have studied the modification of the electronic structure induced at the interface between the $n=1$ inclusion and the $n=2$ domain and viceversa as due to changes of the charge transfer across the interface and in terms of possible modification of the Ru electronic density. We have connected the behaviour of the *DOS* at the Fermi level and the modification of its curvature to the criteria for the strengthening or hindering of ordered states as superconductivity, ferromagnetism and metamagnetism close to the inclusion compared to the behaviour for the uniform system. The analysis has shown that the changes of the *DOS* at the Fermi level is orbital dependent for the three Ru bands and the behaviour is not always concorde between the different t_{2g} bands. In particular

depending on the level of interbands matching at the inclusion-host interface the orbital dependent DOS can get suppressed or significantly enhanced.

The results here presented indicate that if the charge transfer processes are inhibited at the interface between the inclusion and the host, i.e. in the regime of $q \rightarrow 0$, then the general trend for all the bands is to have a suppression of the DOS at the Fermi level both at the Ru sites in the inclusion and in its vicinity, meaning that both the ferromagnetism and the superconductivity are inhibited. Otherwise, for the case of good matching at the inclusion-host interface the tendency is dependent on the orbital involved and on the position of the Ru site. Indeed, both for the $n=1$ impurity in the $n=2$ host and viceversa, the DOS of all the t_{2g} bands in the single layer increase with respect to the uniform case, while in the neighbour $n=2$ unit cell the DOS grows for the d_{xy} band but it is suppressed for the γz ones. This behaviour can be interpreted as a possible strengthening of the ferromagnetism or the superconductivity only at the inclusion or in its vicinity if the electrons that tend to form the ferromagnetic or superconducting order belong to the xy band.

Concerning the curvature changes compared to the uniform solution, both at the inclusion and in its vicinity the effects on the DOS first and second derivative can lead to a large increase of the coefficient of the M^4 term of the free energy expansion that is related to a significant modification of the metamagnetic response. There is an interesting regime where the coefficient of the quartic term tends to zero leading to a possible emergence of a quantum tricritical behaviour.

Let us consider the connection between the presented results and the experimental observations in the eutectic system made of interfaced $n=1$ and $n=2$ domains both at the micrometric and the nanometric scale.

Concerning the superconducting behaviour the $Sr_3Ru_2O_7$ domain cut from the eutectic has been shown to exhibit an unusual temperature and magnetic field dependence below an onset temperature that is above the nominal superconducting transition $T_c \sim 1.5$ K of the "pure" Sr_2RuO_4 single phase compound.[57] The modification of the onset T_c is an issue that has been already established in the Sr_2RuO_4 -Ru eutectic where micrometric metallic islands of Ru are embedded in the Sr_2RuO_4 single phase and the superconductivity occurs already at about 3 K in the region in the vicinity of the Sr_2RuO_4 -Ru interface. [49, 67] Similar effects are also induced by the uniaxial pressure on *pure* Sr_2RuO_4 leading to an onset T_c above 3 K.[68] This emphasizes the role played by structural changes and octahedral distortions as driving forces to induce a change of the superconducting state in the eutectic systems made of Sr_2RuO_4 phase as one of its constituents. In this context,

recent electric transport and muons measurements in the $\text{Sr}_2\text{RuO}_4/\text{Sr}_3\text{Ru}_2\text{O}_7$ eutectic have confirmed the occurrence of superconductivity at a temperature that is higher than that observed in the *pure* Sr_2RuO_4 with an onset of about 2.5 K. [69] Though the origin and the mechanisms for the superconducting behaviour in the $\text{Sr}_2\text{RuO}_4/\text{Sr}_3\text{Ru}_2\text{O}_7$ eutectic are still under debate, similarly to what has been deduced for the Sr_2RuO_4 -Ru system or in the *pure* Sr_2RuO_4 upon uniaxial pressure, it is plausible that the superconducting state nucleates at the interface between the $n=1$ and $n=2$ domain as well as in the proximity of it.

Within our analysis we can address the increase of the onset critical temperature by assuming that a single layer embedded in the $n=2$ domain exhibits an increase of the density of states at the Fermi level both for the xy and γz bands in the regime of good $n = 1-n = 2$ interfacing or for enhanced charge transfer across the $\text{Sr}_2\text{RuO}_4/\text{Sr}_3\text{Ru}_2\text{O}_7$ interface. The lack of first-principles calculations of the structural and electronic properties at the $\text{Sr}_2\text{RuO}_4/\text{Sr}_3\text{Ru}_2\text{O}_7$ interface does not allow one to have a quantitative estimate of the octahedral relaxation and the effective charge-transfer in the vicinity of the interface. Nevertheless, one might expect different effects to occur cooperatively at the interface in such a way to achieve a regime of enhanced charge transfer amplitude. The good in-plane lattice mismatch[58] can be one of the reason for good interfacing along the c -axis. Moreover, both the reduction of the in-plane bandwidth, due to rotation and tilting of the octahedra and the reduced dimensionality, as well as the renormalization of the interband hopping across the interface, due to the c -axis mismatch between the $n=1$ and $n=2$ phases and the variation of the apical oxygens positions, can lead an increase of the effective hopping across the interface.

About the magnetic properties, preliminary measurements on the $\text{Sr}_2\text{RuO}_4/\text{Sr}_3\text{Ru}_2\text{O}_7$ eutectic, with a majority of $\text{Sr}_3\text{Ru}_2\text{O}_7$ and a small percentage of dispersed $n=1$ phase, have shown a small downward shift of the metamagnetic critical field to lower values than those of the *pure* $\text{Sr}_3\text{Ru}_2\text{O}_7$ with a magnetic field applied in the ab plane.[70] As pointed out above for the superconducting case, this observation may find an explanation in the regime of good c -axis interfacing. Indeed, taking into account that the critical field depends on the ratio between the DOS at the Fermi level and its curvature via the coefficient F_1 , it is possible to deduce a reduction of the critical magnetic field when both the *DOS* and the F_1 coefficient grow as reported in the Table 2. In this framework we do expect that depending on the interface achieved in the eutectic system the metamagnetic critical field can either grow (i.e. in the intermediate regime) or decrease in amplitude if compared to the case of the *pure* $\text{Sr}_3\text{Ru}_2\text{O}_7$.

Due to the spatial dependence of the *DOS* variation and its derivatives at the inclusion

and in its vicinity our results also indicate a tendency to an inhomogeneous magnetism in the eutectic system with a possible distribution of critical metamagnetic fields. Hence, a broadening of the first order transition can occur even at very low temperature where a sharp change in the magnetization is expected. This behaviour might represent an hallmark of the magnetic response for the $\text{Sr}_2\text{RuO}_4/\text{Sr}_3\text{Ru}_2\text{O}_7$ eutectic.

4 Metamagnetism of itinerant electrons: the realistic case of multy-layer ruthenates

We study in detail the influence of the electronic correlation on electronic structure of nanometric inclusions of Sr_2RuO_4 embedded as c -axis stacking fault in $Sr_3Ru_2O_7$ and viceversa. The metamagnetic properties in mean field theory approach using the realistic density of state are analyzed.

4.1 Introduction

The issue of metamagnetism in itinerant electron systems was studied both theoretically [66] and experimentally [71] long ago. The magnetic phase diagrams of itinerant electron systems show both thermal and quantum phase transitions, and often non-Fermi-liquid behaviour associated with quantum critical endpoints. Recently, the problem of quantum criticality in the context of itinerant ferro- or metamagnetism has received considerable attention [22, 72, 73], considering it from a new point of view. It has been suggested that these systems might display a new type of quantum criticality, connected with a so-called quantum critical end-point (*QCEP*), in the vicinity of which the Landau Fermi-liquid theory of metals breaks down.

The $Sr_3Ru_2O_7$ compound displays a metamagnetic transition which bifurcates as a function of field angle to enclose an anomalous phase where the transport properties break the symmetry of the crystal lattice[74, 75]. Intriguingly, this phase has been shown to have a higher entropy than the surrounding normal phases[76], contrary to naive expectations. The metamagnetism and anomalous phase are generally thought to be caused by the presence of a van Hove singularity just below the Fermi surface in one of the electronic bands of the material[40, 23, 77, 78]. It is also a key ingredient of mean field treatments of the anomalous phase such as the nematic instability[79, 80, 81, 82, 83]. However, the quantum critical endpoint in the region of the anomalous phase[22] and the possible role of this critical point remains largely unexplored. In addition, the region around the phase shows signatures which may be attributed to the quantum critical point, such as a diverging entropy and specific heat. Also the dependence of the metamagnetic transition on field angle, as well as doping [84] and scanning tunneling microscope [85] studies, have cast doubt on the simple picture of a fixed band structure with the field acting to Zeeman split the spin species through a peak in the density of states. Theoretical results concerning the properties of the *QCEP* have been obtained on the basis of phenomenological, low-energy

field theories [86]. These issues raise the question of how far the properties of the material may be explained by the density of states, without involving quantum fluctuations or more exotic physics.

Some authors [23, 87] presented a mean field theory of uniform magnetism for itinerant electrons with Fermi energy close to a *VHS* in the context of multilayer ruthenates. The resulting phase diagram features first- and second-order ferromagnetic transitions, as well as a line of (metamagnetic) critical end-points, which is pushed to zero temperature at a *QCEP*. One of the characteristic features of $\text{Sr}_3\text{Ru}_2\text{O}_7$ is an unusual phase with a higher entropy than its surroundings. They consider how this may arise in the context of a density of states picture and finds that it is possible to reproduce the thermodynamic behaviour and first-order phase transitions.

We show, based on a mean field theory, that the low-temperature behaviour of the n -layer ruthenates $\text{Sr}_{n+1}\text{Ru}_n\text{O}_{3n+1}$ can be understood as a result of the presence of a Van Hove Singularity (*VHS*) near the Fermi level. We would like to emphasize that the origin of this behaviour lies in the band structure. We will not consider instabilities toward other phases such as the nematic or spin spiral but will concentrate on the bare homogeneous metamagnetic transition. We will consider how these results may help to identify the cause of the metamagnetic transition in $\text{Sr}_3\text{Ru}_2\text{O}_7$ and may more generally help to distinguish between *DOS* features and quantum critical effects. Differently from other papers that used similar strategy, we will use a realistic *DOS* from ab-initio hopping parameters calculated in Chapter 3. In the first paragraph, we will introduce the three bands Hubbard model and the effective degrees of freedom generalizing the Stoner criterion. In the second paragraph, we will calculate the magnetization versus Coulomb repulsion for Sr_2RuO_4 , $\text{Sr}_3\text{Ru}_2\text{O}_7$ and the system with one Sr_2RuO_4 impurity embedded in the $\text{Sr}_3\text{Ru}_2\text{O}_7$ host and viceversa.

4.2 Metamagnetism in three band Hubbard model

Let us consider the homogeneous system, it is possible to generalize the same topic in the non homogeneous case. We use the same notation of Chapter 3 for the Hamiltonian describing our system. We add the three band Hubbard model to the single particle Hamiltonian (50):

$$\hat{H} = \sum_{\sigma\{\mathbf{i},\mathbf{d}_n\}} \sum_{\{\lambda,\nu\}} t_{\lambda\nu}(\mathbf{d}_n)(\hat{c}_{\mathbf{i}\lambda\sigma}^\dagger \hat{c}_{\mathbf{i}+\mathbf{d}_n\nu\sigma} + h.c.) - \mu \sum_{\mathbf{i}\lambda\sigma} \hat{n}_{\mathbf{i}\lambda\sigma} + U \sum_{\mathbf{i}} \sum_{\lambda} \hat{n}_{\mathbf{i}\lambda\uparrow} \hat{n}_{\mathbf{i}\lambda\downarrow} \quad (60)$$

If we consider the pure system Sr_2RuO_4 , we can diagonalize the single-particle Hamiltonian to have

$$\hat{H} = \hat{H}_\alpha + \hat{H}_\beta + \hat{H}_\gamma + U \sum_{\mathbf{i}} \sum_{\lambda=xy,xz,yz} \hat{n}_{\mathbf{i}\lambda\uparrow} \hat{n}_{\mathbf{i}\lambda\downarrow} \quad (61)$$

where α, β and γ are the bands that generate the three strongly two-dimensional sheets in the Fermi surface [30]. We are able to decouple the single-particle Hamiltonian in terms of occupation numbers $n_{\alpha\sigma}$, $n_{\beta\sigma}$ and $n_{\gamma\sigma}$, but we are not able to express the Hubbard term respect to occupation number of the diagonalized band. The thermodynamic potential will not a sum of single band potential. For this reason, the system is complicated by multiband effects.

We will calculate the complete mean field theory of three band Hubbard model without approximation, considering symmetry-constrained to reduce the degrees of freedom. In mean field approximation, the thermodynamic functional generated from (60) depends from the 6 occupation numbers (we have three bands with two spin channels). We impose the geometrical symmetry and fix the filling.

$$n_{xz\uparrow} = n_{yz\uparrow} \quad (62)$$

$$n_{xz\downarrow} = n_{yz\downarrow} \quad (63)$$

$$n_e = \sum_{\alpha,\sigma} n_{\alpha,\sigma} = 4 \quad (64)$$

Now, we have 3 degrees of freedom and the system is composed by 2 effective bands (d_{xy} and $d_{\gamma z}$). We choose these degrees of freedom: the magnetization for the two bands and the polarization p .

$$M_{xy} = \frac{n_{xy\uparrow} - n_{xy\downarrow}}{2} \quad (65)$$

$$M_{\gamma z} = \frac{n_{\gamma z\uparrow} - n_{\gamma z\downarrow}}{2} \quad (66)$$

$$p = \frac{(n_{\gamma z\uparrow} + n_{\gamma z\downarrow}) - (n_{xy\uparrow} + n_{xy\downarrow})}{2} \quad (67)$$

Let us consider the paramagnetic phase, where the two magnetizations are zero and there is just one degree of freedom that is the polarization. From ab-initio calculation, the degree of freedom p is around 0.14 for Sr_2RuO_4 .

$$M_{xy}(U=0) = 0 \quad (68)$$

$$M_{\gamma z}(U=0) = 0 \quad (69)$$

$$p(U=0) \approx 0.14 \quad (70)$$

Similar values are found for $\text{Sr}_3\text{Ru}_2\text{O}_7$ and the for the non homogeneous cases. When the repulsion increases in the non magnetic case, we polarization goes to zero to minimize the energy of the system described by (60):

$$M_{xy}(U \longrightarrow +\infty) = 0 \quad (71)$$

$$M_{\gamma z}(U \longrightarrow +\infty) = 0 \quad (72)$$

$$p(U \longrightarrow +\infty) = 0 \quad (73)$$

Instead, when the repulsion increases in the magnetic case, the system becomes completely polarized ($n_{\gamma z\uparrow} = n_{xy\uparrow} = 1$) and the only degree of freedom left is p . We observe from our calculation in the self-consistent solution, that p becomes smaller than the initial value. This effect gives rise to a charge flow from the γz bands to xy band, thereby shifting the xy VHS very close to Fermi energy.

$$M_{xy}(U \longrightarrow +\infty) = \frac{1}{3} - \frac{p}{2} \quad (74)$$

$$M_{\gamma z}(U \longrightarrow +\infty) = \frac{1}{3} + \frac{p}{2} \quad (75)$$

$$p(U \longrightarrow +\infty) \approx 0 \quad (76)$$

It was already observed that p decrease in static [88] and dynamical mean field theory [89] when Coulomb repulsion is added. This is a multiband effect not present in the Stoner criterion or single band models. The paramagnetic DOS $\rho_{xy}(\varepsilon_F, p(U))$ depends on U through p .

After the symmetry considerations, we have that any homogenous ruthenates system can be described by the thermodynamic functional $G(n_{\gamma z\uparrow}, n_{\gamma z\downarrow}, n_{xy\uparrow}, n_{xy\downarrow}, U)$. It was demonstrated that the electron-like sheet γ is dominantly d_{xy} [33]. If we identify the γ band with the xy band, we can consider the thermodynamic functional generated using mean field theory from Hamiltonian (61) like a sum of the d_{xy} part and $d_{\gamma z}$ part.

$$G(n_{\gamma z\uparrow}, n_{\gamma z\downarrow}, n_{xy\uparrow}, n_{xy\downarrow}, U) \approx G_{xy}(n_{xy\uparrow}, n_{xy\downarrow}, U) + G_{\gamma z}(n_{\gamma z\uparrow}, n_{\gamma z\downarrow}, U) \quad (77)$$

$$= G_{xy}(M_{xy}, p, U) + G_{\gamma z}(M_{\gamma z}, p, U) \quad (78)$$

But, the charge flow effect is again present and we need to neglect the dependence from p to have 2 complete decoupled potential for the two effective bands.

$$G(n_{\gamma z\uparrow}, n_{\gamma z\downarrow}, n_{xy\uparrow}, n_{xy\downarrow}, U) \approx G_{xy}(M_{xy}, p, U) + G_{\gamma z}(M_{\gamma z}, p, U) \quad (79)$$

$$\approx G_{xy}(M_{xy}, U) + G_{\gamma z}(M_{\gamma z}, U) \quad (80)$$

Using these approximations, we can decouple the system but we lose important effects. We will consider the full calculation having in mind that multiband effects plays a role just throw the polarization p .

We will neglect the octahedral distortions present in multilayer ruthenates and will focus on the xy band, supposed to be essential to understand the metamagnetic transition. If we do not consider the octahedral distortions in $Sr_3Ru_2O_7$, the xy DOS present a *VHS* in the same point of the Sr_2RuO_4 [90]. In the distorted case, the hopping $t_{xy,xy}^{100}$ decreases and the *VHS* goes below the Fermi level changing the *DOS*. Following our model and using the Stoner criterion, the d_{xy} band must be ferromagnetic for

$$U > U_{Stoner} = \frac{1}{\rho_{xy}(\varepsilon_F, U = 0)} \approx 1.7 \text{ eV} \quad (81)$$

but two effects reduce this value: the charge flow and the first order transition. The multiband effect make near the *VHS* to Fermi energy increasing $\rho_{xy}(\varepsilon_F)$ and the first order transition appears at U smaller than U_{Stoner} . Considering the multiband effect, we should obtain a second order transition at $U \approx 1.4 \text{ eV}$

$$U \rho_{xy}(\varepsilon_F, p(U)) = 1 \implies U \approx 1.4 \text{ eV} \quad (82)$$

Instead, we will see a first order transition at lower U .

4.3 $M(U)$ for ruthenates, role of Hubbard repulsion

In Chapter 2, we demonstrated that a jump in $M(U)$ creates a smaller jump in the $M(h)$ for an example with a single band model. It is possible to demonstrate this in general, but we do not show. In all the cases studied, we find a $M(U)$ function strictly increasing in the interesting regions as physically expected. We will have three phase: the paramagnetic at low U , the metamagnetic before the transition and the ferromagnetic phase. The calculation of the magnetic properties was never done before for realistic model $Sr_3Ru_2O_7$. We calculate the *DOS* from realistic model using the hopping parameter derived in the Chapter 3. We analyse the properties of the pure phases and the properties of the interfaces, studying the $M(U)$ function.

4.3.1 Metamagnetic properties of pure phases

The *DOS* of Sr_2RuO_4 contains the two contributions of the $d_{\gamma z}$ and d_{xy} part. There is a wider quasi-twodimensional xy , and two quasi-onedimensional bands of character γz .

The *VHS* near the Fermi energy belongs to the partial *DOS* of the d_{xy} band. The jump in the magnetization happens when the Fermi level goes from one side to the other of the *VHS* as we can see in Fig. 13 and Fig. 14. Since the hopping of the d_{xy} bands out of the plane are negligible, the Sr_2RuO_4 and $\text{Sr}_3\text{Ru}_2\text{O}_7$ d_{xy} bands are extremely similar in tetragonal case, so, the two densities of state are not extremely different.

Now, we demonstrate that is the d_{xy} to produce the metamagnetism. We analyse the system as a function of the Coulomb repulsion. In particular, we analyse the behaviour of

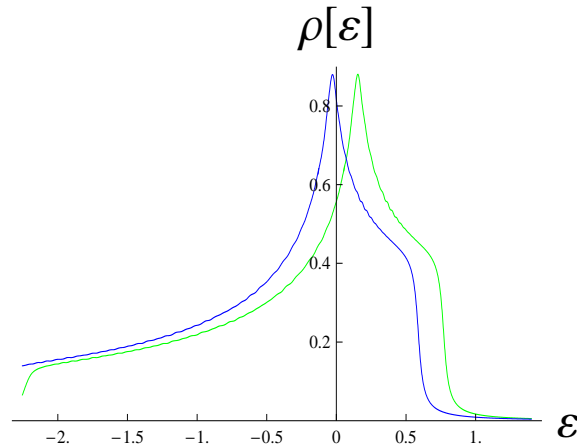


Figure 13: d_{xy} *DOS* of pure phase of Sr_2RuO_4 at $U=1.23$. The ferromagnetic transition happens at $U=1.22$. The Coulomb repulsion in mean field theory create a splitting of the density of state between the majority (blue line) and minority (green line) spin. The *VHS* create a jump in the magnetization.

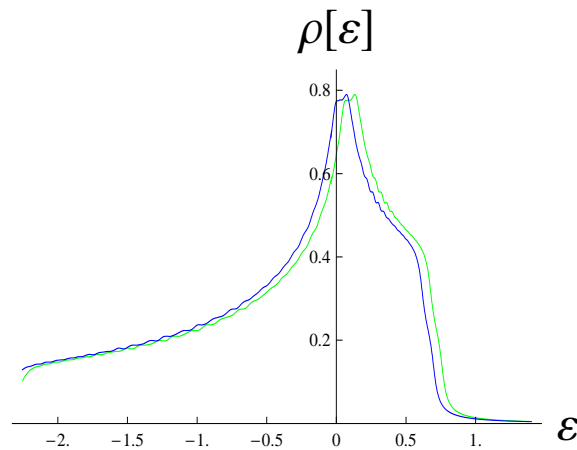


Figure 14: d_{xy} *DOS* of pure phase $\text{Sr}_3\text{Ru}_2\text{O}_7$ at $U=1.23$. The ferromagnetic transition happens at $U=1.22$. The Coulomb repulsion in mean field theory create a splitting of the density of state between the majority (blue line) and minority (green line) spin. The *VHS* create a jump in the magnetization.

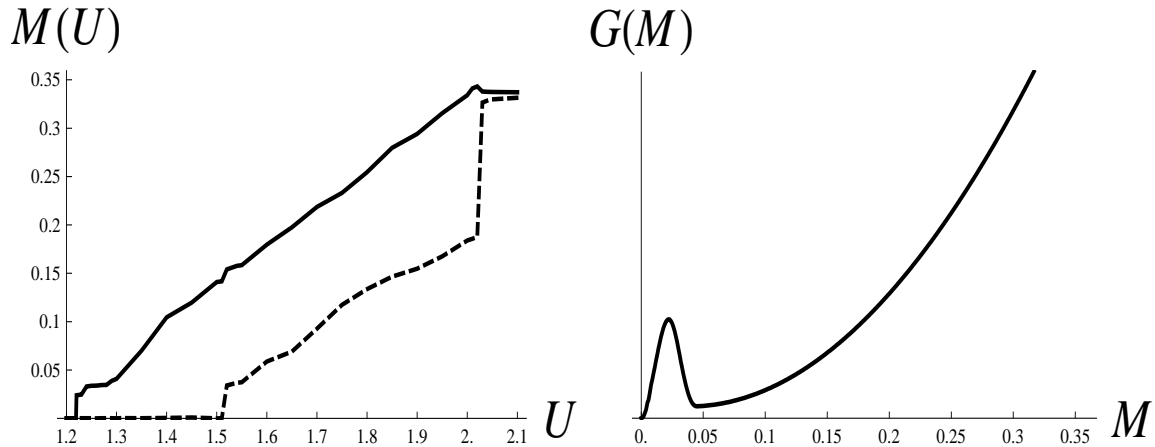


Figure 15: $M_{xy}(U)$ (solid line) and $M_{\gamma_z}(U)$ (dashed line) for the $\text{Sr}_3\text{Ru}_2\text{O}_7$ compound (left panel). Schematic behaviour of the thermodynamic potential able to reproduce this kind of jump in the magnetization.

the two magnetization degrees of freedom of the system $M_{xy}(U)$ and $M_{\gamma_z}(U)$ under the symmetry constraint in self-consistent way.

In Fig. 15 (left panel), we compute the evolution of the magnetization degrees of freedom as function of the Coulomb repulsion for the $\text{Sr}_3\text{Ru}_2\text{O}_7$. We see that the d_{xy} band produce the first jump in the magnetization at critical value of $U_{crit} = 1.22 \text{ eV}$. The experimental metamagnetic transition found in $\text{Sr}_3\text{Ru}_2\text{O}_7$ can be associated to the first jump of $M(U)$ due to the d_{xy} band. We showed in the Chapter 2, that the phase diagram can be separated in three phase: the paramagnetic phase at low U , the metamagnetic phase at value smaller than U_{crit} , and the ferromagnetic phase at $U > U_{crit}$. In the metamagnetic region we have a nearly ferromagnetic metal, the system is paramagnetic at zero magnetic field and jumps to the ferromagnetic minimum of the thermodynamic functional in applied magnetic field. In Fig. 15 (right panel), we put a schematic view of the thermodynamic potential that can create this kind of jump in the magnetization. We are not able to check how much is bigger the metamagnetic region but it is present for a value of U arbitrarily near U_{crit} . If the value of U for $\text{Sr}_3\text{Ru}_2\text{O}_7$ is around 1.20 eV , it is possible to have metamagnetic transition in applied magnetic field. This value of U is in good agreement with other values for not distorted ruthenates. It was found $U=1.0 \text{ eV}$ [91] and $U=1.2 \text{ eV}$ [92] for the cubic structure of SrRuO_3 by ab-initio technique. Other typical value used in the literature for Sr_2RuO_4 are $U = 1.2 - 1.5 \text{ eV}$ [93, 88, 89].

In Fig. 16 (left panel), we compute the evolution of the magnetization degrees of freedom as function of the Coulomb repulsion for the Sr_2RuO_4 . In Fig. 16 (right panel), we put a schematic view of the thermodynamic potential that can create this kind of jump in

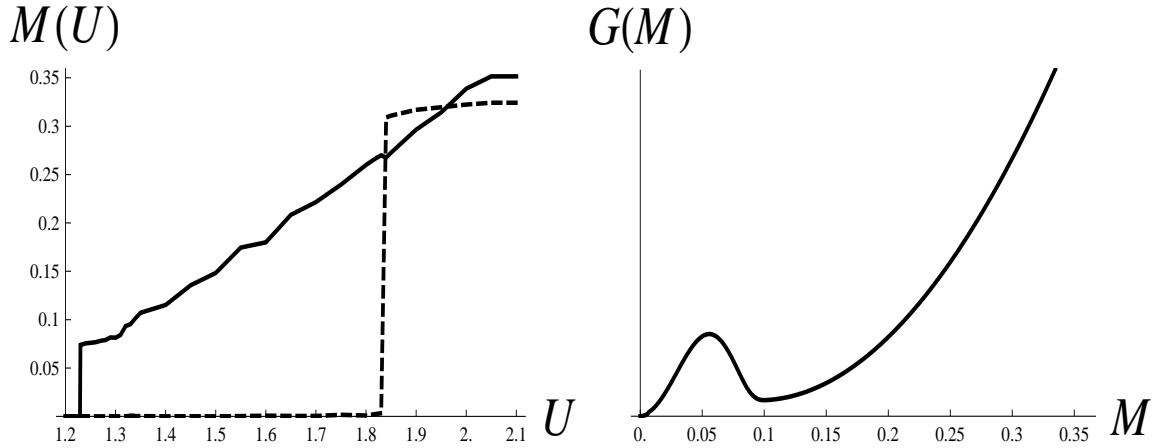


Figure 16: $M_{xy}(U)$ (solid line) and $M_{\gamma z}(U)$ (dashed line) for the Sr_2RuO_4 compound (left panel). Schematic behaviour of the thermodynamic potential able to reproduce this kind of jump in the magnetization.

the magnetization. The metamagnetism is not experimentally observed in Sr_2RuO_4 . The critical value of U for the Sr_2RuO_4 is $U_{crit} = 1.23 \text{ eV}$. There is a simple reason to explain this incongruity: the octahedral rotations in multilayer ruthenates reduce the bandwidth W increasing the ratio $\frac{U}{W}$ in $\text{Sr}_3\text{Ru}_2\text{O}_7$. The larger ratio $\frac{U}{W}$ for $\text{Sr}_3\text{Ru}_2\text{O}_7$ make possible the metamagnetism. It is interesting to observe, that we can recover the particular case of density of state of the one-dimensional tight binding studied in Chapter 2. The γz band is extremely similar to one-dimensional tight binding. We can observe that $M_{\gamma z}$ goes from a state with zero magnetization to a fully polarized state as expected. Using the formula:

$$\frac{U_{crit}}{t} = 2 \frac{2|\sin((1-n)\pi)| - \sin(2(1-n)\pi)}{(1-n)^2\pi} \quad (83)$$

calculated in Chapter 2, we can estimate the critical value of U for the first-order transition of the $d_{\gamma z}$ band at filling $n = \frac{2}{3}$. We find $\frac{U_{crit}}{t} = \frac{9\sqrt{3}}{\pi}$. Now, we consider that the bandwidth $W_{\gamma z}^{214}$ is approximatively $4t$, than $U_{crit} \approx \frac{W_{\gamma z}^{\text{Sr}_2\text{RuO}_4} 9\sqrt{3}}{4\pi} = 1.8 \text{ eV}$. This is in excellent agreement with our numerical result in Fig. 16 (left panel).

4.3.2 Magnetization at interface

We study the interface $\text{Sr}_2\text{RuO}_4/\text{Sr}_3\text{Ru}_2\text{O}_7$ using the same technicality breaking the invariance along the c -axis. We use periodic boundary condition and the hopping of the Sr_2RuO_4 bulk between the two phases to simulate the interfaces. The numerical simulation has been performed for a system having a total volume of $L_a \times L_b \times L_c$ with a number of sites for each direction given by $L_a = L_b = 140$ and $L_c = 32, 33$ (depending on the symmetry of the system). We have also modified the number of sites along the

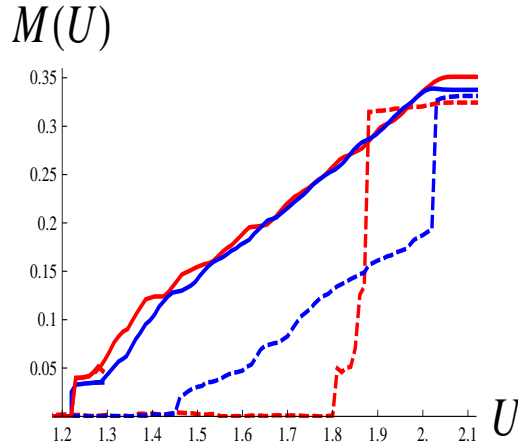


Figure 17: $M_{xy}(U)$ (solid lines) and $M_{\gamma z}(U)$ (dashed lines) for the system $\text{Sr}_2\text{RuO}_4/\text{Sr}_3\text{Ru}_2\text{O}_7$. The blue curves represent the magnetization of the $\text{Sr}_3\text{Ru}_2\text{O}_7$ host, while the red curves represent the Sr_2RuO_4 impurity.

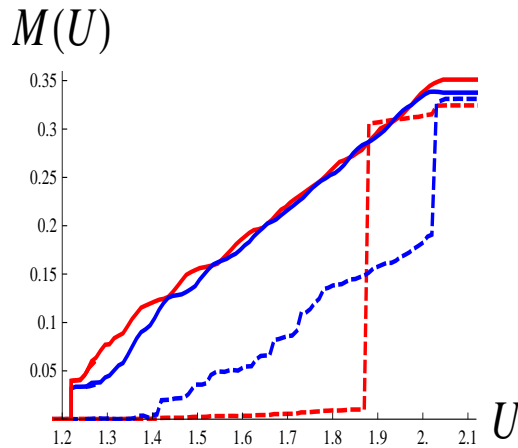


Figure 18: $M_{xy}(U)$ (solid lines) and $M_{\gamma z}(U)$ (dashed lines) for the system $\text{Sr}_2\text{RuO}_4/\text{Sr}_3\text{Ru}_2\text{O}_7$. The red curves represent the magnetization of the Sr_2RuO_4 host, while the blue curves represent the $\text{Sr}_3\text{Ru}_2\text{O}_7$ impurity.

c -axis to verify the dependence of the results by the boundary conditions. We study the host $\text{Sr}_3\text{Ru}_2\text{O}_7$ with an impurity of Sr_2RuO_4 and the host Sr_2RuO_4 with an impurity of $\text{Sr}_3\text{Ru}_2\text{O}_7$. The response of the impurity is not trivial. In both phases, the magnetization jump at $U_{crit} = 1.22$ eV differently from the pure phases. The $\text{Sr}_3\text{Ru}_2\text{O}_7$ induce a jump in the magnetization of Sr_2RuO_4 at U_{crit} smaller than the value of the Sr_2RuO_4 bulk. We can observe these results in Fig. 17 and 18. The system will have just one metamagnetic transition at lower critical metamagnetic field. An only one metamagnetic transition it is experimentally observed in some sample of $\text{Sr}_3\text{Ru}_2\text{O}_7 - \text{Sr}_4\text{Ru}_3\text{O}_{10}$ layered eutectic crystal [94].

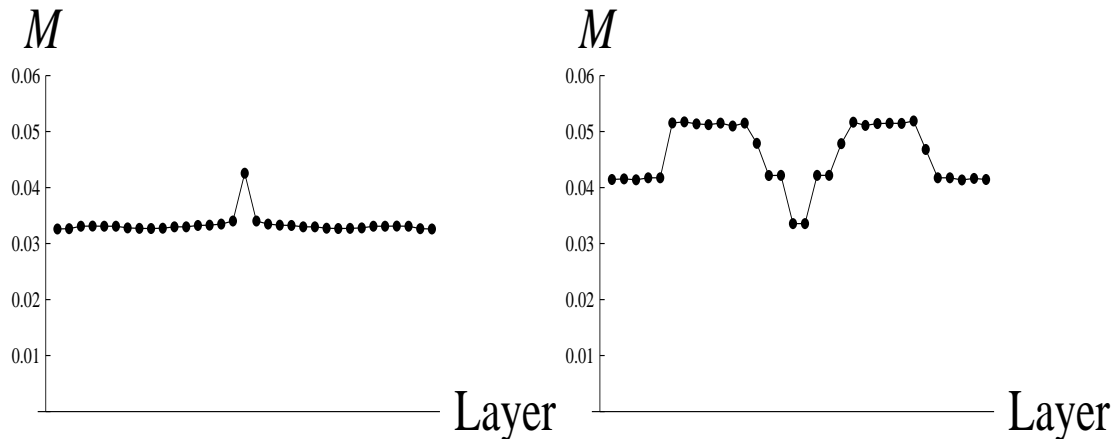


Figure 19: Magnetization in the real space at $U=1.23$ eV as a function of the layer for the $\text{Sr}_2\text{RuO}_4/\text{Sr}_3\text{Ru}_2\text{O}_7$ system. Magnetization of $\text{Sr}_3\text{Ru}_2\text{O}_7$ host with an impurity Sr_2RuO_4 (left panel) and viceversa (right panel).

In the pure phase, we have a homogenous magnetization. However, because of the interface, the homogenous magnetization is not a self-consistent solution. The $\text{Sr}_3\text{Ru}_2\text{O}_7$ host has a compact magnetic response as we can see in Fig. 19 (left panel), instead the Sr_2RuO_4 host is strongly inhomogeneous as we can see in Fig. 19 (right panel). This is due to the different hopping along the z -axis. The hopping intralayer in $\text{Sr}_3\text{Ru}_2\text{O}_7$ is so big, that second neighbour of the impurity can not see the impurity, so the response of the $\text{Sr}_3\text{Ru}_2\text{O}_7$ host to impurity is much more uniform and compact than the Sr_2RuO_4 host. The metamagnetism need to a compact response to magnetic field, that is not possible in Sr_2RuO_4 compound if it is not extremely pure. The results in Fig. 19 can not be related to the change of the DOS calculated in Chapter 3 at $U = 0$, because we have the Coulomb repulsion U that changes the polarization. The main influence of the host on the impurity is a change of the polarization. We find that the polarization p in Sr_2RuO_4 locally decreases near the interface. Because this, the Sr_2RuO_4 DOS increases in some region creating domain with higher magnetization respect to the bulk (right panel of Fig. 19).

4.4 Conclusions

We used ab-initio hopping parameters to make the density of state for tetragonal Sr_2RuO_4 and $\text{Sr}_3\text{Ru}_2\text{O}_7$. We show that both the systems can present metamagnetism. The possibility to have or to do not have metamagnetism critically depends from the Hubbard U . The purity of the sample Sr_2RuO_4 must be higher than the purity of $\text{Sr}_3\text{Ru}_2\text{O}_7$ to, eventually have metamagnetism. The metamagnetic transition of the system $\text{Sr}_2\text{RuO}_4/\text{Sr}_3\text{Ru}_2\text{O}_7$

can present quantitative differences from the pure phase behaviour, in particular, we find one metamagnetic crossover in this heterostructure. Finally, we comment that, although we have captured many of the qualitative features observed in multi-layer ruthenates, our model remains a relatively crude simplification. Here we have neglected several aspects, including spin-orbit coupling and rotation effects, which undoubtedly have a certain role in real materials. One of the most important questions concerns the effects of spin fluctuations, which are neglected within the mean field approximation. In the mean field approximation, there is no dependence from dispersion relation and from the shape of Fermi surface. The only important issue is the *DOS* and its derivatives at Fermi level. To overcome these simplifications, we can compute $M(U)$ ab-initio for the Sr_2RuO_4 and the $\text{Sr}_3\text{Ru}_2\text{O}_7$ compound tuning the octahedral distortion to improve the understanding of the phenomena.

5 Ab-initio study of the interface properties $\text{Sr}_2\text{RuO}_4/\text{Sr}_3\text{Ru}_2\text{O}_7$

We study the fermiology of Sr_2RuO_4 and $\text{Sr}_3\text{Ru}_2\text{O}_7$ from first principles: comparison, main features and a detailed analysis of the low-energy physics are performed. We show that the rotations in $\text{Sr}_3\text{Ru}_2\text{O}_7$ strongly reduce the first-neighbour hopping parameter between the d_{xy} orbitals, making near the Van Hove singularity to the Fermi level. Effect of the octahedral rotation and dimensionality are analyzed studying ab-initio the interface ruthenate $\text{Sr}_2\text{RuO}_4/\text{Sr}_3\text{Ru}_2\text{O}_7$. The geometrical rearrangement and the modification of the atomic bonds at the interface are shown.

5.1 Introduction

In recent years a lot of attention has been devoted to the study of interfaces made by transition metal oxides. The interest toward this topic is related to the fact that they offer a unique opportunity to test the interplay between many different electronic degrees of freedom. These interactions may produce several forms of symmetry breaking phases leading to novel and unexpected phenomena. Furthermore, the reduced dimensionality of the heterostructure may enhance the electronic correlations against the kinetic energy giving rise to novel effects that cannot be observed in bulk systems.

On the other hand, the possibility of synthesizing eutectic systems may open new routes to test the robustness of the ordered phases of the bulk components at the nanoscale, offering the occasion to check if the hybrid materials exhibit distinct properties from those of the pure bulk constituents. In this respect, the recently eutectically grown mixed ruthenate oxides represent a natural chance to address this issue. Indeed, ruthenate oxides of the Ruddlesden-Popper series (RP), given by the formula $\text{Sr}_{n+1}\text{Ru}_n\text{O}_{3n+1}$, display remarkable unconventional properties. Indeed, the $n = 1$ member of the series, i. e. Sr_2RuO_4 is a superconducting copper-free metal oxide showing an odd-parity spin-triplet pairing. The $n = 2$ member, $\text{Sr}_3\text{Ru}_2\text{O}_7$, exhibits unconventional magnetic properties being an enhanced Pauli paramagnet undergoing, at low temperatures, in anisotropic metamagnetic state. $\text{Sr}_4\text{Ru}_3\text{O}_{10}$, the $n = 3$ member of the RP shows ferro- or metamagnetic behavior depending on the direction of the applied magnetic field. Finally, the $n = \infty$ member SrRuO_3 is an isotropic ferromagnetic metal.

On the experimental side, it has been shown that the eutectic phase made by single-crystalline islands of pure Ru metal embedded in a single-crystal matrix of Sr_2RuO_4 , the

so called 3 Kelvin phase, reveals an onset of superconductivity at a temperature twice the critical temperature of pure oxide. The synthesis of $\text{Sr}_2\text{RuO}_4/\text{Sr}_3\text{Ru}_2\text{O}_7$ eutectic samples allows to show that this system exhibits unusual magnetic behavior as well as unconventional transport response. Surprisingly, susceptibility measurements on $\text{Sr}_3\text{Ru}_2\text{O}_7$ regions cut from the eutectic crystal, show an almost complete superconducting screening fraction. Nevertheless, the origin and the nature of the superconducting state in this eutectic compound is still an open question. Finally, it is worth mentioning that $\text{Sr}_4\text{Ru}_3\text{O}_{10}/\text{Sr}_3\text{Ru}_2\text{O}_7$ eutectic crystals have been successfully grown. [55] The properties of this material are not simply the sum of the two constituents. Indeed, in samples with a majority of the $n = 2$ RP member with respect to the $n = 3$, the system is ferromagnetic with magnetization along the c -axis and a single metamagnetic transition is observed at a critical magnetic field that is smaller to that obtained in the pure $\text{Sr}_3\text{Ru}_2\text{O}_7$ but greater than that in the $\text{Sr}_4\text{Ru}_3\text{O}_{10}$. [56]

However, very little theoretical results are until now available. Namely, for the 3 Kelvin phase a phenomenological theory has been proposed, whereas for the other eutectic combinations we may mention only the study devoted to the modification of the electronic structure induced by nanometric inclusions of Sr_2RuO_4 embedded as c -axis stacking fault in $\text{Sr}_3\text{Ru}_2\text{O}_7$. Here, we try to fill part of this gap proposing an ab-initio study of the $\text{Sr}_2\text{RuO}_4/\text{Sr}_3\text{Ru}_2\text{O}_7$ hybrid structures. We firstly study the electronic structure and the Fermi surface of the pure Sr_2RuO_4 and $\text{Sr}_3\text{Ru}_2\text{O}_7$ phases by using density functional theory (DFT). We remind that Sr_2RuO_4 has space group $I4/mmm$, whereas, due the rotations of the octahedra, $\text{Sr}_3\text{Ru}_2\text{O}_7$ presents an orthorhombic symmetry of space group Pbn . To study the heterostructure, we perform the full relaxation of the bulk Sr_2RuO_4 and $\text{Sr}_3\text{Ru}_2\text{O}_7$ phases, in such a way to construct the supercell of the hybrid $\text{Sr}_2\text{RuO}_4/\text{Sr}_3\text{Ru}_2\text{O}_7$ system. However, we would like noticing that standard DFT functionals overestimate the volume producing unacceptable ratio between c - and a - axis. [95] We find the same problem for these ruthenate oxides, especially for the $\text{Sr}_3\text{Ru}_2\text{O}_7$ phase. Thus, since we need accurate lattice constants in the study of the supercell made by these two RP members, we will use the exchange-correlation of Wu and Cohen, [96], a variant of generalized gradient approximation by Perdew *et al* (PBE) [97] method optimized for the relaxation of bulk systems. Referring to the estimated quantities, we have analyzed the low energy physics of the system calculating the hopping parameters and the modification of the location of van Hove singularity, which is related to the first-neighbor hopping between two orbitals d_{xy} .

The present chapter is organized as follows: In paragraph 2 we present some details concerning the numerical calculations, and in paragraph 3 we deal with the analysis of the achieved results, while the conclusions are reported in paragraph 4.

5.2 Computational details

We perform unpolarized first-principles density functional theory calculations [6] using the plane wave ABINIT package [9], the generalized gradient approximation (GGA) exchange-correlation functional of Wu and Cohen [96], and ultrasoft pseudopotentials [98]. We use a plane-wave energy cut-off of 80 Ry and a cold smearing of 0.045 Ry. These values for the plane-wave cutoff and the smearing are used in all calculations. As reported in the Introduction, we have firstly performed the calculation of the energy spectra for pure Sr_2RuO_4 and $\text{Sr}_3\text{Ru}_2\text{O}_7$ phases. Although, similar computations have already been realized, we have calculated these quantities to compare our results with the available data. In this way, we are confident that the results we will present for the hybrid structure correctly reproduce those for pure phases. An $8 \times 8 \times 8$ k-point grid is used for Sr_2RuO_4 , while a $8 \times 8 \times 2$ grid used for $\text{Sr}_3\text{Ru}_2\text{O}_7$ for the full relaxation. Furthermore, the $\text{Sr}_2\text{RuO}_4/\text{Sr}_3\text{Ru}_2\text{O}_7$ hybrid structures are studied with a $4 \times 4 \times 1$ k-point grid. We optimized the internal degrees of freedom by minimizing the total energy to be less than 10^{-8} Hartree and the remaining forces to be less than 10^{-4} Hartree/Bohr, and we require the external pressure to be less than 0.05 GPa to obtain the full relaxation of the system. Finally, to extract the character of the electronic bands at the Fermi level, we use the Slater-Koster interpolation scheme based on the maximally-localized Wannier functions method. [11] The k-point grid used for the Slater-Koster interpolation scheme is the same of the self-consistence for the bulk method, while a grid $10 \times 10 \times 1$ is used for the heterostructures.

5.3 Results

We study the electronic structure and the Fermi surface of the Sr_2RuO_4 and $\text{Sr}_3\text{Ru}_2\text{O}_7$ bulk phases by using density functional theory. We performed the full relaxation of the bulk Sr_2RuO_4 and $\text{Sr}_3\text{Ru}_2\text{O}_7$ to construct the supercell of the heterostructure $\text{Sr}_2\text{RuO}_4/\text{Sr}_3\text{Ru}_2\text{O}_7$. We compare the results at experimental atomic positions with the system after the full relaxation. Finally, we study the heterostructures with fully relaxed atomic positions and the electronic reconstruction at the interface.

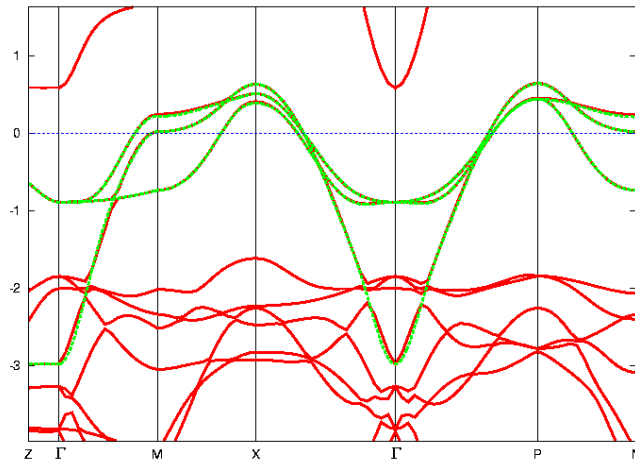


Figure 20: GGA (green line) and t_{2g} (red line) band structure of Sr_2RuO_4 . The e_g levels are 1 eV above the Fermi level. The Fermi level is set to zero.

5.3.1 Bulk Sr_2RuO_4 phase

The electronic structure of Sr_2RuO_4 has been already studied by several authors by means of DFT in local density approximation (LDA) or GGA. [30, 31, 36] The tetravalent Ru has four electrons in the 4d shell; the quasi-cubic crystal field splits the d levels into three-fold degenerate t_{2g} and two-fold degenerate e_g states. At Fermi level, four electrons belong to t_{2g} bands, while e_g bands are empty being higher in energy. DFT calculations show that the three t_{2g} bands can be divided in a wider quasi-two-dimensional xy , and two quasi-one-dimensional bands of γz character. While the first band slightly hybridizes with the other bands, the two bands xz and yz strongly hybridize between them, and the resulting bands are called α and β bands, whereas the band with strong character xy is called γ band. The flatness of the band structure at M point, shown in Fig. 20, produces a van Hove singularity (VHS) in the density of states (DOS) above the Fermi level. We have also calculated the maximally localized Wannier functions (MLWF) starting from the initial wave functions t_{2g} , finding that MLWF are coincident with the t_{2g} wave functions. The Fermi surface is displayed in Fig. 21, where it is shown that one sheet is hole-like (α) and the other two sheets, γ and β sheets, are electron-like. We notice that the γ sheet is nearly cylindrical in shape, and because the VHS is above the Fermi level, this sheet is electron-like. We have finally computed the hopping parameters, and reporting them in Table 1. We want to emphasize that the hopping $t_{xy,xy}^{100}$ is -0.3867 eV. This hopping is roughly proportional to the distance between the VHS from the bottom of the 3d band. If this hopping decreases, then the VHS goes towards the Fermi level.

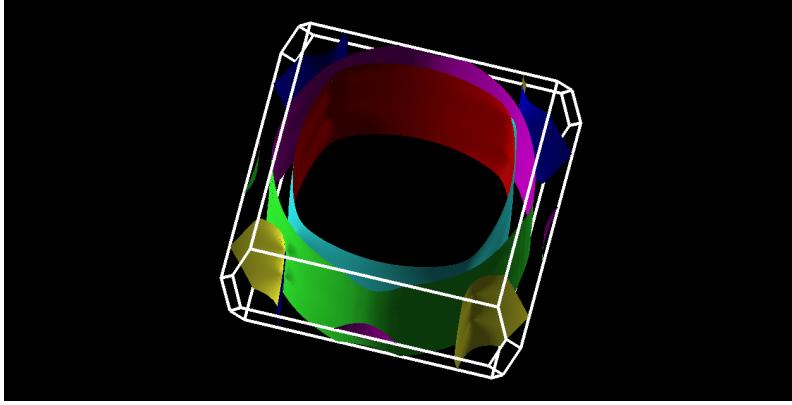


Figure 21: Fermi surface of Sr₂RuO₄. Three sheets are observed, and the small dispersion along the c -axis makes the system quasi-two-dimensional.

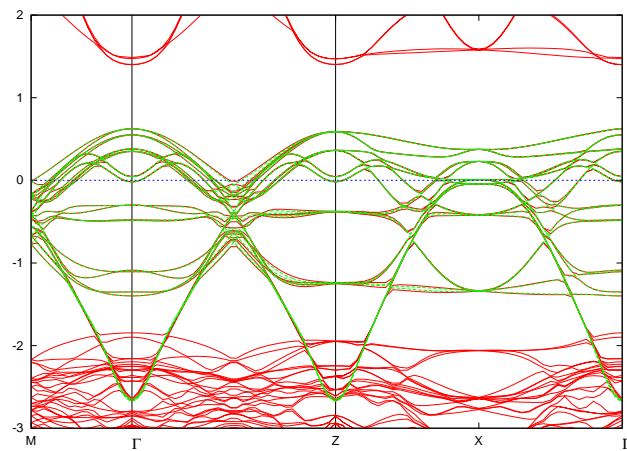


Figure 22: GGA (green line) and t_{2g} (red line) band structure of Sr₃Ru₂O₇. The e_g levels are 1 eV above the Fermi level. In this case, the position of the VHS is located at half of long direction Z- Γ (X point). The Fermi level is set to zero.

5.3.2 Bulk Sr₃Ru₂O₇ phase

We have performed a detailed analysis of the electronic structure of the bilayer Sr₃Ru₂O₇ for the case of fully distorted orthorhombic configuration. [99] To understand the character of the band at low energy, we have used the Slater-Koster interpolation scheme. As for the Sr₂RuO₄ case, the low energy physics is produced by the t_{2g} electrons, while the e_g electrons are again 1 eV higher in energy, as plotted in Fig. 22. The analysis of the band structure in Fig. 23 close to the Fermi level reveals a complex Fermi surface with multiple sheets having electron- and hole-like character. We notice that the topology and the volume of the Fermi surfaces here obtained are in good agreement with the recent high resolution experimental measurements obtained by means of angle-resolved photoemission. [40] In tetragonal environment, without rotation, the MLWF coincide with the t_{2g} bands when the Sr₂RuO₄ is considered. However, the MLWF of Sr₃Ru₂O₇ are different:

Table 3: Hopping integrals along the direction $[lmn]$ and on-site energy in eV associated to the three orbitals of the t_{2g} sector of the bulk $\text{Sr}_3\text{Ru}_2\text{O}_7$ in the t_{2g} basis. The unit is eV. In the MLWF basis, the hopping parameters differ at most of 0.001 eV. The connecting vector is expressed in terms of the integer set $[lmn]$ and the lattice constants a and c as $\mathbf{d} = la\mathbf{x} + ma\mathbf{y} + nc\mathbf{z}$ [9, 60, 11]. The direction $00d$ connect the two ruthenium atoms of the same cell. The hopping parameters that are zero in the tetragonal phase have sign dependent from the rotation (clockwise or anticlockwise). The hopping parameters $t^{\frac{1}{2}\frac{1}{2}\frac{1}{2}}$ can have different connections: depending from the rotations of the two octahedra the hopping parameter can increase, decrease or be similar to the hopping of Sr_2RuO_4 .

orbital index	amplitude							
	[000]	[100]	[010]	[110]	[200]	[020]	$[\frac{1}{2}\frac{1}{2}\frac{1}{2}]$	[00d]
$[lmn]$								
xy-xy	-0.482	-0.292	-0.292	-0.134	-0.021	-0.021	0.002/0.001	-0.018
yz-xy	0	± 0.010	± 0.010	± 0.001	± 0.002	± 0.006	0.006/0.005/0.004	0
xz-yz	0	± 0.010	± 0.010	± 0.001	± 0.006	± 0.002	0.006/0.005/0.004	0
yz-yz	-0.386	-0.020	-0.301	0.014	0.002	0.041	-0.023/-0.018/-0.014	-0.264
yz-xz	0	± 0.061	± 0.061	-0.013	± 0.007	± 0.007	-0.024/-0.015/-0.006	0
xz-xz	-0.386	-0.301	-0.020	0.014	0.041	0.002	-0.023/-0.018/-0.014	-0.264

the rotation of the octahedra strongly modifies the d_{xy} orbital as it can be checked looking at Table 3. Moreover, the hopping $t_{xy,xy}^{100}$ get smaller and VHS goes below the Fermi level. We have also analyzed the electronic charge associated with any band, and we find that, at Fermi level, the self-consistent charge of the band that originally has a d_{xy} character, tends to become similar to the $d_{x^2-y^2}$ charge just at Γ point where the hybridization is stronger.

This result allows to explain why many authors find appreciable weight of e_g electrons [90, 40], although no e_g bands are located near the Fermi level. Besides, the small hybridization at Fermi level generates the pocket at Γ point. The effective Wannier interpolation reproduces very well the low-energy regime, as we can see from Fig. 22, but the MLWF are not aligned along the cartesian axes, but they show a small tilting following the distortion of the orthorhombic structure. We point out that these conclusions are fully in agreement with the result of [100].

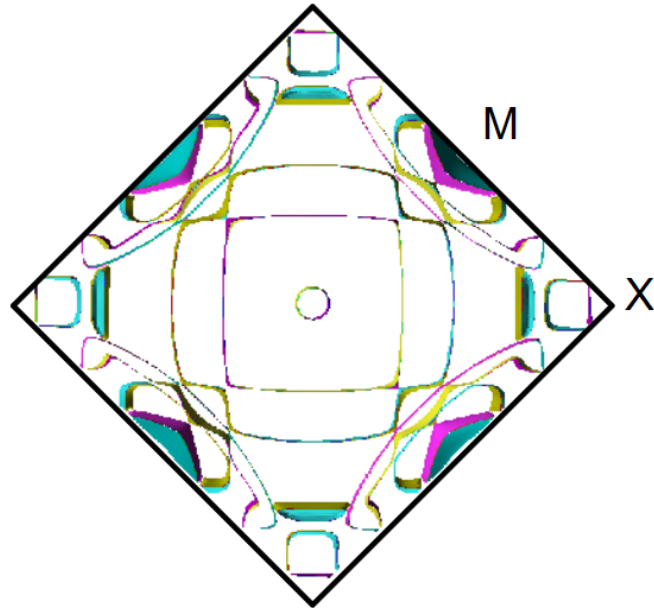


Figure 23: Fermi surface of $\text{Sr}_3\text{Ru}_2\text{O}_7$. The Γ point is at centre of the picture. The *VHS* is in X, along the direction Ru-Ru as in Sr_2RuO_4 .

5.3.3 Sr_2RuO_4 - $\text{Sr}_3\text{Ru}_2\text{O}_7$ hybrid structures

Here, we discuss the structural and electronic properties of heterostructures made by Sr_2RuO_4 and $\text{Sr}_3\text{Ru}_2\text{O}_7$. We will investigate two configurations: the het42 arrangement composed by four Sr_2RuO_4 and two $\text{Sr}_3\text{Ru}_2\text{O}_7$ cells, and het33 one composed by three Sr_2RuO_4 and three $\text{Sr}_3\text{Ru}_2\text{O}_7$ cells.

As first outcome, we have compared the experimental lattice constants of the pure bulk phases with the ones obtained by the full relaxation of the pure phases, het42 and het33 ; the results are reported in Table 4. Let us consider the Sr_2RuO_4 . Although we find a good agreement between our results on pure phases with experimental results, we mention that the in-plane lattice constant a we get is shorter than the available experimental value, whereas the experimental value for the c axis is larger than the value obtained in our calculations. Nevertheless, the computed volume is $\sim 0.7\%$ larger than the experimental one, so we are confident that the discrepancy between experimental lattice constants and theoretical ones will not affect our conclusions. For completeness, we would like to point out that the volume obtained using PBE is $\sim 1\%$ larger than experimental value. [101] When the $\text{Sr}_3\text{Ru}_2\text{O}_7$ is considered, we find out that a lattice constant almost coincides with the experimental value, while the experimental c lattice constant is slightly lower than the numerical value. Also in this case, the theoretical volume is $\sim 0.7\%$ larger than the experimental one. When the het42 and het33 configurations are considered, we find

that for het42 hybrid a lattice constant is comparable with the theoretical value obtained for pure Sr_2RuO_4 , while for het33, where the number of $\text{Sr}_3\text{Ru}_2\text{O}_7$ cells is increased, a gets reduced if compared to the theoretical values obtained for the pure Sr_2RuO_4 and $\text{Sr}_3\text{Ru}_2\text{O}_7$.

Then, we have looked at Δz , the displacement along the c -axis of the Ru atom respect to the planar oxygens, and at the Ru-O-Ru bond angle. The results are summarized in Table 5. From these data we infer two different trends for Δz in Sr_2RuO_4 and $\text{Sr}_3\text{Ru}_2\text{O}_7$. Indeed, as far as Δz for Sr_2RuO_4 is considered, we see that in the bulk of both the hybrid het42 and het33 structures this quantity is zero, i. e. there is no variation of the displacement of Ru-O planar atoms compared to the pure phase. Consequently, no significant variation of the Ru-O-Ru bond angle is appreciated. On the other hand, at the interface a small Δz is produced, Δz being larger for richest Sr_2RuO_4 heterostructure het42. Concerning the $\text{Sr}_3\text{Ru}_2\text{O}_7$, a different behavior is observed: because of the different symmetry a displacement Δz is present also in the bulk. We deduced at the interface as well as in the bulk of both the hybrid structures a change of this Δz . This effect may have important consequences when the ordering of the bare energy levels of $\text{Sr}_3\text{Ru}_2\text{O}_7$ is investigated. We suggest that crystal field is slightly altered by this effect thus producing a rearrangement of the energy ordering of the bare t_{2g} -bands, with potentially relevant physical consequences. Indeed, crystal field effects, associated with the elongation of the RuO_6 octahedra will tend to stabilize ferromagnetic spin configurations. Since the energy of xz and yz orbitals is higher than the energy of xy orbital, and if the Coulomb repulsion is larger than the energy splitting between xz and yz orbitals and yz orbital, to fill these bands, one would occupy first the lower energy band and put the other hole in one of the two degenerate xz and yz bands. In this case there is a gain in the kinetic energy if the holes on the neighbor site have the same spin of the hole moving. This configuration may induce the spins of neighbor sites to be fluctuating in amplitude and in phase, and the net effect may be the appearance of ferromagnetic fluctuations that would be more pronounced for the electrons in the xy band, while the orbital degeneracy for the xz and yz bands would give rise to a kind of frustration in the spin sector reducing the strength of the ferromagnetic correlations.

Furthermore, we argue that this modification of bond angle may modify the hopping parameters, affecting the position of VHS in the $\text{Sr}_3\text{Ru}_2\text{O}_7$ and in the Sr_2RuO_4 making it near the Fermi level. We note that, if suitably located, the VHS may make larger the DOS near the Fermi level at the interface, influencing the electronic response of the hybrid structures. This conjecture has been tested, and in Fig. 24 we have plotted the band structure for the $\text{Sr}_3\text{Ru}_2\text{O}_7$ phases. To better understand the behavior of the VHS, we summarize what we get concerning this singularity in bulk Sr_2RuO_4 and $\text{Sr}_3\text{Ru}_2\text{O}_7$.

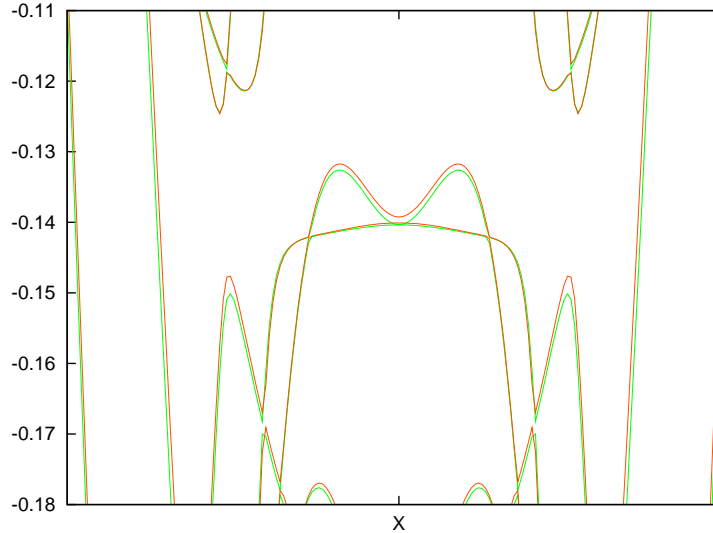


Figure 24: Magnification of the band structure for the $\text{Sr}_3\text{Ru}_2\text{O}_7$ bulk (green line) and $\text{Sr}_3\text{Ru}_2\text{O}_7$ interfaces (red line) for the het33 case. The VHS goes towards the Fermi level because of the different rotation at Fermi level.

Table 4: Comparison of lattice constant between the experimental measurements and the theoretical results. The unit is angstrom.

	Exp. Sr_2RuO_4 [59]	Th. Sr_2RuO_4	Exp. $\text{Sr}_3\text{Ru}_2\text{O}_7$ [99]	Th. $\text{Sr}_3\text{Ru}_2\text{O}_7$	$(\text{Sr}_2\text{RuO}_4)_4(\text{Sr}_3\text{Ru}_2\text{O}_7)_2$	$(\text{Sr}_2\text{RuO}_4)_3(\text{Sr}_3\text{Ru}_2\text{O}_7)_3$
a	3.862	3.887	3.873	3.872	3.881	3.869
c	12.723	12.650	20.796	20.968	46.234	50.554

The theory does not catch the Ru-O-Ru angle in $\text{Sr}_3\text{Ru}_2\text{O}_7$, for this reason the VHS is located 150 meV below the Fermi level (experimentally is 7 meV below the Fermi level), whereas in Sr_2RuO_4 the singularity is 30 meV above the Fermi level (experimentally is 57 meV above the Fermi level). When the interface is concerned, we find that the VHS in both Sr_2RuO_4 and $\text{Sr}_3\text{Ru}_2\text{O}_7$ moves towards the Fermi level. This effect is easily explained considering that in Sr_2RuO_4 there is a displacement along z axis without any rotation of the RuO_6 octahedra that, in turn, produces a reduction of the hopping parameter between xy orbitals. The final effect is that the energy position of the VHS shifts at lower energy. The opposite behavior happens for $\text{Sr}_3\text{Ru}_2\text{O}_7$: in this case the entity of the rotation is less than the previous case so that the energy position of the VHS increases approaching the Fermi level. Also in this case, our assumption is supported by the xy - xy hopping parameter at the interface which is larger than the same parameter in the bulk case.

Now, considering the change of the atomic bonds above discussed, we show in Fig. 25 how Sr_2RuO_4 and $\text{Sr}_3\text{Ru}_2\text{O}_7$ rearrange at the interface, along the c -axis. The figure

Table 5: Measure of the Ru-O-Ru bond angles and displacement of Ru in the several case studied. At the interface, the modification of the Ru-O-Ru bond angle in Sr_2RuO_4 it is due to the Ru displacement along the c -axis, no rotations are found.

	Exp. [59, 99]	Th. Bulk	Bulk het42	Interface het42	Bulk het33	Interface het33
Δz in Sr_2RuO_4	0	0	0	0.008	0	0.007
Δz in $\text{Sr}_3\text{Ru}_2\text{O}_7$	0.017	0.033	0.032	0.039	0.030	0.037
Ru-O-Ru bond angle in Sr_2RuO_4	180.0°	180.0°	180.0°	179.5°	180.0°	179.6°
Ru-O-Ru bond angle in $\text{Sr}_3\text{Ru}_2\text{O}_7$	163.9°	158.1°	158.6°	158.8°	157.4°	157.5°

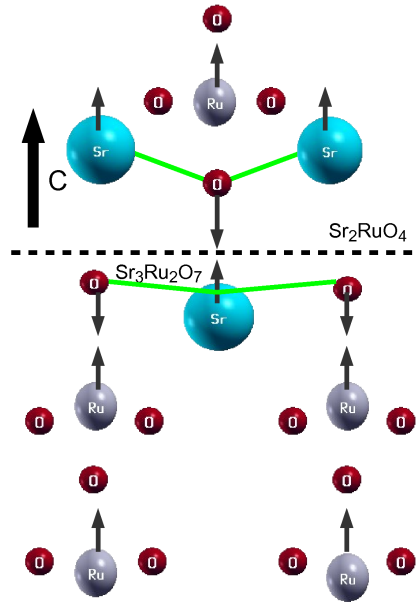


Figure 25: Schematic view of the atomic rearrangement at the interface $\text{Sr}_2\text{RuO}_4/\text{Sr}_3\text{Ru}_2\text{O}_7$. The arrows indicate the most relevant displacements respect to the bulk positions at the interface. The different geometrical configuration of the Sr-O plane is shown (green line). This is more flat for $\text{Sr}_3\text{Ru}_2\text{O}_7$, while there is a greater difference between the Sr and the O atom along the c -axis in Sr_2RuO_4 .

clearly suggests that all the positive charges move in the direction of Sr_2RuO_4 , while the negative ones go in the direction of $\text{Sr}_3\text{Ru}_2\text{O}_7$; the net effect is the emergence of an electric dipole moment. Besides, the creation of a dipole moment in the $\text{Sr}_3\text{Ru}_2\text{O}_7$ phase of the heterostructure, induce a small dipole moment in the first layer of Sr_2RuO_4 . Nevertheless, we point out that this static electric dipole moment is washed out by the itinerancy of conduction electrons that produces a screening of the electrostatic field compensating this effect.

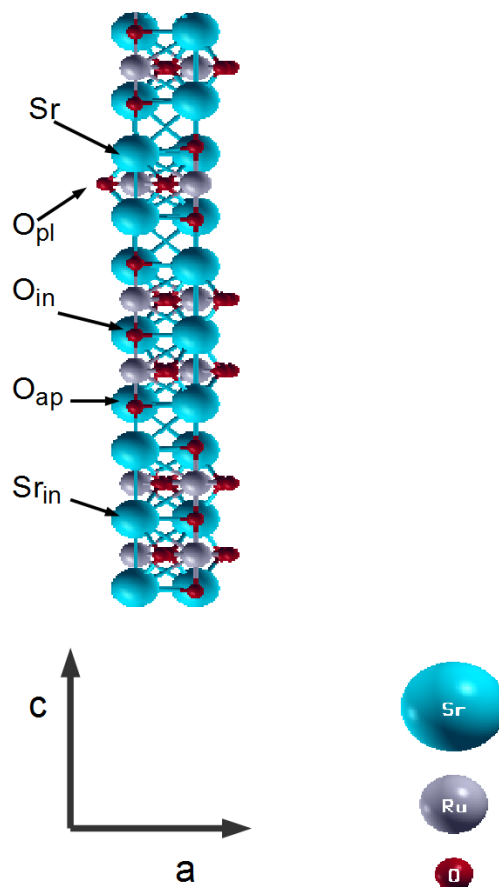


Figure 26: Notation about the atoms. We have three inequivalent oxygen atoms and two inequivalent strontium atoms. We call it: the planar oxygen O_{pl} , the apical oxygen O_{ap} , the intralayer oxygen O_{in} , the intralayer strontium Sr_{in} and the strontium Sr . Sr_{in} and O_{in} are present only in $Sr_3Ru_2O_7$.

Finally, we present all the non-equivalent distances in the heterostructure compared with the bulk properties in Table 6. We have used the notation of Fig. 26 to collect the data of the geometrical rearrangement of the Sr, Ru and O atoms near and far from the interface, for both the heterostructures considered. For comparison, in the same Table we also report the experimental and the theoretical distances for pure phases (the first two columns).

Two bonds are strongly modified at the interface:

1. the distance between the ruthenium and the apical oxygen
2. the distance between the Sr atom and the apical oxygen along the c -axis

Other in plane modifications are smaller. In the first case, the distance becomes greater in Sr_2RuO_4 and smaller in $Sr_3Ru_2O_7$. In the second case, the distance between the Sr_2RuO_4

Table 6: Inequivalent atomic bonds in ruthenates for the several concentrations studied. The main difference between the bulk and the interface are the distances Ru-O_{ap} and Sr-O_{ap} along the *c*-axis.

	Exp. [59, 99]	Th. Bulk	Bulk het42	Interface het42	Bulk het33	Interface het33
Sr-O _{ap} ^{Sr₂RuO₄} along <i>c</i>	2.429	2.433	2.433	2.423	2.431	2.416
Sr-O _{ap} ^{Sr₃Ru₂O₇} along <i>c</i>	2.452	2.449	2.455	2.472	2.447	2.469
Sr-O _{ap} in Sr ₂ RuO ₄ in <i>ab</i>	2.738	2.757	2.757	2.758	2.745	2.747
Sr-O _{ap} in Sr ₃ Ru ₂ O ₇ in <i>ab</i>	2.744	2.743	2.755	2.755	2.739	2.740
Sr-O _{pl} in Sr ₂ RuO ₄	2.688	2.670	2.671	2.673	2.676	2.675
Sr-O _{pl} in Sr ₃ Ru ₂ O ₇	2.506/2.896	2.473/3.002	2.478/2.997	2.480/2.997	2.470/3.015	2.473/3.017
Sr _{in} -O _{in}	2.738	2.738	2.747	2.747	2.737	2.736
Sr _{in} -O _{pl}	2.607/2.986	2.548/3.064	2.556/3.062	2.553/3.055	2.545/3.074	2.543/3.068
Ru-O _{ap} in Sr ₂ RuO ₄	2.062	2.059	2.059	2.069	2.068	2.076
Ru-O _{ap} in Sr ₃ Ru ₂ O ₇	2.038	2.059	2.058	2.050	2.063	2.056
Ru-O _{pl} in Sr ₂ RuO ₄	1.931	1.943	1.943	1.943	1.934	1.934
Ru-O _{pl} in Sr ₃ Ru ₂ O ₇	1.956	1.972	1.977	1.977	1.973	1.972
Ru-O _{in}	2.026	2.045	2.043	2.045	2.049	2.052

oxygen and the Sr₃Ru₂O₇ strontium decreases, while the opposite happens between the Sr₃Ru₂O₇ oxygen and the Sr₂RuO₄ strontium.

5.4 Conclusions

The pure phase Sr₃Ru₂O₇ does not present *e_g* bands at Fermi level, the rotations push the *VHS* below the Fermi level. We performed a full relaxation of the heterostructure Sr₂RuO₄/Sr₃Ru₂O₇ at two different concentrations comparing it with the bulk phases. At both concentrations of the heterostructure, we find a modification of the geometrical position of the atoms. These effects are in the nearest layers at interfaces, while are negligible in the bulk side of the heterostructures. One of the major effects is a displacement of the Ru atoms. This displacement changes the Ru-O-Ru angle in Sr₂RuO₄. Moreover, the rotation of the Sr₃Ru₂O₇ octahedron is slight reduced at interface. These effects strongly modify the position of the *VHS* in both compounds. We find that the *VHS* for both phases go towards the Fermi level.

6 First principles study of KCrF_3

We study the tetragonal-monoclinic structural transition in the compound KCrF_3 . We present the electronic structure and the volume relaxation study for the KCrF_3 in the two different crystalline phases. Following the usual definition of the orbital $|\theta\rangle = \cos\frac{\theta}{2}|3z^2 - 1\rangle + \sin\frac{\theta}{2}|x^2 - y^2\rangle$, the calculation of the e_g orbital gives $\theta = 110.5^\circ$ for the tetragonal structure. For the monoclinic phase, we find $\theta = 120.9^\circ$ and 102.2° for the two types of octahedron. We discuss similarities with KCuF_3 and LaMnO_3 in the orbital.

6.1 Introduction

The discovery of the colossal magnetoresistance effect in doped manganites caused a surge of interest in these perovskite oxides especially due to their potential technological applications. The particular properties of the colossal magnetoresistance materials derive from the intriguing physics of undoped parent compound LaMnO_3 [102]. The presence of strong electronic correlations and an orbital degree of freedom, to which the Jahn-Teller effect is directly related, gives rise to a rich phase diagram in function of the doping displaying an incredible number of spin, charge, orbital and magnetically ordered phases [1]. KCrF_3 is an insulator that exhibits a cooperative Jahn-Teller distortion [103]. It is similar to LaMnO_3 for its structural, electronic and magnetic properties because in the high spin configuration Cr^{2+} is electronically equivalent to Mn^{3+} . Both are tetravalent. At temperatures higher than 973 K, KCrF_3 is cubic, at temperatures between 973 and 250 K it is tetragonal, and finally, at temperatures lower than 250 K it is monoclinic. We report in Table 7 the values of the lattice constant for the tetragonal and monoclinic crystalline structure. In this chapter, we perform ab-initio calculations to describe the structural, electronic and magnetic properties of KCrF_3 . In the following, we present the crystal and the magnetic structures from the experimental data in paragraph 2. In paragraph 3, we expose the computational detail for the ab-initio calculations. In paragraph 4, we show the ab-initio calculations fixing the volume and in paragraph 5 we perform the relaxation of the system in all its structural and magnetic phases.

Table 7: We report crystal structure data for KCrF_3 at different temperatures. This system has bigger volume than KCuF_3 . In this table we report lattice constants a, b and c , the γ angle between the direct vector lattice \mathbf{a} and \mathbf{b} and the temperature at which the measurement is taken. The volume per unit formula is given by $V = \frac{(abc \sin \gamma)}{4}$. The units are angstrom, Kelvin and degree.

Crystalline structure	Parameters					
	$a(\text{\AA})$	$b(\text{\AA})$	$c(\text{\AA})$	T(K)	$\gamma(\text{deg})$	$V(\text{\AA}^3)$
Tetragonal [104]	6.0464	6.0464	8.0230	300	90	73.3300
Tetragonal [105]	6.05230	6.05230	8.02198	room	90	73.4625
Monoclinic [104]	5.8069	5.8137	8.5871	10	93.671	72.3250
Monoclinic [105]	5.82642	5.83517	8.57547	150	93.686	72.7375

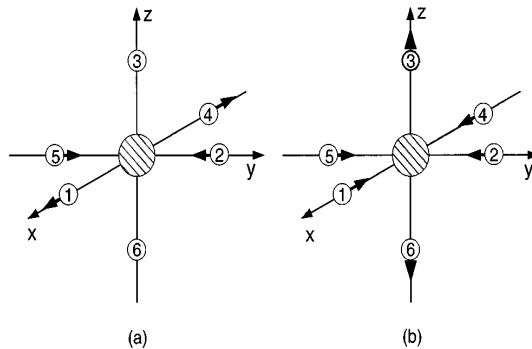


Figure 27: (a) The normal mode Q_2 ($Q_2 > 0$). (b) The normal mode Q_3 ($Q_3 < 0$). Q_2 and Q_3 are given by $Q_2 = \frac{1}{\sqrt{2}}(X_1 - X_4 - Y_2 + Y_5)$ and $Q_3 = \frac{1}{\sqrt{6}}(2Z_3 - 2Z_6 - X_1 + X_4 - Y_2 + Y_5)$ where X, Y , and Z are the coordinates of the surrounding oxygens with the subscript specifying the atoms as shown in the figure.

6.2 Crystal structures and magnetism

The structural changes from the cubic to the tetragonal structure can be described in terms of Q_3 -type tetragonal compression and a Q_2 -type Jahn-Teller distortion, which create a long (l) and a short (s) bond Cr-F in the ab plane (with $l=2.300 \text{ \AA}$ and $s=1.975 \text{ \AA}$ at 300 K [104]) as we can see in Fig. 27. These are the only distortions in the tetragonal phase and are analogue to the LaMnO_3 distortion [106]. The tetragonal structure is always paramagnetic. At $T = 0$, the hypothetical tetragonal structure would be antiferromagnetic with A-type order like in Fig. 28. Below 250 K, KCrF_3 exhibits a phase transition to a monoclinic structure, characterized by a pronounced tilting of the CrF_6 octahedra. In the monoclinic phase, the structure is drastically different from the tetragonal one: sites 1 and sites 2 became inequivalent (Fig. 29) and all the distances Cr-F are inequivalent,

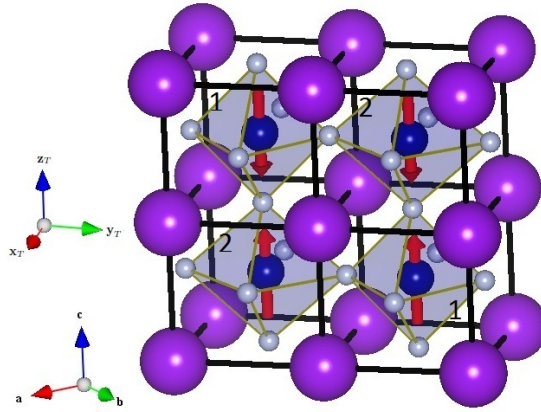


Figure 28: Antiferromagnetic *A*-type tetragonal crystal structure. Cr is in the centre of *F* octahedra enclosed in a *K* cage. All Cr are equivalent, site 1 and 2 are related by relation $x \longleftrightarrow y$. For this reason we call it type-1 octahedron and type-2 octahedron. The pseudocubic axes are defined as $\mathbf{x}_T = (\mathbf{a}_T + \mathbf{b}_T)/2$, $\mathbf{y}_T = (-\mathbf{a}_T + \mathbf{b}_T)/2$ and $\mathbf{z}_T = \mathbf{c}_T/2$. The pseudocubic axes connect first-neighbour Cr. For the type-1 octahedron the long (short) bond is along \mathbf{x}_T (\mathbf{y}_T) direction. The red arrows represent the spins. KCrF_3 is tetragonal between 250 and 973 K.

as we can see in Table 8. The octahedra CrF_6 are rotated in the *ab* plane, and the distance Cr-F along the *c*-axis (or \mathbf{x}_M axis) is different between the two octahedra. The K atoms are not in the high symmetry position as in the tetragonal case, but are displaced along the *c*-axis by 0.026 Å. We define different pseudocubic axis basis to compare the tetragonal and monoclinic structure. The monoclinic structure shows alternating short and long bonds occurring in the plane defined by \mathbf{x}_M and \mathbf{y}_M . The direction of \mathbf{x}_M is the direction of the spins in the magnetic phase (below 79.5 K). In the tetragonal case the modules of the pseudocubic axis are $|\mathbf{x}_T| = |\mathbf{y}_T| > |\mathbf{z}_T|$, and in the monoclinic case they are $|\mathbf{x}_M| \cong |\mathbf{y}_M| > |\mathbf{z}_M|$. With decreasing temperature, four magnetic phase transitions are observed at 79.5, 45.8, 9.5, and 3.2 K. Below $T_N=79.5$ K, the Cr^{2+} moment orders in an incommensurate antiferromagnetic arrangement, which can be defined by the magnetic propagation vector $(1/2 \pm \delta, 1/2 \pm \delta, 0)$. The incommensurate-commensurate magnetic transition occurs at 45.8 K and the magnetic propagation vector locks into $(1/2, 1/2, 0)$ with the Cr moment of $3.34 \mu_B$. The two transitions below 10 K are due to the spin-orbit coupling effect [104]. We will use the experimental atomic positions of the article [104] in the next sections. The measurements are taken at $T=300$ K for the tetragonal case and $T=10$ K for the monoclinic case.

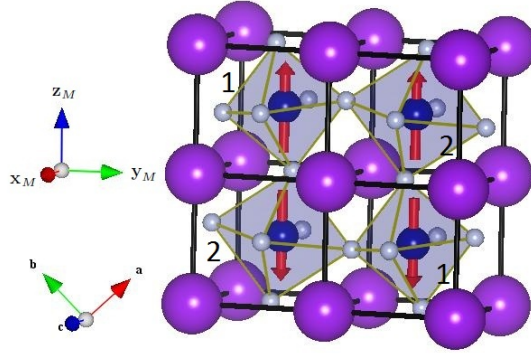


Figure 29: Antiferromagnetic *A*-type monoclinic crystal structure. Cr is in the centre of *F* octahedra enclosed in a *K* cage. Cr in the octahedron 1 is not equivalent to Cr in the octahedron 2. The pseudocubic axes are defined as $\mathbf{x}_M = \mathbf{c}_M/2$, $\mathbf{y}_M = (\mathbf{a}_M - \mathbf{b}_M)/2$ and $\mathbf{z}_M = (\mathbf{a}_M + \mathbf{b}_M)/2$. For the octahedron 1 the long (short) bond is along \mathbf{x}_M (\mathbf{y}_M) direction. The red arrows represent the spins, the direction of the spin-axis should be along the \mathbf{x}_M vector but we plot it in this way for better visualization. KCrF_3 is monoclinic below 250 K.

Table 8: We report the distance Cr-F (d^{lmn}) and the volume of the octahedra V_{oct} for each type [104]. The unit is angstrom. l, m and n are the coefficient of the connecting vector $\mathbf{T} = l\mathbf{x}_T + m\mathbf{y}_T + n\mathbf{z}_T$ for the tetragonal case or $\mathbf{T} \sim l\mathbf{x}_M + m\mathbf{y}_M + n\mathbf{z}_M$ for the monoclinic phase. The direction of these vectors is the direction of the Cr-Cr bond. This direction coincides with the Cr-F direction in the tetragonal phase, but it is approximately coincident in the monoclinic phase because of the tilt.

	$d^{100}(\text{\AA})$	$d^{010}(\text{\AA})$	$d^{001}(\text{\AA})$	$V_{oct}(\text{\AA}^3)$
Tetr. type-1 octahedron	2.300	1.975	2.006	12.151
Tetr. type-2 octahedron	1.975	2.300	2.006	12.151
Monoc. type-1 octahedron	2.319	2.000	1.975	12.218
Monoc. type-2 octahedron	1.975	2.278	2.046	12.271

6.3 Computational details: *DFT*, *PAW* and *LSDA + U*

We perform unpolarized and spin-polarized first-principles *DFT* calculations [6] using the *GGA* exchange-correlation functional of Perdew, Burke, and Ernzerhof [97]. Moreover, we use *LSDA* and *LSDA + U* [107, 108] approach for the volume relaxation technique. There are many extensions and simplifications of *LSDA + U*, but we use the rotational invariant approach proposed by Liechtenstein [109] implemented in the Vienna ab-initio simulation package (*VASP*) [10]. We use a plane-wave energy cut-off of 600 eV to avoid

Pulay stress and a k-point grid of $8 \times 8 \times 6$ for the relaxation of magnetic supercells with 20 atoms. We fix the volume and optimize the internal degree of freedom by minimizing the total energy are less than $5 * 10^{-3}$ eV and the remaining forces are less than $9 * 10^{-3}$ eV/Å. We scan the volume to calculate the energy vs. volume curve.

Calculations of hopping parameters are made with *PAW* code *ABINIT* [110, 60, 111] computing the overlap operator for Wannier90 [11] interface using a $8 \times 8 \times 8$ k-point grid centered on the Γ point.

In all calculations, we find that the band structure obtained using *VASP* match very well to the *ABINIT* band structure. In Fig. 30 and 31 we show the band structure for the non magnetic case. We can see that they match very well near the Fermi level but the *VASP* bandwidth is 3-4% larger than the *ABINIT* bandwidth when we are far from the Fermi level. The bandwidth of t_{2g} is around 1.0 eV, the bandwidth of t_{2g} is around 2.2-2.3 eV and the total bandwidth for d electron is around 3.0 eV. Small difference can be observed between the monoclinic and the tetragonal phase. In both approaches, we have that the total bandwidth W_d and the bandwidth of the e_g W_{e_g} became smaller in the monoclinic case. Instead, the bandwidth $W_{t_{2g}}$ becomes bigger in the monoclinic case.

Using *ABINIT*, we find that the bandwidths of the tetragonal phase are $W_d \approx 2.96$, $W_{t_{2g}} \approx 0.99$ and $W_{e_g} \approx 2.28$ while the bandwidths of the monoclinic phase are $W_d \approx 2.86$, $W_{t_{2g}} \approx 1.03$ and $W_{e_g} \approx 2.22$. Using *VASP*, we have that the bandwidths of the tetragonal phase are $W_d \approx 3.00$, $W_{t_{2g}} \approx 0.98$ and $W_{e_g} \approx 2.27$, while, the bandwidths of the monoclinic phase are $W_d \approx 2.92$, $W_{t_{2g}} \approx 1.07$ and $W_{e_g} \approx 2.24$.

Since the γ angle is slightly different by 90° and because the lattice constants $a \approx b$, the two Brillouin zones for the tetragonal and monoclinic phase are not so different. We choose k-point path in the band structures similar for the two phases.

6.4 Ground state, orbital order and magnetic properties

We use the pseudocubic axis as reference system to compare the properties of the two phases. We use the notation of the article [112]

$$|\theta\rangle = \cos\frac{\theta}{2}|3z^2 - 1\rangle + \sin\frac{\theta}{2}|x^2 - y^2\rangle \quad (84)$$

to calculate the orbital. After performing self-consistent calculations within *LSDA + U* approach, we use the occupation matrix to obtain orbital parameters using (84). The

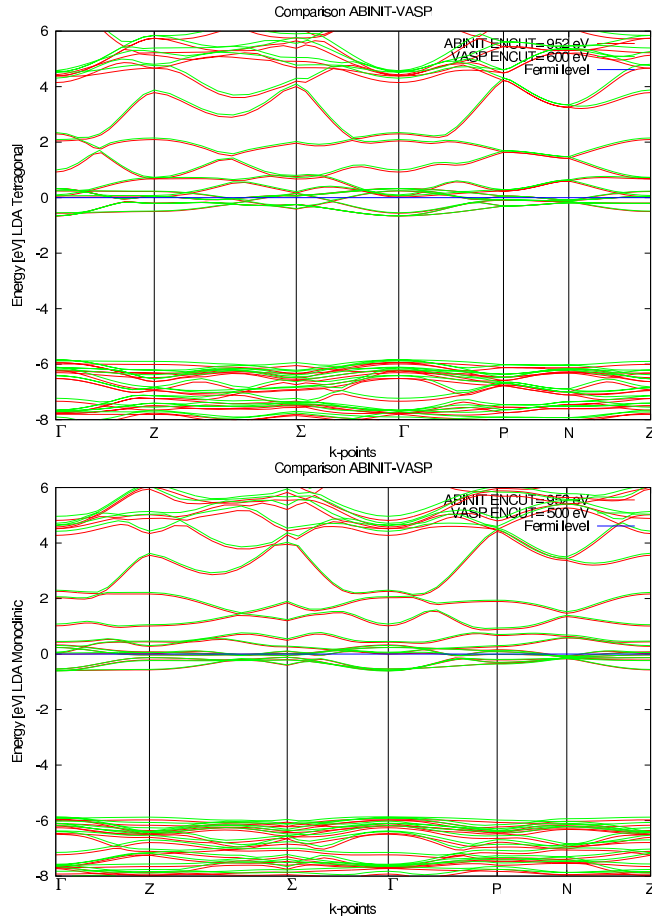


Figure 30: Comparison between *VASP* band structure (green) and *ABINIT* band structure (red) in the tetragonal (up) and monoclinic (down) phase in *LDA* calculations near the Fermi level. The Fermi level is set at zero.

occupation matrix calculated by *VASP* on the basis of the real atomic basis set is the following for *LSDA + U* in the monoclinic phase:

$$n_{occ}^{\uparrow} = \begin{pmatrix} 0.9142 & 0.0000 & 0.0024 & 0.0000 & -0.2380 \\ 0.0000 & 0.9599 & 0.0000 & -0.0002 & 0.0000 \\ 0.0024 & 0.0000 & 0.9654 & 0.0000 & 0.0084 \\ 0.0000 & -0.0002 & 0.0000 & 0.9599 & 0.0000 \\ -0.2380 & 0.0000 & 0.0084 & 0.0000 & 0.2111 \end{pmatrix} \quad (85)$$

$$n_{occ}^{\downarrow} = \begin{pmatrix} 0.0301 & 0.0000 & 0.0003 & 0.0000 & 0.0238 \\ 0.0000 & 0.0136 & 0.0000 & -0.0002 & 0.0000 \\ 0.0003 & 0.0000 & 0.0375 & 0.0000 & 0.0003 \\ 0.0000 & -0.0002 & 0.0000 & 0.0133 & 0.0000 \\ 0.0238 & 0.0000 & 0.0003 & 0.0000 & 0.1037 \end{pmatrix} \quad (86)$$

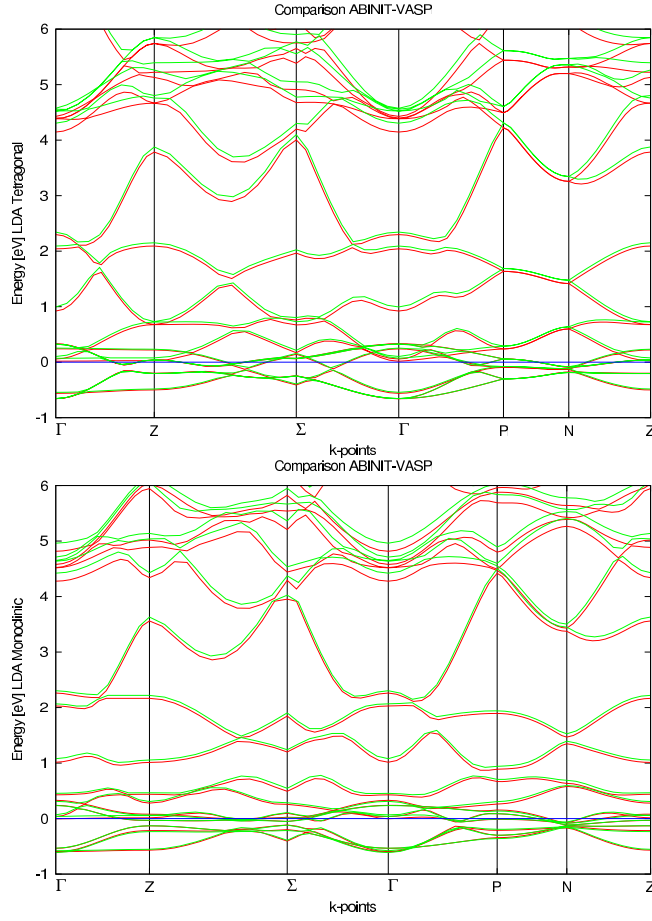


Figure 31: Comparison between *VASP* band structure (green) and *ABINIT* band structure (red) in the tetragonal (up) and monoclinic (down) phase in *LDA* calculations near the Fermi level. The *VASP* bandwidth is 3-4% bigger. The Fermi level is set at zero.

Diagonalizing (85) and (86), we get:

$$n_{occ}^{\uparrow} = \begin{pmatrix} 0.99 & 0 & 0 & 0 & 0 \\ 0 & 0.97 & 0 & 0 & 0 \\ 0 & 0 & 0.96 & 0 & 0 \\ 0 & 0 & 0 & 0.96 & 0 \\ 0 & 0 & 0 & 0 & 0.14 \end{pmatrix} \quad (87)$$

$$n_{occ}^{\downarrow} = \begin{pmatrix} 0.11 & 0 & 0 & 0 & 0 \\ 0 & 0.04 & 0 & 0 & 0 \\ 0 & 0 & 0.02 & 0 & 0 \\ 0 & 0 & 0 & 0.01 & 0 \\ 0 & 0 & 0 & 0 & 0.01 \end{pmatrix} \quad (88)$$

and we can approximate the matrix (87) to

$$n_{occ}^\dagger \simeq \begin{pmatrix} 1 & 0 & 0 & 0 & 0 \\ 0 & 1 & 0 & 0 & 0 \\ 0 & 0 & 1 & 0 & 0 \\ 0 & 0 & 0 & 1 & 0 \\ 0 & 0 & 0 & 0 & 0 \end{pmatrix} \quad (89)$$

We have four eigenvectors with eigenvalues near 1 (occupied state). The eigenvectors of n_{occ}^\dagger in terms of the basis $(d_{xy} \ d_{xz} \ d_{yz} \ d_{3z^2-1} \ d_{x^2-y^2})$ are (in the same order of approximation) :

$$\begin{pmatrix} 1 & 0 & 0 & 0 & 0 \\ 0 & 1 & 0 & 0 & 0 \\ 0 & 0 & 1 & 0 & 0 \\ 0 & 0 & 0 & a_1 & a_2 \\ 0 & 0 & 0 & a_3 & a_4 \end{pmatrix} \quad (90)$$

We can see that three occupied states are t_{2g} and one occupied state is e_g . We use the projections of the eigenvector of the e_g state on real atomic orbitals to reconstruct the θ angle

$$\tan \frac{\theta}{2} = \frac{\sin \frac{\theta}{2}}{\cos \frac{\theta}{2}} = \frac{\text{projection on } dx^2 - y^2}{\text{projection on } dz^2 - 3r^2} = \frac{a_2}{a_1} \quad (91)$$

We calculate the θ angle for the two experimental structures [104] in the A -type antiferromagnetic configuration along the z -axis for the tetragonal phase and the experimental antiferromagnetic structure. We have $\theta = -110.5^\circ$ and $\theta = +110.5^\circ$ for the tetragonal structure respectively for type-1 and type-2 octahedron, that is very similar to the value of the LaMnO_3 . The two values of the theta angle must be opposite in all the systems where the sites are equivalent, but, the direction of one orbital is rotate of 90 degrees with respect to the other orbital. For the monoclinic phase, as we have two inequivalent Cr, we have two different values for the two octahedra. We find $\theta = -120.9^\circ$ and $+102.2^\circ$, respectively for the first and the second octahedron. We can observe that the monoclinic type-1 octahedron is extremely elongated in the \mathbf{x}_M -direction ($l=2.319 \text{ \AA}$). This would be correlated to the orbital because we have $\theta \simeq -120^\circ$ for the type-1 octahedron ($|-120^\circ \rangle = -|3x^2 - 1\rangle$).

We study the antiferromagnetic A -type configuration in the tetragonal and monoclinic structure. We find a magnetic moment of $3.65 \mu_B$ ($3.87 \mu_B$) in $LSDA$ ($LSDA + U$). For the monoclinic phase, we find a magnetic moment of 3.636 and $3.653 \mu_B$ (3.867 and $3.874 \mu_B$) in $LSDA$ ($LSDA + U$) respectively for the first and the second octahedron. So, all the Cr^{2+} ions are in the high spin $t_{2g}^3 e_g^1$ state, in accordance with Hund's rule.

The biggest difference between LaMnO_3 and KCrF_3 is the orbital order. While in LaMnO_3

and KCuF_3 , the order is C-type in according with the Goodenough-Kanamori-Anderson rules, in KCrF_3 the order is G-type. The G-type order is predicted for the hypothetical ferromagnetic phase of LaMnO_3 [139].

6.5 Volume relax

We perform the relaxation of the volume of KCrF_3 in *LDA*, *LSDA* and *LSDA + U* (only *AFM A*-type solution) for all crystal phases using a conjugate-gradient algorithm. All the data shown in this paragraph are obtained from *VASP* but some tests have been done with *ABINIT* using the same technique. The two results obtained are in agreement. We can observe two general results: 1) The non magnetic solutions (*LDA*) are very high in energy respect to the magnetic solution how we can see from Fig. 32. 2) The equilibrium volume of the monoclinic case is always smaller than the tetragonal case. Moreover, the ground state is cubic in *LDA*, monoclinic in *LSDA* and monoclinic in *LSDA + U*.

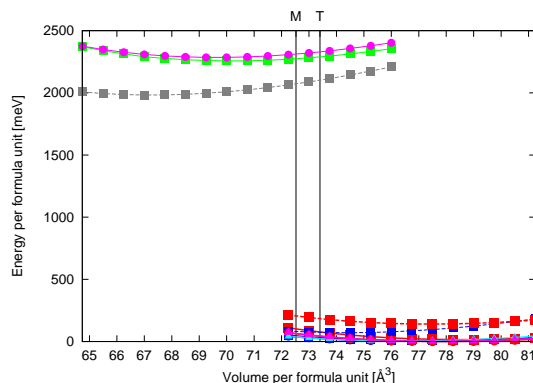


Figure 32: Energy vs. volume curves for the magnetic and non magnetic case. The ground state is shifted at zero energy level. The label *T* and *M*, on the x-axis, are experimental volume respectively of the tetragonal and monoclinic structure. The non magnetic solutions are in the top on the left side and the magnetic solutions are in the bottom on the right side.

6.5.1 *LDA*

In the *LDA* case all the solutions are metallic. We perform the relaxation the system fixing the volume shape and the internal degree of freedom, if we do not fix it we obtain that the tetragonal volume (or the monoclinic volume) becomes cubic because the cubic symmetry is lower in energy. The low symmetry phase (tetragonal o monoclinic) can

converge to the high symmetry phase (cubic) but the opposite is forbidden. The ground state is the cubic structure (Fig. 33) but the equilibrium volume is not so accurate. The experimental volume of the cubic structure is 75.78 \AA^3 [103]. We can see that, at the experimental volume, the tetragonal phase is energetically favored in comparison to the monoclinic phase contrarily to the magnetic case. These non-magnetic solutions are 2 eV higher than the magnetic solutions, therefore energetically unstable. *DFT* theory is a zero temperature theory and can not accurately reproduce transitions at high temperature, but the message is that tetragonal and monoclinic phases are very close in energy. Moreover, the equilibrium volume of the monoclinic phase is always smaller than the tetragonal phase in agreement with the experimental results in Table 7.

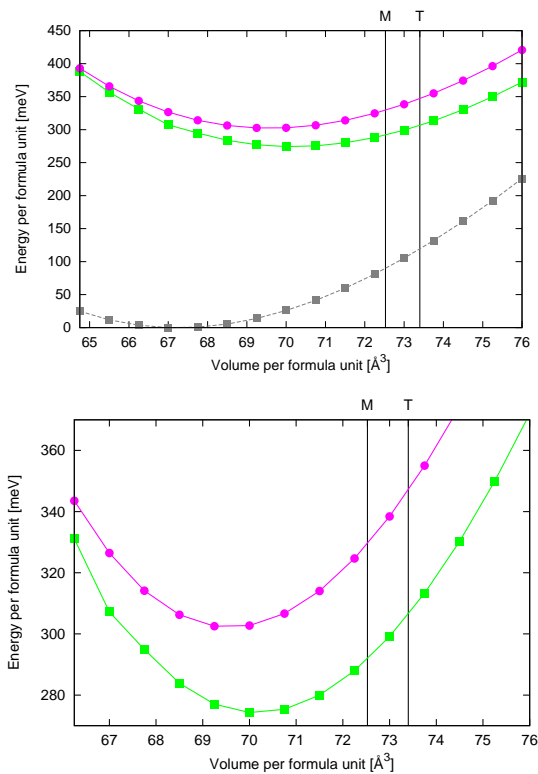


Figure 33: Energy vs. volume curves for the non magnetic case (above panel) and magnification (below panel). The ground state is shifted at zero energy level. The labels T and M , on the x-axis, are the experimental volume respectively of the tetragonal and monoclinic structure. The square dots represent the curve of the tetragonal phase (green), the circles represent the monoclinic phase (pink) and the square dots with dashed lines represent the cubic phase (grey).

6.5.2 *LSDA* and *LSDA + U*

All the solutions are insulating except for the cubic *LSDA*, that is metallic. In the magnetic case, we find an equilibrium volume larger than the experimental one. The energy difference are bigger for the *LSDA + U* case. For the monoclinic magnetic phase, we perform the relaxation of the system in two ways: preserving the shape volume and allowing the system to change shape volume. We can see from Fig. 34 that the monoclinic solution with fixed shape (blue curve and triangle dot) and the variable shape (blue curve and circle dot) are different, so, *LDA* can not describe accurately the shape of the monoclinic system. Instead, *LSDA + U* can describe the shape of the monoclinic phase very well. The ground state is the monoclinic structure in *LSDA* and *LSDA + U*, but the energy difference between two phases is very small (10 meV in *LSDA* and 20 meV in *LSDA + U* per formula unit) as we can see in Fig. 34.

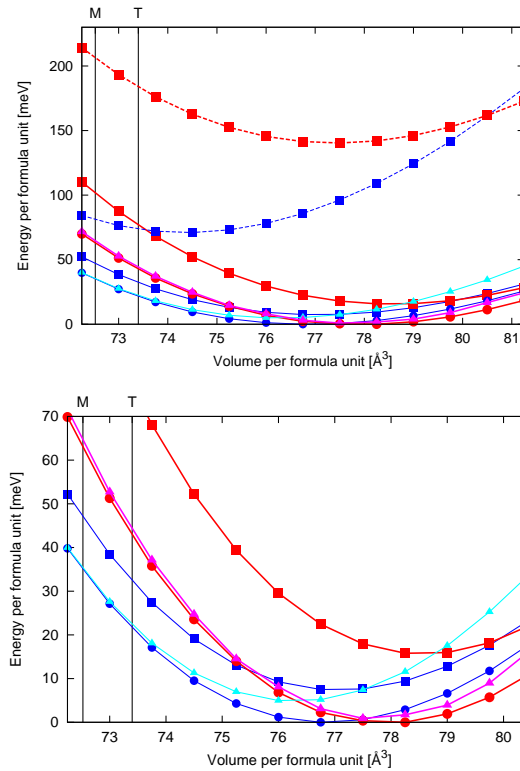


Figure 34: Energy vs. volume curves for the antiferromagnetic case (above panel) and his magnification (below panel). The blue curves are *LSDA* calculations and the red curves are *LSDA + U*. The ground state in *LSDA* and *LSDA + U* are shifted at zero energy level. The labels *T* and *M*, on the x-axis, are the experimental volume respectively of the tetragonal and monoclinic structure. The square dots represent the curve of the tetragonal phase, the triangles represent the monoclinic phase with fixed shape and the circles the monoclinic phase with variable shape. The dashed lines with square dots are the solutions with cubic cell.

6.5.3 High volume

In the non magnetic case, we can see from Fig. 33 that the energy difference increases at a higher volume compared to the equilibrium volume. The equilibrium volume for the monoclinic phase is smaller than the equilibrium volume for the tetragonal phase. We check that a similar behaviour takes place in the magnetic case, when the volume per formula unit is 85 \AA^3 and the tetragonal phase gives the ground state in *LSDA*. At 85 \AA^3 , in *LSDA + U* the ground state is again the monoclinic but the difference in energy between the two structures is smaller. 85 \AA^3 is a huge volume (+16% in comparison to the experimental one), but it tells us that the tetragonal structure is favored at high volume, also in the magnetic case. Based on the experimental data, the tetragonal phase is present at high temperature when the volume of the system is greater in comparison to the volume of the monoclinic phase.

6.5.4 The hypothetical ferromagnetic phase

In the paper [113] using ultrasoft pseudopotential plane wave method, they found that the ferromagnetic phase of KCrF_3 is the ground state for the cubic structure in *LSDA*. We find that the cubic half-metallic ferromagnetic phase is 20 meV lower than all the antiferromagnetic *LSDA* energies, but the problem is solved in *LSDA + U*, where the ferromagnetic phase is 500 meV higher than the antiferromagnetic phases. This problem is due to an overestimation of the kinetic energy in *LSDA*.

In the tetragonal and monoclinic structures, the hypothetical ferromagnetic phase of KCrF_3 is insulating. This is a large difference with LaMnO_3 , where the hypothetical ferromagnetic phase is half-metallic and it is found experimentally doping the system. We can speculate that doping the KCrF_3 compound will be more difficult to reproduce the half-metallic ferromagnetic phase respect to the LaMnO_3 .

6.6 Conclusions

Performing density functional calculations, we have determined the electronic, magnetic, orbital and volume properties of KCrF_3 . We found that KCrF_3 is a strongly correlated antiferromagnetic insulator with the monoclinic structures as ground state. The tetragonal symmetry shows many similarities with LaMnO_3 from the electronic, magnetic and orbital

point of view. But, the monoclinic symmetry has two different Cr sites with two different orbitals: one is KCuF_3 -like and the other is more similar to LaMnO_3 orbital order. The orbital order in the KCrF_3 compound is G-type in the non-cubic phases. The equilibrium volume for the monoclinic phase is smaller than the equilibrium volume for the tetragonal phase in agreement with experimental data.

7 Calculation of model Hamiltonian parameters for KCrF_3

We present and compare the hopping parameters for the cubic, tetragonal and monoclinic structures of KCrF_3 using the e_g basis and the Maximally localised Wannier functions. Moreover, we analyse the strength of electronic correlation using the Cococcioni method based on linear response approach. Although, the atomic number of chromium is relatively small, it is observed experimentally that the spin-orbit effect can play a non trivial role at low temperature. We go beyond the spin collinear approximation, the spin-orbit coupling and the weak ferromagnetism are also examined.

7.1 Introduction

The formalism of the Maximally localised Wannier functions (*MLWF*) has been applied in many and diverse fields. Linear scaling quantum Montecarlo, photonic crystal and metal-insulator interfaces are some relevant example. Furthermore, it is efficient interpolator for the anomalous Hall effect and elcetron-phonon coupling, and a powerful tool for the study of large scale systems. In addition, *MLWFs* are playing an increasing role in bridging density-functional approaches and strongly correlated ones, to derive model Hamiltonian or as a starting point for *LDA + U*, *LDA + DMFT* or *LDA + CDMFT* [11]. Here, we deepen the study of KCrF_3 , started in previous chapter, studying the low-energy physics and the non-collinear properties of its ground state.

We find that KCrF_3 , like LaMnO_3 , in the antiferromagnetic *A*-type configuration is an insulator for both phases in *LSDA* approach. We calculate hopping parameters in the *LDA* non magnetic case in two ways: first using the e_g basis and second using the Maximally-Localized Wannier Functions basis. In the pictures of the Wannier functions we only show just the short bond Cr-F, not the long bond. All the plots of Wannier functions are made using *xcrysden* [114]. In Fig. 35, 36 and 37 we show, respectively, the interpolated band structure for the cubic, tetragonal and monoclinic phases. We have 3d bands of Cr at Fermi level, but at 1 eV above the Fermi level there is a 4s Cr band as we can see clearly in Fig. 35. Fortunately, the 4s Cr band does not go below the Fermi level. The strongly believe that the unusual 4s band near the Fermi level, comes from the presence fluorine that force the configuration Cr^{2+} . Indeed, due to its low ionization, potential divalent chromium is rarely found in solid state physics. In the cubic case, we can observe the twofold degenerate e_g level and the threefold degenerate t_{2g} level at Γ point due to the absence of the tetragonal crystal field. We can also see the 4s Cr band that is below the e_g at Γ point and does not hybridize with the e_g because all are eigenstates of the

Hamiltonian with different symmetry. When we analyse the tetragonal and monoclinic phases, the eigenstates of the Hamiltonian are not e_g , t_{2g} , $4s$... but a mix of all these states. The result is that the band that has a strong $4s$ character hybridizes with the bands of e_g character. We use frozen windows in the calculation of hopping parameters, in this way we impose the perfect interpolation of the band structure, so these hopping parameters for the 3d bands contain the hybridization with the 4s band. In the other case, the interpolations are not perfect at Γ point, due to the hybridization with the 4s band that is impossible to eliminate with our technique. We call $|j, i, T\rangle$ ($|j, i, M\rangle$) the state of the orbital j ($j = x^2 - y^2, 3z^2 - 1$) on the site i of the tetragonal (monoclinic) structure.

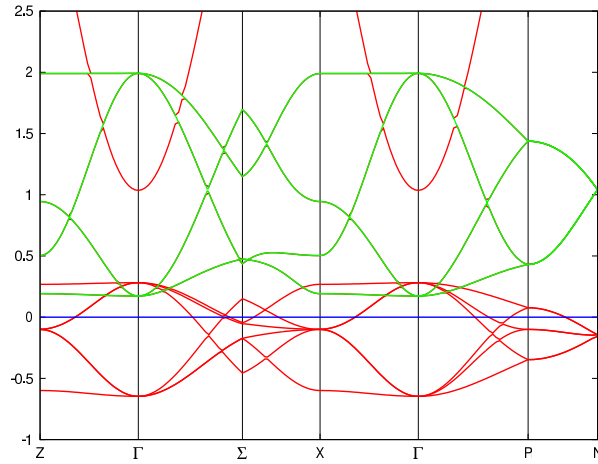


Figure 35: *LDA* band structure (red) and e_g bands obtained using the *MLWFs* (green) for the cubic case. The Fermi level is set at zero. The level of e_g bands in the cubic band structure is higher in energy respect to the other phases.

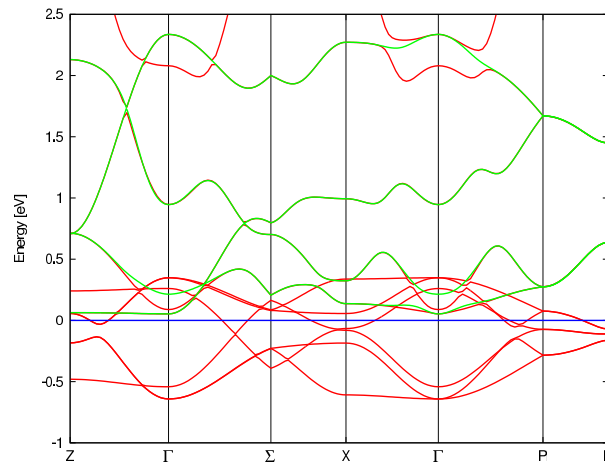


Figure 36: *LDA* band structure (red) and e_g bands obtained using the *MLWFs* (green) for the tetragonal case. The Fermi level is set at zero.

The remainder of this chapter is organised as follows. In paragraph 2 and 3, we calculate ab-initio the hopping parameters using respectively the e_g basis and the *MLWF* basis. We evaluate the Coulomb repulsion using the Cococcioni method in paragraph 4. In

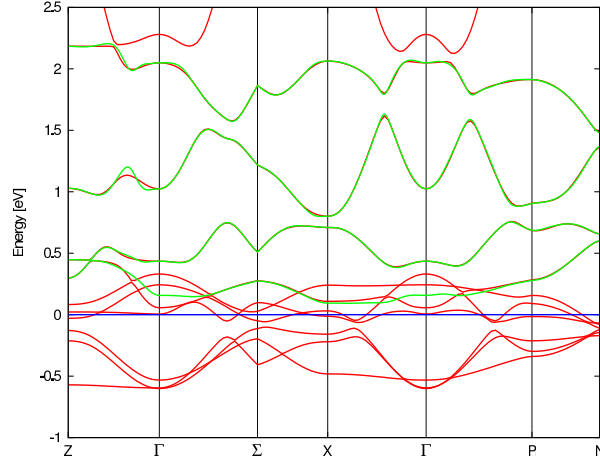


Figure 37: *LDA* band structure (red) and e_g bands obtained using the *MLWFs* (green) for the monoclinic case. The Fermi level is set at zero.

paragraph 5, we calculate magnetocrystalline anisotropy effect to estimate the strengthen of the spin-orbit coupling.

7.2 e_g basis

We use the e_g basis as trial functions $|g(\mathbf{r})\rangle$; these trial functions are projected onto the cell-periodic part of the N Bloch eigenstates $|u_{m\mathbf{k}}(\mathbf{r})\rangle$ calculated using the *DFT* technique. We have four e_g trial functions (two functions for each of the two sites). N is the number of Bloch states in the energy window.

$$|\phi_{n\mathbf{k}}(\mathbf{r})\rangle = \sum_{m=1}^N \langle u_{m\mathbf{k}}(\mathbf{r}) | g_n(\mathbf{r}) \rangle |u_{m\mathbf{k}}(\mathbf{r})\rangle \quad n = 1, 2, 3, 4 \quad (92)$$

Orthonormalising the resulting four functions $|\phi_{n\mathbf{k}}(\mathbf{r})\rangle$ via a Löwdin transformation we find

$$|\phi_{n\mathbf{k}}^{ON}\rangle = \sum_{m=1}^4 (S^{-1/2})_{mn} |\phi_{m\mathbf{k}}\rangle \quad n = 1, 2, 3, 4 \quad (93)$$

where $S_{mn} = \langle \phi_{m\mathbf{k}} | \phi_{n\mathbf{k}} \rangle$ is the overlap matrix. The resulting $|\phi_{n\mathbf{k}}^{ON}\rangle$ are used for the disentanglement procedure and the result is integrated into the \mathbf{k} -space to obtain the Wannier functions $|\omega_{n\mathbf{R}}^{e_g}\rangle$. We use $|\omega_{n\mathbf{R}}^{e_g}\rangle$ as a basis to calculate hopping parameters for the tetragonal phase and the monoclinic phase. We can observe in Fig. 38, 39 and 40 that $|\omega_{n\mathbf{R}}^{e_g}\rangle$ are almost equal to e_g basis.

7.2.1 Tetragonal phase

We show the basis of the tetragonal case in Fig. 38 for the type-1 octahedron. Since the Cr sites are equivalent, the other elements of the basis for the type-2 octahedron have the same shape, but rotated by 90° . We present the hopping parameters in Table 9 using this basis. We use notation of the Table 9 for the hopping parameter. Moreover, we add

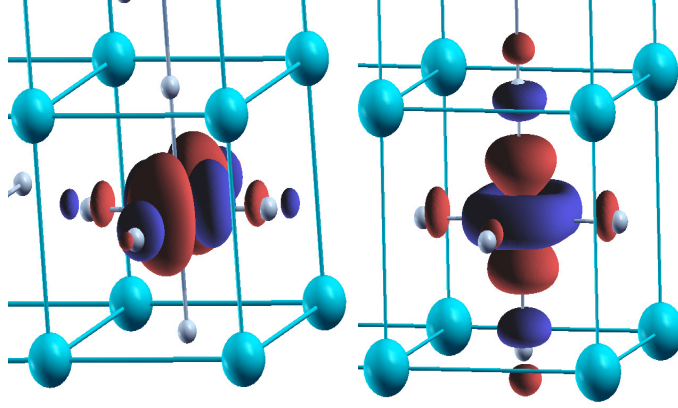


Figure 38: $|\omega_{n\mathbf{R}}^{eg}\rangle$ for the tetragonal case for the site 1 used as basis to calculate hopping parameters. We have two orbitals on the site 1; we call $|x^2 - y^2, 1, T\rangle$ the state similar to $|x^2 - y^2\rangle$ (left panel) and $|3z^2 - 1, 1, T\rangle$ the state similar to $|3z^2 - 1\rangle$ (right panel). The Cr sites are equivalent but the two octahedra have different orientation, so the total number of elements of the basis is 4. We call $|x^2 - y^2, 2, T\rangle$ and $|3z^2 - 1, 2, T\rangle$ the states that are on the site 2.

Table 9: The basis is composed by $|x^2 - y^2, 1, T\rangle$, $|x^2 - y^2, 2, T\rangle$, $|3z^2 - 1, 1, T\rangle$ and $|3z^2 - 1, 2, T\rangle$. Hopping integrals $t_{j,j'}^{i,i'}$ from a site i with orbital j to neighboring site i' with orbital j' for the tetragonal structure. The orbital 1 is $|x^2 - y^2\rangle$, the orbital 2 is $|3z^2 - 1\rangle$. The connecting vector is $\mathbf{T} = l\mathbf{x}_T + m\mathbf{y}_T + n\mathbf{z}_T$; the hopping integrals are tabulated up to the first neighbors. ϵ_j^i is the energy on site for the orbital j on the site i . All energies are in eV.

lmn	$t_{1,1}^{1,2}$	$t_{1,2}^{1,2}$	$t_{2,1}^{1,2}$	$t_{2,2}^{1,2}$
100	-0.1712	0.1566	0.1089	-0.0952
010	-0.1712	-0.1089	-0.1566	-0.0952
001	0.0465	-0.0729	0.0729	-0.2921

lmn	$\epsilon_1^1 = \epsilon_1^2$	$\epsilon_2^1 = \epsilon_2^2$	$t_{1,2}^{1,1}$	$t_{1,2}^{2,2}$
000	0.7915	1.1018	0.3900	-0.3900

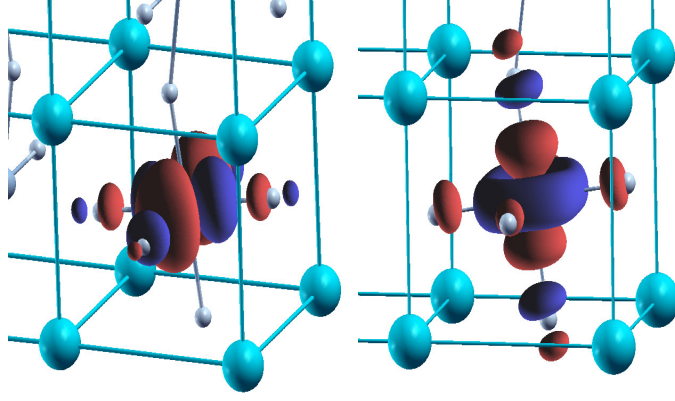


Figure 39: $|\omega_{n\mathbf{R}}^{e_g}\rangle$ for the monoclinic case for the site 1 used as basis to calculate hopping parameters. We have two orbitals on the site 1; we call $|x^2 - y^2, 1, M\rangle$ the state similar to $|x^2 - y^2\rangle$ (left panel) and $|3z^2 - 1, 1, M\rangle$ the state similar to $|3z^2 - 1\rangle$ (right panel).

the coefficient lmn of the direction of the connecting vector to make the notation $t_{j,j'}^{lmn,i,i'}$ for the hopping parameters. We can observe in Table 9 that hopping $t_{1,1}^{100^{1,2}} = t_{1,1}^{010^{1,2}} = -0.1712$, $t_{1,2}^{100^{1,2}} = -t_{2,1}^{010^{1,2}} = 0.1566$ duo to the symmetry. The hopping $t_{1,2}^{100^{1,2}}$ and $t_{2,1}^{100^{1,2}}$ are different. The first is the hopping between the $|x^2 - y^2, 1, T\rangle$ and $|3z^2 - 1, 2, T\rangle$ in the direction 100 that is the long bond for the site 1, while, the second is the hopping between the $|x^2 - y^2, 2, T\rangle$ and $|3z^2 - 1, 1, T\rangle$ in the direction 100 that is the short bond for the site 2. The hopping integrals are larger in the plane $\mathbf{x}_T\mathbf{y}_T$ respect to the hopping in the direction \mathbf{z}_T . The only exception is the hopping $t_{22}^{001} = -0.2921$ eV because is between two orbital elongated in the \mathbf{z}_T direction. The main hopping parameters of the KCrF_3 compound are $t_{1,1}^{100^{1,2}}$, $t_{1,1}^{010^{1,2}}$ and t_{22}^{001} in all the phases.

7.2.2 Monoclinic phase

In the monoclinic case we have 4 different elements of the basis. We define this basis in Fig. 39 and 40. We tabulate the hopping parameters in Table 10. In comparison to the tetragonal case with e_g basis, the main hopping integrals shrink by 10-20%. In this case, we have also the reduction of the bandwidth.

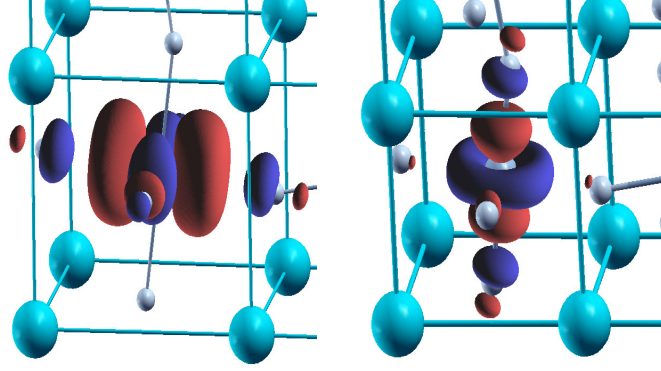


Figure 40: $|\omega_{n\mathbf{R}}^{e_g}\rangle$ for the monoclinic case for the site 2 used as basis to calculate hopping parameters. We have two orbitals on the site 2; we call $|x^2 - y^2, 2, M\rangle$ the state similar to $|x^2 - y^2\rangle$ (left panel) and $|3z^2 - 1, 2, M\rangle$ the state similar to $|3z^2 - 1\rangle$ (right panel).

Table 10: The basis is composed by $|x^2 - y^2, 1, M\rangle$, $|x^2 - y^2, 2, M\rangle$, $|3z^2 - 1, 1, M\rangle$ and $|3z^2 - 1, 2, M\rangle$. Hopping integrals $t_{j,j'}^{i,i'}$ from a site i with orbital j to neighboring site i' with orbital j' for the monoclinic structure. The orbital 1 is $|x^2 - y^2\rangle$, the orbital 2 is $|3z^2 - 1\rangle$. The connecting vector is $\mathbf{T} = l\mathbf{x}_M + m\mathbf{y}_M + n\mathbf{z}_M$; the hopping integrals are tabulated up to the first neighbors. ϵ_j^i is the energy on site for the orbital j on the site i . All energies are in eV.

lmn	$t_{1,1}^{1,2}$	$t_{1,2}^{1,2}$	$t_{2,1}^{1,2}$	$t_{2,2}^{1,2}$
100	-0.1638	0.1207	0.0835	-0.0721
010	-0.1630	-0.0866	-0.1667	-0.0673
001	0.0330	-0.0723	0.0522	-0.2532

lmn	ϵ_1^1	ϵ_1^2	ϵ_2^1	ϵ_2^2	$t_{1,2}^{1,1}$	$t_{1,2}^{2,2}$
000	0.7329	0.8435	1.1988	1.1014	0.4136	-0.3156

7.2.3 Cubic phase

We tabulate the hopping parameters in Table 11 for the cubic phase at the experimental volume of the tetragonal phase. The d_{3z^2-1} and the $d_{x^2-y^2}$ must be degenerate at Γ point, therefore the energy on site is equal for the two orbitals. Some hopping between the d_{3z^2-1} and the $d_{x^2-y^2}$ orbital are zero because of the symmetry. Moreover, the high symmetry makes equivalent the direction 100 and 001 up to a phase factor. The main hopping parameters are larger, but, because of the null hopping the total bandwidth is

smaller than the other phases.

Table 11: The basis is composed by $|x^2 - y^2, 1, C\rangle$, $|x^2 - y^2, 2, C\rangle$, $|3z^2 - 1, 1, C\rangle$ and $|3z^2 - 1, 2, C\rangle$. Hopping integrals $t_{j,j'}^{i,i'}$ from a site i with orbital j to neighboring site i' with orbital j' for the cubic structure. The orbital 1 is $|x^2 - y^2\rangle$, the orbital 2 is $|3z^2 - 1\rangle$. The connecting vector is $\mathbf{T} = l\mathbf{x}_C + m\mathbf{y}_C + n\mathbf{z}_C$; the hopping integrals are tabulated up to the first neighbors. ϵ_j^i is the energy on site for the orbital j on the site i . All energies are in eV.

lmn	$t_{1,1}^{1,2}$	$t_{1,2}^{1,2}$	$t_{2,1}^{1,2}$	$t_{2,2}^{1,2}$
100	-0.2231	0.1238	0.1238	-0.0801
010	-0.2231	-0.1238	-0.1238	-0.0801
001	-0.0087	0.0000	0.0000	-0.2944

lmn	$\epsilon_1^1 = \epsilon_1^2$	$\epsilon_2^1 = \epsilon_2^2$	$t_{1,2}^{1,1}$	$t_{1,2}^{2,2}$
000	0.9906	0.9906	0.0000	0.0000

At high symmetry, we can observe that many hopping parameters are zero. At the same time the main hopping parameters $t_{2,2}^{001,1,2} = -0.2944$ and $t_{1,1}^{100,1,2} = -0.2231$ increase respect to the other phases. The reduction of the main hopping parameters due to the lowering of the symmetry is a very general concept. The low symmetry produces new hopping that are zero (or lower) at higher symmetry, and make lower the main hopping parameters. We observed the same in strontium ruthenate oxide compound, where the rotations in multilayer ruthenates make lower the hopping $t_{xy,xy}^{100}$.

7.3 The *MLWF* basis

As in the previous paragraph, we calculate hopping parameters for the tetragonal and monoclinic phases, but we now use the *MLWF* basis. We can observe that the *MLWF* basis and hopping parameters are similar to the previous case for the tetragonal structure but are completely different for the monoclinic. We call $|j, i, T\rangle$ ($|j, i, M\rangle$) the state of the orbital j on the site i of the tetragonal (monoclinic) structure. We do not have the crystal field basis, but the *MLWF* basis. We put $j=1$ for the wave function in plane (similar to $x^2 - r^2$) and $j=2$ for the wave function out of plane (similar to $3z^2 - 1$).

7.3.1 Tetragonal phase

We show the *MLWF* basis for the tetragonal case in Fig. 41 and the hopping parameters in Table 12. Basically, the *MLWF* basis and e_g basis are very similar, therefore, the

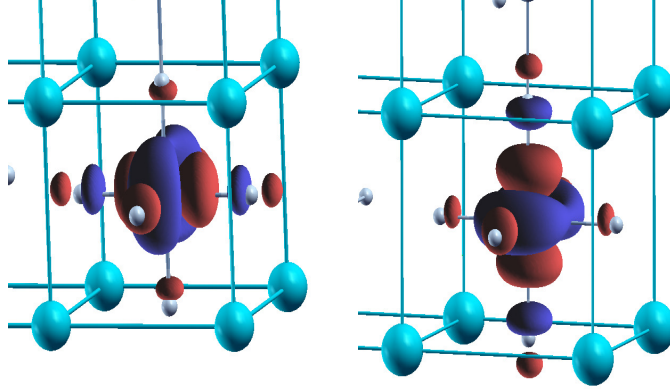


Figure 41: *MLWFs* for the tetragonal case for the site 1 used as basis to calculate hopping parameters. We have two orbitals on the site 1; we call $|1, 1, T\rangle$ (left panel) and $|2, 1, T\rangle$ (right panel). The Cr sites are equivalent but the two octahedra have different orientation, so the total number of elements of the basis is 4. We call $|1, 2, T\rangle$ and $|2, 2, T\rangle$ the states that are on the site 2.

hopping parameters too are extremely similar. We can observe that the biggest difference between two basis is a different wave function behaviour along the two different Cr-F bond in the plane $\mathbf{x}_T\mathbf{y}_T$.

Table 12: Hopping integrals $t_{j,j'}^{i,i'}$ between the state $|j, i, T\rangle$ and the state $|j', i', T\rangle$ for the tetragonal structure. The connecting vector is $\mathbf{T} = l\mathbf{x}_T + m\mathbf{y}_T + n\mathbf{z}_T$; the hopping integrals are tabulated up to the first neighbors. The *MLWF* basis is composed by $|1, 1, T\rangle$, $|1, 2, T\rangle$, $|2, 1, T\rangle$ and $|2, 2, T\rangle$. ϵ_j^i is the energy on site for the *MLWF* $|j, i, M\rangle$. All energies are in eV.

lmn	$t_{1,1}^{1,2}$	$t_{1,2}^{1,2}$	$t_{2,1}^{1,2}$	$t_{2,2}^{1,2}$
100	-0.1739	0.1384	0.1241	-0.0968
010	-0.1739	-0.1241	-0.1384	-0.0968
001	0.0439	-0.0896	0.0896	-0.2921

lmn	$\epsilon_1^1 = \epsilon_1^2$	$\epsilon_2^1 = \epsilon_2^2$	$t_{1,2}^{1,1}$	$t_{1,2}^{2,2}$
000	0.8343	1.0590	0.3984	-0.3984

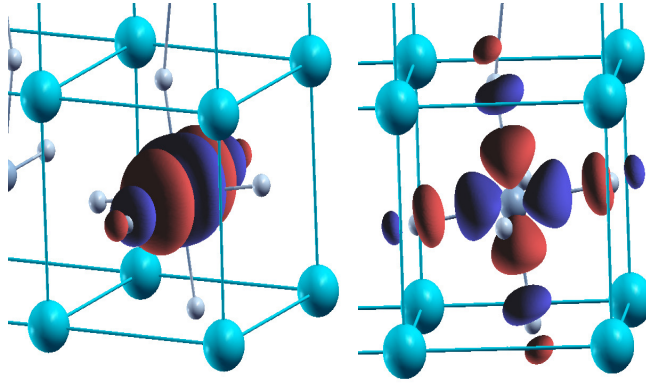


Figure 42: *MLWFs* for the monoclinic case for the site 1 used as basis to calculate hopping parameters. We have two orbitals on the site 1; we call it $|1, 1, M\rangle$ (left panel) and $|2, 1, M\rangle$ (right panel).

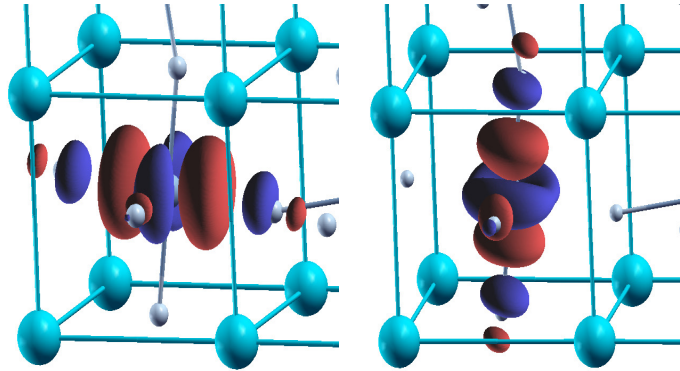


Figure 43: *MLWFs* for the monoclinic case for the site 2 used as basis to calculate hopping parameters. We have two orbitals on the site 2; we call it $|1, 2, M\rangle$ (left panel) and $|2, 2, M\rangle$ (right panel).

7.3.2 Monoclinic phase

In the monoclinic case we have four different *MLWFs*. We define this basis in Fig. 42 and 43. We tabulate the hopping parameters in Table 13. Unlike the previous case, we have nodes in the $|2, i, M\rangle$ Wannier functions along the Cr-F long bond. The Wannier functions of the type-2 octahedron are similar to the Wannier functions of the previous cases, but the Wannier functions of the type-1 octahedron are completely different (Fig. 42). For this reason, Table 13 is significantly different from the previous tables. On site 1 (Fig. 42), we have that the orbital is $|\theta\rangle \approx |3l^2 - 1\rangle$. We can observe that the *MLWFs* are like $|3l^2 - 1\rangle$ and $|s^2 - z^2\rangle$ present in KCuF_3 [115]. In the KCrF_3 we have 2 electrons

Table 13: The Hopping integrals $t_{j,j'}^{i,i'}$ between the state $|j, i, M\rangle$ and the state $|j', i', M\rangle$ for the monoclinic structure. The connecting vector is $\mathbf{T} = l\mathbf{x}_M + m\mathbf{y}_M + n\mathbf{z}_M$; the hopping integrals are tabulated up to the first neighbors. The *MLWF* basis is composed by $|1, 1, M\rangle$, $|1, 2, M\rangle$, $|2, 1, M\rangle$ and $|2, 2, M\rangle$. All energies are in eV. ϵ_j^i is the energy on site for the *MLWF* $|j, i, M\rangle$.

lmn	$t_{1,1}^{1,2}$	$t_{1,2}^{1,2}$	$t_{2,1}^{1,2}$	$t_{2,2}^{1,2}$
100	-0.1957	0.1516	0.0204	-0.0169
010	-0.0818	-0.0537	-0.2253	-0.1072
001	0.0007	0.0467	0.0633	-0.2568

lmn	ϵ_1^1	ϵ_1^2	ϵ_2^1	ϵ_2^2	$t_{1,2}^{1,1}$	$t_{1,2}^{2,2}$
000	0.5266	0.8510	1.4248	1.0743	0.0972	-0.3021

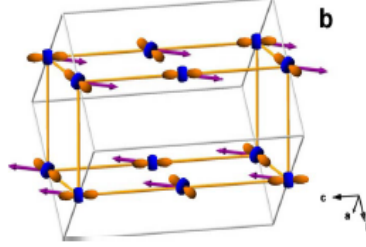


Figure 44: Experimental picture of orbital order G-type for the monoclinic and AFM phase of KCrF_3 . From [104].

in the 3d shell, instead, in KCuF_3 we have one hole in the 3d shell. In Table 13, we can observe a difference in the crystal field splitting in comparison to the other cases. The amount $\epsilon_2^1 - \epsilon_1^1 = 0.90$ eV is the difference of the energy on-site for the two Wannier functions of site 1, this value is greater than others value for this material (0.2-0.3 eV). Another observation is that the hopping integrals for the $|3l^2 - 1\rangle$ are large in the direction of the long (-0.1957 and 0.1516 eV) while are small in the direction of the short (-0.0818 and -0.0537 eV). We have the opposite for the $|s^2 - z^2\rangle$, the hopping are large along the short (-0.2253 and -0.1072 eV) and extremely small in the direction of the long bond (0.0204 and -0.0169 eV).

All these results confirm the experimental picture of orbital order in Fig. 44. In particular, it is sufficient to check the energy on site of *MLWF* in Table 13. We have that $\epsilon_1^1 = 0.5266$ for the $|3l^2 - 1\rangle$ orbital on site 1 (Fig. 42 left panel), while $\epsilon_1^2 = 0.8510$ and $\epsilon_2^2 = 1.0743$ for the site 2 where we have an orbital similar to LaMnO_3 .

7.4 Cococcioni method

The evaluation of the Coulomb repulsion is an important task to understand the physics of the strongly correlated system. We apply the Cococcioni method [116] to calculate the Coulomb repulsion in self-consistent way. We compute the values of $U_{eff} = U - J$ for the Cr atoms in the simplified Dudarev $LSDA+U$ approach for the estimation of the Coulomb repulsion. The result of Cococcioni method depends on the value of occupation numbers, for this reason the algorithm is not so stable and the value of U greatly depends on the kind of atomic positions used for the calculation (experimental, relaxed, full relaxed). Other methods based on polarization and band structure may be more accurate [117]. For the experimental atomic positions of reference [104] we have: $U_{eff}^{Tetragonal} = 3.2$ eV, $U_{eff}^{MonoclinicSite1} = 3.4$ eV and $U_{eff}^{MonoclinicSite2} = 4.0$ eV while U_{eff} used is 5.12 eV. Starting from the experimental atomic positions of $LaMnO_3$, we obtain $U_{eff}^{LaMnO_3} = 2.7$ eV. In the Cococcioni method the U_{eff} is calculated from the curvature of the energy vs. occupation number, but $LSDA + U_{eff}$ does not reduce the curvature to a great extent. To reduce this curvature completely, we need to recalculate U_{eff} using $LSDA + U_{eff}$. Using this technique the value of U_{eff} for these systems is around 9 eV and is 6.3 eV for $LaMnO_3$. The quantitative values of the Hubbard U calculated by Cococcioni method can not be taken as absolute reference, but we can deduce that $KCrF_3$ is more correlated than $LaMnO_3$.

7.5 Spin-orbit coupling and magnetic anisotropy

The role of the interplay between the observed lattice distortion and magnetocrystalline anisotropy, as well as the anisotropic and isotropic exchange interactions in this kind of compound is crucial [118]. At low temperature there are several different phases not completely understood in $KCrF_3$, it was proposed that the spin-orbit can be crucial to distinguish between these phases. We calculate the spin-orbit coupling effect and we observe that influence of the spin-orbit coupling is 2-3 orders of magnitude less than the volume effect. Spin-orbit coupling effects are greater in the monoclinic phase. We calculate magnetocrystalline anisotropy effect (MAE) for the monoclinic phase, in particular, the energy difference between the same system with different spin orientations. S_{x_M} , S_{y_M} and S_{z_M} are the spin orientations along the three pseudocubicaxis. We compute:

$$E_{MAE} = E(S_{z_M}) - E(S_{x_M}) \approx E(S_{z_M}) - E(S_{y_M}) = -0.3 \text{ meV} \quad (94)$$

As experimentally found in $KCrF_3$ and $LaMnO_3$, we have the spin orientation in the plane $x_M y_M$ as we compute in equation (94). But, we find spin along the y_M axis:

$$E_{MAE} = E(S_{x_M}) - E(S_{y_M}) = -0.03 \text{ meV} \quad (95)$$

while experimentally it is observed along the direction between \mathbf{x}_M and \mathbf{y}_M [104]. Other spin directions are been examined and do not give a lower energy. We find also the weak ferromagnetism orthogonal to the spin orientation, the net magnetization is $M \approx 10^{-4} - 10^{-5} \frac{\mu_B}{Cr\ atom}$ along \mathbf{z}_M for the ground state. Experimentally, the weak ferromagnetism of $KCrF_3$ is $2.5 * 10^{-3} \frac{emu}{g} = 2.5 * 10^{-3} \frac{Am^2}{Kg}$ [104] that is equivalent to $7 * 10^{-5} \frac{\mu_B}{Cr\ atom}$.

7.6 Conclusions

We obtained the hopping parameters for all the structural phases of $KCrF_3$. We calculate *MLWFs* for the tetragonal and monoclinic structures. The results of our calculations clearly show that $LaMnO_3$ and the tetragonal phase of $KCrF_3$ are not only structurally but also electronically very similar. We find *MLWFs* similar to $LaMnO_3$ for the tetragonal phase, instead, the monoclinic phase has two different orbitals. One octahedron has *MLWFs* that are $KCuF_3$ -like ($|3l^2 - 1\rangle$ and $|s^2 - z^2\rangle$), while the other octahedron of the monoclinic phase has also the orbital similar to $LaMnO_3$. The orbital order is G-type different from $LaMnO_3$ and $KCrF_3$. Using the Cococcioni method, we find that the Coulomb repulsion for $KCrF_3$ is greater than the Coulomb repulsion for $LaMnO_3$ in all the phases. The spin orientation is in the plane $\mathbf{x}_M\mathbf{y}_M$ for the monoclinic phase and the weak ferromagnetism is along the direction \mathbf{z}_M as for $LaMnO_3$.

8 Orbital order and ferromagnetism in $\text{LaMn}_{1-x}\text{Ga}_x\text{O}_3$

We study from first principles the magnetic, electronic, orbital and structural properties of the LaMnO_3 doped with gallium atoms. The gallium atoms reduce the Jahn-Teller effect, and accordingly reduce the charge gap. Surprisingly, the system does not go towards a metallic phase because of the kinetic energy reduction. The doping tends to reduce the orbital order by weakening the antiferromagnetic phase and by favoring an unusual insulating ferromagnetic phase.

8.1 Introduction

In recent years the series $\text{La}_{1-x}\text{A}_x\text{MnO}_3$, where A is a divalent metal, has been the object of a systematic investigation [119]. This is not only due to the discovery of the giant magnetoresistance in several members of the series but also to a strong interplay among orbital, lattice, spin and charge degrees of freedom. This interplay results in a large variety of magnetic arrangements and phase transitions depending on the hole doping. The giant magnetoresistance phenomena is observed in the ferromagnetic metallic phase [120]. The correlation between ferromagnetism and metallic behaviour has been explained by the double exchange mechanism [121] and the electron-phonon coupling is mainly due to the Jahn-Teller effect [122, 112]. The mother compound LaMnO_3 has been considered the prototype example of a cooperative Jahn-Teller system and orbital-order state [7]. The parent compound LaMnO_3 , shows an orthorhombic unit cell with a cooperative tetragonal deformation of the MnO_6 octahedra, Jahn-Teller like, at room temperature. The structural parameters are shown in Table 14. This compound develops long-range magnetic ordering

Table 14: Structural parameters of the $Pbnm$ (No. 62 in the International Tables) structure of the parent compound LaMnO_3 as reported by Elemans *et al.* [123], $a = 5.532 \text{ \AA}$, $b = 5.742 \text{ \AA}$, $c = 7.668 \text{ \AA}$ at 4.2 K.

Atoms & Wyckoff site	$\frac{x}{a}$	$\frac{y}{b}$	$\frac{z}{c}$
La (4c)	-0.010	0.049	$\frac{1}{4}$
Mn (4b)	$\frac{1}{2}$	0	0
O(1) (4c)	0.070	0.486	$\frac{1}{4}$
O(2) (8d)	0.724	0.309	0.039

below $T_N = 140\text{K}$ that is antiferromagnetic (AFM) of type A. The manganese moments are aligned in the $[010]$ direction with the spins coupled ferromagnetically in the ab plane

and antiferromagnetically along the c -axis.

Surprisingly, the replacement of Mn^{3+} by a non-magnetic non Jahn-Teller trivalent ion such as Ga^{3+} also induces long range ferromagnetism [124, 125, 126, 127, 128] without carrying hole doping. Without hole doping, the double-exchange mechanism is not active. Nevertheless, the ferromagnetic interactions can not be ascribed to any of the previous mechanisms. It was studied in the past, and it was shown the relationship between the static Jahn-Teller distortion of the MnO_6 octahedron and the orthorhombic distortion of the unit cell in the $LaMn_{1-x}Ga_xO_3$ series [124]. The replacement of manganese by the smaller gallium reduces both distortions and it is coupled with the appearing of a spontaneous magnetization [127]. The maximum ferromagnetic moment is achieved for $x=0.500$. For $x > 0.6$ the lack of Jahn-Teller effect makes the system cubic [128]. Moreover, these samples are also electrically insulators, unusual for a ferromagnetic compound. The gallium doping has dramatic effect at low concentration too, where one Ga atom increases the magnetic moment in an applied magnetic field up to $16 \mu_B$ per Ga atom [126]. This result is still not fully understood.

Here, we study from first principles the properties of the $LaMn_{1-x}Ga_xO_3$ at $x=0.000, 0.125, 0.250, 0.500$ considering different size supercells and substituting the Ga atom to the Mn atom in the centre of the octahedron, and we use the experimental volume from [123, 127] to construct the supercells. Due to the construction of the supercell, the net magnetic moment will be different from zero at $x=0.125, 0.250$. This chapter is organized as follows: we present the computational detail for the ab-initio calculations in the paragraph 2, while in the paragraph 3 we present the results from first principle studies, focusing on the octahedral distortions, the density of state (DOS) and the orbital order. Finally, in paragraph 4 we propose the possible origin of experimentally detected ferromagnetic phase.

8.2 Computational details

We perform spin-polarized first-principles density functional theory (DFT) calculations [6] using the Quantum Espresso program package [8], the GGA exchange-correlation functional of Perdew, Burke, and Ernzerhof [97], and the Vanderbilt ultrasoft pseudopotentials [129] in which the $La(5s, 5p)$ and $Mn(3s, 3p)$ semicore states are included in the valence. We used a plane-wave energy cut-off of 35 Ry and a Gaussian broadening of 0.01 Ry as in the reference[130]. These values for the plane-wave cutoff and the Gaussian broadening are used in all calculations presented in this chapter. The $10 \times 10 \times 10$ k-point grid is used

in all *DOS* calculations, while a $8 \times 8 \times 8$ grid used for the relaxation of the internal degrees of freedom. We optimized the internal degrees of freedom by minimizing the total energy are less than 10^{-4} Hartree and the remaining forces are inferior to 10^{-3} Hartree/Bohr, while fixing the lattice parameter a , b and c to the experimental values [123, 127]. After obtaining the *DFT* Bloch bands within *GGA*, we use the occupation matrix to obtain the orbital order parameter. For the *DOS* calculations, we used a Gaussian broadening of 0.02 eV to have an accurate measurement of the band gap.

The basic approach of *DFT* is the local spin density approximation (*LSDA*). To go beyond *LSDA*, it has been proposed to include the Coulomb repulsion U into the *LSDA* theory giving rise to the so-called *LSDA+U* theory. The first *LSDA+U* was introduced by Anisimov and his coworkers [107, 108]. Here, we use the rotational invariant form introduced by Lichtenstein [109] in his spherically averaged and simplified Dudarev approach [131]. In the Dudarev approach, there is just an adjustable parameter $U_{eff} = U - J$. The functional energy in *LSDA+U* (E_{LSDA+U}) is the sum of the energy functional in *LSDA* (E_{LSDA}) plus the Hubbard term as we can see in expression (96):

$$E_{LSDA+U} = E_{LSDA} + \frac{U_{eff}}{2} \sum_{m\sigma} (n_{m\sigma} - n_{m\sigma}^2) \quad (96)$$

where $n_{m\sigma}$ is the occupation number of the orbital m with spin σ . Basically, the Dudarev approach neglects the off diagonal $\langle mm' | \frac{1}{r_1 - r_2} | m'' m''' \rangle$ terms and performs the approximations of equation (97) and (98) in comparison to the Lichtenstein approach [109]:

$$\langle mm' | \frac{1}{r_1 - r_2} | m' m' \rangle = U_{mm'} = U \quad (97)$$

$$\langle mm' | \frac{1}{r_1 - r_2} | m' m \rangle = J_{mm'} = J \quad (98)$$

A self-consistent method for the determination of U_{eff} was proposed by Cococcioni [116]. Starting from the observation of the non piecewise behaviour of the energy as function of the occupation number [108], he implemented a method to take in account the electron screening in the Hubbard repulsion. We used the refined approach suggested by Cococcioni seeking internal consistency for the value of U_{eff} . Once calculated the first value of U_{eff} from *LSDA* calculation, we performed the Cococcioni technique for the functional *LSDA+U_{eff}* obtaining a correction to the U_{eff} value and repeating the procedure until the correction for the final value of U_{eff} vanishes. We construct several supercells required by the Cococcioni method and we calculate U_{eff} from the *AFM* configuration using experimental volume and atomic position from [132]. The well converged value for the *AFM* configuration of LaMnO₃ is $U_{eff}=6.3$ eV. The U_{eff} obtained in the *AFM* phase is in good agreement with other values used for LaMnO₃. In the literature, we find $U_{eff}=7.12$ eV [133], $U_{eff}=4.25$ eV [134, 135] and a scanning between 3.25 and 6.25 eV [112]. We

use the value $U=6.3$ eV in all the configurations and at all the doping concentrations of $\text{LaMn}_{1-x}\text{Ga}_x\text{O}_3$.

8.3 The ab-initio study of the electronic and structural properties of $\text{LaMn}_{1-x}\text{Ga}_x\text{O}_3$

We perform the relaxation of the atomic positions at fixed experimental volume for some doping concentrations in *LSDA* in the *AFM* spin configuration using several supercells. After the relaxation, we calculate the density of state, the distortion and the orbital order in *LSDA + U* using the U calculated by the Cococcioni method. Pickett [132] shows that, in *LSDA* approximation, the gap of *AFM* phase of LaMnO_3 is entirely due to the octahedral distortion. We find the same result, so, we can conclude that the gap in *LSDA+U_{eff}* is a rough sum of the contribution due to the distortion plus the contribution due to the Coulomb repulsion U_{eff} . The undoped LaMnO_3 has an experimental gap of 1.2 eV [136], so, we expect that its ferromagnetic phase is insulating, but, it is a half-metal [130]. We find a metal also in the *LSDA + U* approach, instead, the $\text{LaMn}_{1-x}\text{Ga}_x\text{O}_3$ is an insulator. We are not able to reproduce a ferromagnetic insulator within an ab-initio approach. It is known in literature [106], that it is a hard task to reproduce the magnetic stability of LaMnO_3 because the half-metal ferromagnetic phase is very stable. For these reasons, we will examine the influence of the Ga doping on the *AFM* phase. In the LaMnO_3 compound, the tetravalent Mn^{3+} is in the high spin configuration $t_{2g}^3e_g^1$. For every Mn atom present in the supercell, there is one occupied e_g level with majority spin.

8.3.1 Octahedral Distortion

We calculate the geometrical properties of the system: the Mn-O-Mn bond angle, the Ga-O-Mn bond angle and the octahedra parameters. The geometric angles, shown in Table 15, tend to increase going towards 180° when the Jahn-Teller is completely lost. Experimentally, the lack of the Jahn-Teller distortion at $x > 0.6$ is observed [128]. It is very interesting to observe that this effect is more evident in the plane without Ga atoms, because we have that the Mn-O-Mn bond angle is greater than the Ga-O-Mn.

We calculate, in Table 16 and 17, the Mn-O and the Ga-O distances for all the kinds of octahedra: the gallium octahedron, the octahedron of the Mn first-neighbour in the *ab* plane of the Ga atom, the octahedron of the Mn first-neighbour along the *c* direction of the Ga atom and the Mn octahedra far from the gallium. We find the reduction of the

Table 15: Geometric angles as a function of the doping in the plane ab . There are empty spaces in the table, because these values are not allowed by the geometrical arrangement of the atoms in the used supercells.

Doping	Mn-O-Mn angle	Ga-O-Mn angle
x= 0.000	160°	
x= 0.125	163°	162°
x= 0.250	164°	162°
x= 0.500		164°

Jahn-Teller effect, the long bonds are shorter than the undoped case and the short bonds become longer. However, this reduction does not exhibit a monotonic and homogeneous trend. For instance, the first-neighbour in the ab plane at $x= 0.250$ is distorted similarly to the mother compound. This is due to the alternate distortions induced by gallium atom as we will see in the orbital order.

Table 16: Geometric distances of the gallium octahedra and Mn octahedra that are not first-neighbours of gallium. We call it long (l), short (s) and medium (m). The unit is angstrom. There are empty spaces in the table, because these values are not allowed by the geometrical arrangement of the atoms in the used supercells.

Doping	Mn-l	Mn-s	Mn-m	Ga-l	Ga-s	Ga-m
x= 0.000	2.120	1.949	1.989			
x= 0.125	2.10	1.95	1.97	2.061	1.949	2.007
x= 0.250	2.094	1.947	2.000	2.088	1.924	2.021
x= 0.500				2.053	1.947	2.005

Table 17: Geometric distances of the first-neighbours of Ga octahedra. Mn ab is the manganese atom first-neighbour of the Ga atom in the ab plane, instead Mn c is the manganese atom first-neighbour along the c -axis. We call it long (l), short (s) and medium (m). The unit is angstrom. There are empty spaces in the table, because these values are not allowed by the geometrical arrangement of the atoms in used supercells.

Doping	Mn ab-l	Mn ab-s	Mn ab-m	Mn c-l	Mn c-s	Mn c-m
x= 0.000						
x= 0.125	2.119/2.088	1.945/1.975	2.005/1.975	2.095	1.950	1.965
x= 0.250	2.137	1.960	1.977	2.093	1.948	1.965
x= 0.500	2.067	1.952	2.002			

8.3.2 Density of states

We calculate the density of state of the *AFM* $\text{LaMn}_{1-x}\text{Ga}_x\text{O}_3$ to investigate the effect of the reduced Jahn-Teller distortion. We put the Ga atom in the spin up plane, and this spatial inhomogeneity breaks the equivalence between the spin up and spin down properties. The spin up and spin down *DOS* contributions are different also for an *AFM* phase. We observe in Fig. 45 that the Ga atoms do not have any influence at low energy, the last occupied bands have an e_g character, once more, as for the mother compound. Basically, the Ga atoms are effective vacancies for the system at low energy. The Ga *DOS* is different from zero because of small hybridization with the manganese atoms. This is observed in the metallic system $\text{La}_{\frac{2}{3}}\text{Sr}_{\frac{1}{3}}\text{MnO}_3$ too, where the Ga doping removes electronic states at Fermi level creating an insulator compound [137]. Because of the Coulomb repulsion, the oxygen contributions are between the t_{2g} and the e_g to make a charge-transfer insulator. The Jahn-Teller distortion decreases as x increases. Since part of the gap is due to the distortion the lack of the distortion reduces the gap when we add the gallium doping.

However, when we increase the Ga concentration, once more, the gap increases again because the diminution of the coordination number as we can see in Fig. 46. At $x=0.125$, there is a gap only because of the Coulomb repulsion. At this concentration, the *LSDA* simulations give us a metal. The gap in the plane where is present the Ga atom (Δ_{\uparrow}) is always greater than the gap in the other plane (Δ_{\downarrow}), because the Ga atom in the spin channel \uparrow reduces the coordination number. Moreover, the diminution of the coordination number strongly suppress the bandwidth of the e_g electron near the gap for the electron in the Ga plane W_{\uparrow} , while the e_g electron of the other spin present a greater bandwidth W_{\downarrow} as we can see in the Table 18. At $x=0.500$ there is a decrement of the bandwidth in both spin channels because both contain a Ga atom that reduces the coordination number.

8.3.3 Orbital order

To calculate the orbital order, we use the notation of the article [112]

$$|\theta\rangle = \cos\frac{\theta}{2}|3z^2 - 1\rangle + \sin\frac{\theta}{2}|x^2 - y^2\rangle \quad (99)$$

where $|3z^2 - 1\rangle$ and $|x^2 - y^2\rangle$ represent the e_g eigenstates of manganese. We use the 5×5 occupation number matrix to determine $|\theta\rangle$ by formula (99). We calculate the θ angle for all the octahedra at several concentrations. Now, let us consider two equivalent atoms with the direction of one orbital rotated of 90 degrees with respect to the other orbital.

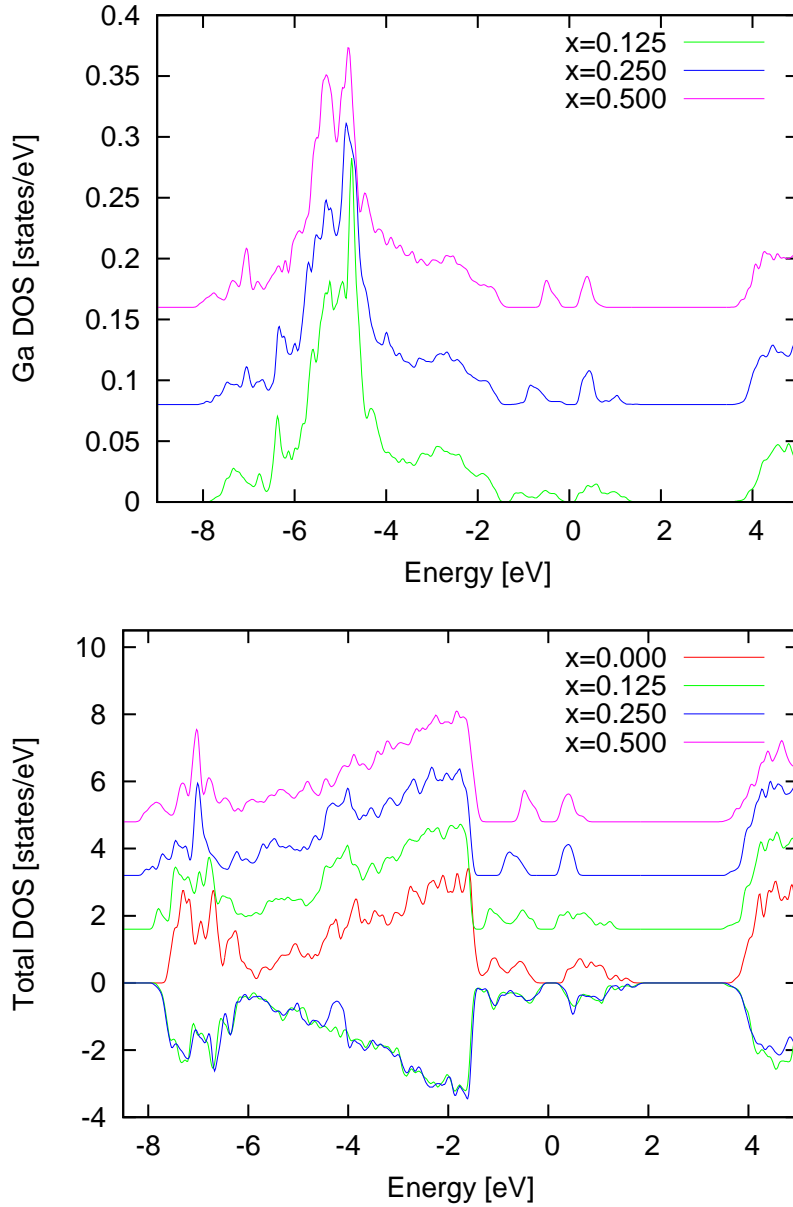


Figure 45: Plotting of the density of state of gallium atom (upper panel) and total density of state (lower panel) per formula unit. The low energy gallium contribution is negligible. The *DOS* contribution between -6 eV and -2 eV is due to the oxygens, while from -8 eV to -6 eV is due to the t_{2g} of the majority spin.

Using this notation in this case, the θ values for the two atoms are opposite. The sign gives us information just about the direction of the orbital. Considering that all the orbitals are in the direction of the long bond in LaMnO_3 , we will just consider the modulus of the theta value in all the cases studied.

We find, for the undoped case, $\theta = 103^\circ$ while the experimental orbital order is $\theta = 108^\circ$ [138]. When θ tends to 90° , we find a modification of the orbital order and a reduction

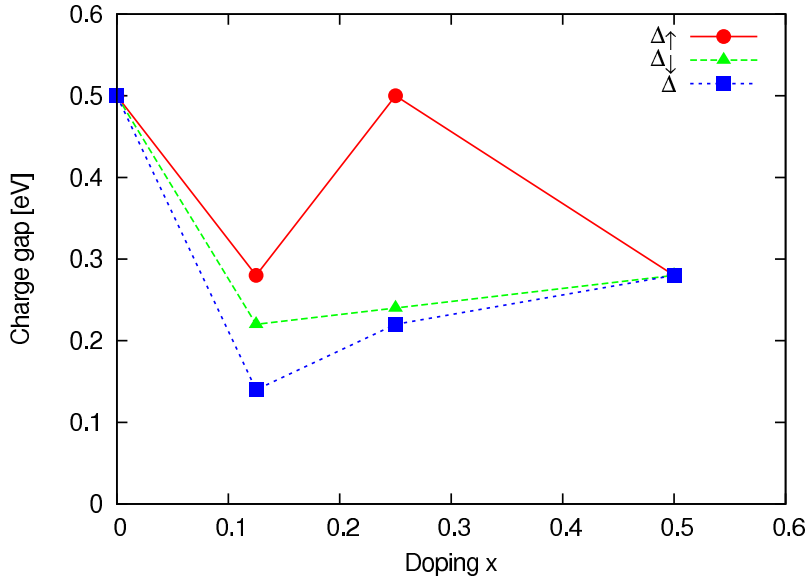


Figure 46: Evolution of the gap as a function of the doping. We find a strong reduction of the gap at $x=0.125$ due to the breaking of the cooperative Jahn-Teller effect. At $x=0.250$ the gap increases again because the coordination number decreases. The spin channel \uparrow has a greater gap in comparison to the spin channel \downarrow , because the Ga atom in the spin channel \uparrow reduces the coordination number.

Table 18: Bandwidths of the e_g electrons. The unit is eV. The plane with spin up Mn contains the Ga atom at $x=0.125$ and $x=0.250$. Instead, at $x=0.500$ both planes contain a Ga atom.

Doping	W_{\uparrow}	W_{\downarrow}
x= 0.000 (experimental atomic positions)	1.45	1.45
x= 0.000 (relaxed position at exp. volume)	1.48	1.48
x= 0.125	1.32	1.68
x= 0.250	0.52	1.70
x= 0.500	0.66	0.66

of the length of the orbital. This is correlated, from a structural point of view, to the reduction of the Jahn-Teller effect. We present the results at $x=0.125$ and $x=0.250$ in Fig. 47 and 48, where we observe changes of the orbital order at long range too. In all the cases we observe a G -type structure of the orbital order. The G -type orbital order is the order for the hypothetical ferromagnetic phase in LaMnO_3 [139], that can be also insulating. Therefore, the gallium doping can induce an instability towards a new kind of orbital order that can drive the ferromagnetism in $\text{LaMn}_{1-x}\text{Ga}_x\text{O}_3$. In the article [139]

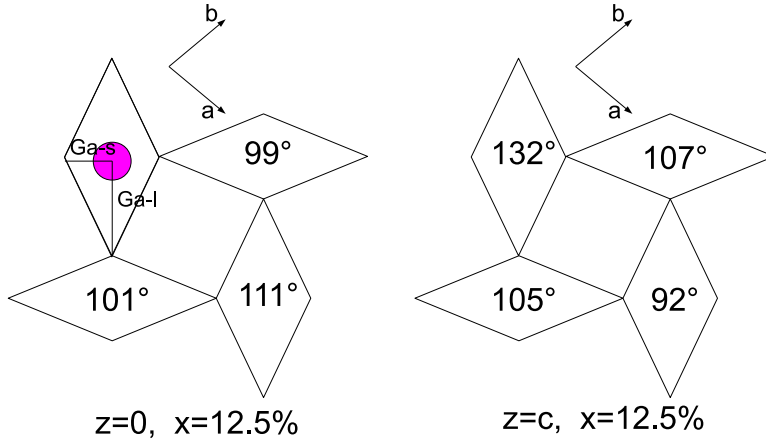


Figure 47: Orbital order for the Mn atoms at $x=0.125$. The Ga atom is pink. Ga-s and Ga-l are the short and the long bond of the gallium octahedron. The $d_{z^2} - r^2$ orbital up the gallium octahedron is strongly suppressed, because it does not hybridize with the gallium atom. Excluding the latter octahedron a G -type orbital order structure is observed.

this order is predicted for low value of J' (interaction between the t_{2g} spin), in our case the reduction of the coordination number might reduce the effective value J' . This G -type orbital order is in agreement with the geometrical distance calculated in the previous paragraph, stronger is the Jahn-Teller and higher is θ . The only one octahedron that is not in agreement with the G -type orbital order is the Mn above the Ga atom at $x=0.125$. In this case the $|3z^2 - 1\rangle$ is strongly suppressed. The same does not happen at $x=0.250$ where there is a different experimental volume and a different symmetry. At $x=0.500$, the θ value for the two equivalent Mn is 93° and the orbital order is strongly suppressed. The reduced coordination suppresses the cooperative Jahn-Teller effect and strongly modifies the orbital order, this is a different behaviour in comparison to the cubic LaMnO_3 , where the orbital order is still present although there are no distortions [140]. Therefore, the Ga impurity is more effective than the pressure to reduce to modify the orbital order.

If we look at the DOS and at the orbital order together, we conclude that the local DOS of atom with θ near 90° has a small gap. This result further suggests that the reduction of octahedron distortion, and subsequently of the θ value, tends to close the gap.

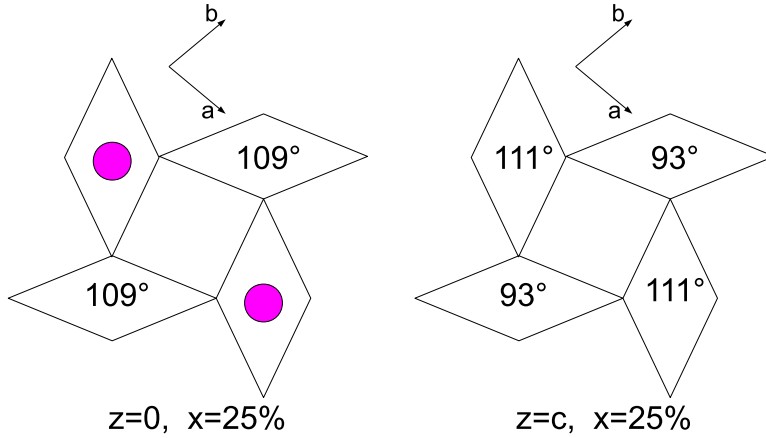


Figure 48: Orbital order for the Mn atoms at $x=0.250$. The Ga atom is pink. Ga-s and Ga-l are the short and the long bond of the gallium octahedron. The octahedra with the same orbital order are symmetrically equivalent. We do not have an octahedra with $\theta = 132^\circ$ because of the different symmetry and different experimental volume.

8.4 Magnetism

At low concentration, a large value for the magnetization is found in applied magnetic field [126], while ferromagnetism it is found at intermediate concentration and superparamagnetism at high concentration [127]. We need to discuss separately the two first cases.

8.4.1 Low concentration of Ga

We calculate the energy difference between the antiferromagnetic phase and the ferromagnetic phase for all the concentrations. The ab-initio magnetic ground state of LaMnO_3 is a non trivial problem [106], but we clearly find that the antiferromagnetic phase becomes weaker when we increase the gallium doping. At low concentration, we have an isolated gallium atom surrounded by the manganese atoms. It has been suggested that the large magnetic moment in an applied magnetic field can be due to a spin-flip of the manganese above the Ga atom [141], instead, we find this is strongly forbidden energetically. So, we propose at low concentration and in applied magnetic field that a spin-flip can happen, but, in the plane of the gallium impurity. This is possible because of the low energy differ-

ence between the configuration with a spin-flip and the antiferromagnetic configuration. This picture can be easily understood within the Ising approximation of the Mn localised moments. The in-plane ferromagnetic coupling in LaMnO_3 is very strong [142], so it is hard to break the ferromagnetic bounds if there are four first-neighbors, instead, the Ga atom reduces the coordination and the Mn magnetic moment becomes easier to orientate in an applied magnetic field.

8.4.2 Intermediate concentration of Ga

At intermediate concentrations a long-range ferromagnetic phase it is experimentally found. We analyse the possible occurrence of a correlated disordered configuration for the Ga-doping by inserting the two Ga atoms at different distances in the supercell at $x=0.250$ in the *AFM* phase. Also in this case, we perform the relaxation of the atomic position at fixed experimental volume, but, all the calculations of this paragraph are carried out in *LSDA* because they are performed using big supercells. In the *AFM* configuration, two types of doping are possible: a ferromagnetic doping and a non magnetic doping. In the first case, two Ga atoms substitute two Mn atoms with the same spin, creating a non-compensated ferromagnetism. In the second case, the two Ga atoms substitute two Mn atoms with different spin leaving the net magnetization equal to zero. We can observe all the possible configurations with supercells of 8 octahedra in Fig. 49. In Fig. 50, we set to zero the ground state energy and plot the energy of the system per formula unit as a function of the Ga-Ga distance in the supercell. Of course, also in this case we fix the experimental volume and minimize the force acting on the atoms to find the equilibrium atomic positions. We find that the ground state is when two Ga atoms are at distance d_1 , therefore when they are first-neighbour in the *ab* plane. This is a ferromagnetic ground state. This result is very easy to understand if we consider that, moving the only planar oxygen between the two Ga atoms, it is possible to reduce the distortion of the Ga octahedra without disturbing the Mn octahedra. In this way, the system minimizes the elastic energy and the total energy, hence creating a ferromagnetic ground state. We notice that all other configurations are higher in energy. In particular, when the Ga-Ga distance is d_5 we have the two Ga atoms first neighbour along the *c*-axis, but, the movement of the apical oxygen can not give us a great gain of elastic energy because the distortions are greater in the *ab* plane. Indeed, the bigger structural change between the real orthorhombic structure of LaMnO_3 and a hypothetical cubic structure is the position of the planar oxygens.

Then, the Ga substitution can creates a non-compensated ferromagnetism. This effect,

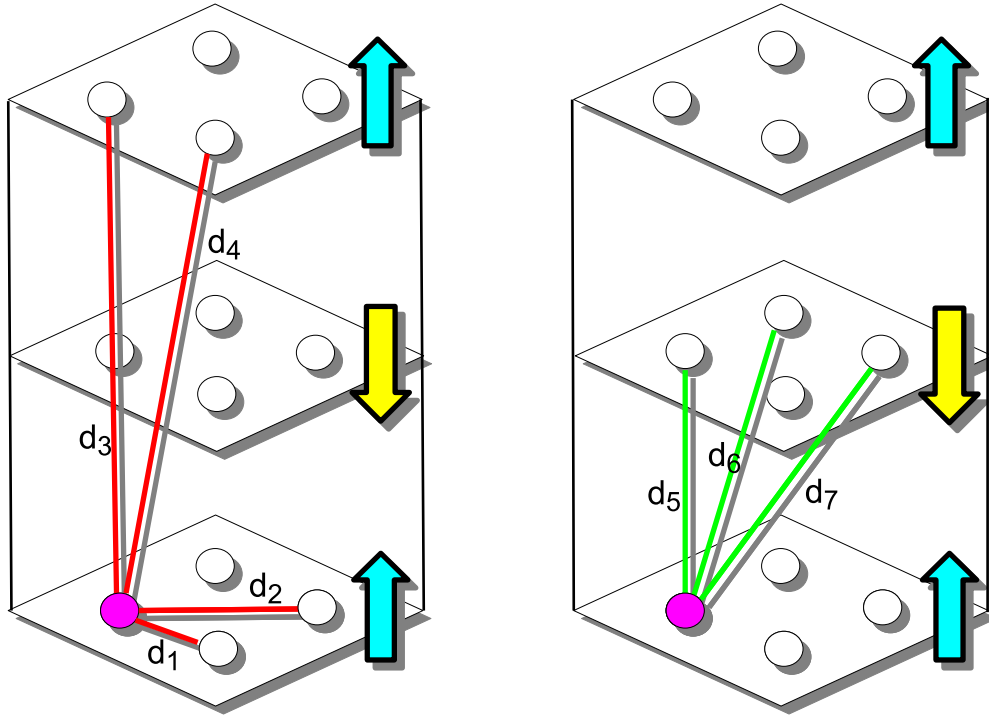


Figure 49: Non equivalent space configurations for the two Ga atoms in the supercells at $x= 0.250$. The red line links two Ga atoms in the same spin channel and the green line links two Ga atoms on two different spin channels.

together with a weaker *AFM* phase and the instability towards a *G*-type structure of the orbital order, can destroy the *AFM* phase favoring the onset of a long-rang ferromagnetic order. The non-compensated ferromagnetism alone is not sufficient to explain the ferromagnetic moment experimentally found at intermediate doping [127], that has a large magnetic moment per Mn atoms, but helps the system to cross to the ferromagnetic insulating phase. Near $x= 0.500$ the system has an insulating ferromagnetic phase which is quite difficult to reproduce by using ab-initio approaches. Differently from the metallic ferromagnetic phase, the non-compensated ferromagnetism is one possibility to reproduce a ferromagnetic insulator. This insulating ferromagnetic phase is also different from the cubic phase obtained under pressure by orbital splitting. Indeed, up to a pressure of 32 GPa, the system is a paramagnetic metal at room temperature and an antiferromagnetic metal at low temperatures, though this region of the phase diagram is not well explored [143].

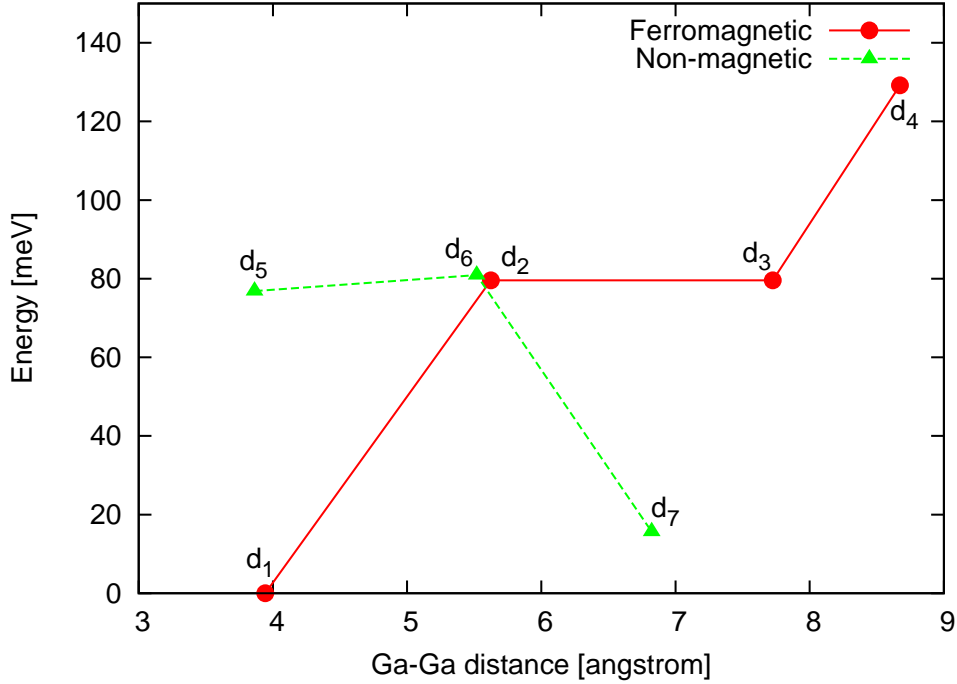


Figure 50: Energy differences as a function of the Ga-Ga distance in the supercells with 8 octahedra at $x=0.250$. We plot the energy differences per Ga atom. The red points are the magnetic configuration, while the green points are the non magnetic configuration. d_i with $i=1,\dots,7$ are the distances defined in the Fig. 49. The lines are guides for the eyes. The ground state is the magnetic configuration when two Ga atoms are first-neighbours in the ab plane.

8.5 Conclusions

We have calculated the density of state, the evolution of the orbital order and the octahedral distortion for several concentrations of $\text{LaMn}_{1-x}\text{Ga}_x\text{O}_3$. The Ga doping is an effective orbital and electronic vacancy. We find that the gallium doping, that reduces octahedral distortion, energetically disfavors the antiferromagnetic phase. The Ga doping weakens the Jahn-Teller effect highlighting electronic correlation. We argue that the large magnetization at low concentration in an applied magnetic field can be explained by a spin-flip of the in-plane first-neighbours of the gallium. We find that the ferromagnetic phase at high doping is due to a non-compensated ferromagnetism of the gallium site position.

9 Conclusions

In this Ph.D. thesis I have studied the interplay between structural distortion and spin-orbital degrees of freedom in tetravalent atoms based perovskite systems. This investigation has proved to be relevant to deeply understand the properties of these transition metal oxides. The applied methodology has made use of ab-initio like approaches as well as model Hamiltonian effective theories for both homogeneous and disordered configurations. In this context, we have considered different issues concerning the $n=1$ and $n=2$ ruthenates members of the Ruddsden-Popper series (i.e. Sr_2RuO_4 and $\text{Sr}_3\text{Ru}_2\text{O}_7$) and the derived eutectic phases $\text{Sr}_2\text{RuO}_4/\text{Sr}_3\text{Ru}_2\text{O}_7$, as well as the Ga-doped LaMnO_3 and the KCrF_3 compound. We started this analysis looking at the necessary and sufficient conditions to have metamagnetism in the mean field theory of single band. We continued applying this theory to the class of Sr-based ruthenates within a weak-coupling effective theory of multi-orbital itinerant systems. We have derived the criteria and the phase diagram related to the occurrence of paramagnetism, metamagnetism and ferromagnetism with respect to the strength of the Coulomb repulsion and the features of the electronic structure taking into account the know-how from the ab-intio study. We have studied the metamagnetic transition of the eutectic system $\text{Sr}_2\text{RuO}_4/\text{Sr}_3\text{Ru}_2\text{O}_7$, finding a metamagnetic crossover. This result has been related to the behaviour of the *DOS* at the Fermi level and the modification of its curvature close to the inclusion. Moreover, the changes of the *DOS* at the Fermi level are orbital dependent for the three t_{2g} Ru bands. In particular, depending on the level of interbands matching at the inclusion-host interface, the orbital dependent *DOS* can get suppressed or significantly enhanced. Due to the spatial dependence of the *DOS* variation and its derivatives near and at the inclusion, our results also indicate a tendency to an inhomogeneous magnetism in the eutectic system with a possible distribution of critical metamagnetic fields. Hence, a broadening of the first order transition can occur even at very low temperature where a sharp change in the magnetization is expected.

The pure phase $\text{Sr}_3\text{Ru}_2\text{O}_7$ does not present e_g bands at Fermi level, the rotations push the *VHS* below the Fermi level if compared to the Sr_2RuO_4 case. We are able to reproduce within *LDA* the key aspects of the Fermi surface topology as well as to understand the origin of the enhanced *DOS* close to the Fermi level and its role with respect to the metamagnetic instability. Starting from the complete analysis of the electronic structure for the bulk Sr_2RuO_4 and $\text{Sr}_3\text{Ru}_2\text{O}_7$ systems we have faced the problem of the electronic reconstruction at their interface. This problem turns out to be relevant for understanding the change in the physical properties observed in the eutectic phase made of crystalline domains of Sr_2RuO_4 interfaced to those of $\text{Sr}_3\text{Ru}_2\text{O}_7$. We have found a significant vari-

ation in the atomic positions for the heterostructure $\text{Sr}_2\text{RuO}_4/\text{Sr}_3\text{Ru}_2\text{O}_7$. These effects are more relevant in the nearest layers to the interface and in the $\text{Sr}_3\text{Ru}_2\text{O}_7$ domain, while are negligible on the rest of the Sr_2RuO_4 part. The most important effect is the off centre displacement of the Ru atoms along the c -axis. Moreover, the rotation of the octahedron within the $\text{Sr}_3\text{Ru}_2\text{O}_7$ domain is slight reduced at interface. This rotation reduction can strongly modify the position of the VHS near the Fermi energy and consequently affect the properties of the $\text{Sr}_3\text{Ru}_2\text{O}_7$ phase especially with respect to the metamagnetic behavior. The determination of the electronic structure represents an important issue to be undertaken in the future for getting a deeper understanding of the collective properties of the eutectic $\text{Sr}_2\text{RuO}_4/\text{Sr}_3\text{Ru}_2\text{O}_7$.

We comment that our model for analyzing the metamagnetism in the $\text{Sr}_3\text{Ru}_2\text{O}_7$, though has been constructed by combining the input from the ab-initio electronic structure with the effective correlated multi-orbital model Hamiltonian, still requires further refinements to catch some of the detailed aspects of the metamagnetic behavior observed in the $\text{Sr}_3\text{Ru}_2\text{O}_7$. Indeed, the anisotropy of the metamagnetic critical field would definitely imply an important role of the spin-orbit coupling. Still, the phenomenology observed around the quantum critical point goes beyond the target of the presented results. On the other hand, in the context of the heterostructures or surfaces based on the ruthenates the obtained outcome is fully novel. Apart from extra refinements and a direct bridge between the ab-initio analysis and the effective model for the nano-inclusion, the results can be of great interest as a platform for new experimental investigations.

Concerning the KCrF_3 compound, we know that it is a strongly correlated antiferromagnetic insulator with the monoclinic structure as ground state. For this system, the estimated Coulomb is stronger than that for the isoelectronic LaMnO_3 pointing to a possible major role of the electron-correlations with respect to the Jahn-Teller effect. The tetragonal phase shows many similarities with LaMnO_3 from the point of view of the electronic, magnetic and orbital properties. On the other hand, the monoclinic phase has two inequivalent Cr sites in the unit cell with two different orbitals on the two inequivalent sites: one is KCuF_3 -like and the other is more similar to LaMnO_3 orbital. We have been able to demonstrate that the equilibrium volume for the monoclinic phase is smaller than the equilibrium volume for the tetragonal phase in agreement with experimental data. The performed analysis reveals also the possibility of a weak-ferromagnetism as driven by the spin-orbit coupling. Because the strong Coulomb interaction, we argue that the structural tetragonal-monoclinic transition might be driven by pure electronic correlation mechanism.

With the aim to explore the tunability of the Jahn-Teller effect and in turn of the or-

bital order in the LaMnO_3 we have considered the role of the substitution of gallium with manganese. We have shown that such atomic substitutions acts like an effective orbital and electronic vacancy reducing the degree of manganese coordination. We have found that the gallium doping by reducing the octahedral distortions tends to energetically disfavor the antiferromagnetic phase. The gallium doping weakens the Jahn-Teller effect thus pointing to a potential dominance of the electronic correlations in controlling the collective behaviour. We have argued that that the large magnetization at low concentration in an applied magnetic field can be explained as a spin-flip rearrangement of the in-plane manganese that are first-neighbours of the gallium. We have found that the ferromagnetic phase at high doping is due to a non-compensated ferromagnetism originated by a correlated positional disorder of the gallium atoms that to minimize the energy associated to the Jahn-Teller effect tend to be located at specific distances rather than distribute in a complete random way.

About the 3d shell compound, both the topic treated in this thesis have been little studied. Because some similarities with LaMnO_3 , the doped KCrF_3 might be a very interesting research channel for the future, theoretically and experimentally. Despite this, the understanding of the nature of structural transition is a very interesting point. At the same time, we hope to see more studies on LaMnO_3 doped with elements of the same group of gallium, to understand if the correlated impurity can be relevant in other compounds. Moreover, there are interesting directions to be covered, as:

1. the change in the magnetic and orbital order,
2. the possible occurrence of metal-insulator transitions,
3. the achievements of new phases with unconventional transport properties as a function of the degree of substitution,
4. the role of electronic correlation in the strong coupling regime, etc...

To the light of the presented studies similar ideas can apply both to the LaMnO_3 and the KCrF_3 to get a deeper understanding of the fundamental interactions in Jahn-Teller correlated systems.

Acknowledgement

I acknowledge Dr. Mario Cuoco, Prof. Canio Noce and Prof. Eva Pavarini for guidance and for their daily support in my Phd period. I also acknowledge Dr. Silvia Picozzi and Dr. Alessandro Stroppa for the great period during the AQUIFER project and for useful and stimulating discussions. I would like to express my gratitude to Dr. Marjana Ležaić and Dr. Matteo Cococcioni for the aid in understanding of the ab-initio evaluation of effective Coulomb repulsion by linear response approach. I would like to acknowledge the many valuable suggestions made by Dr. Giovanni Cantele about the heterostructures. I have to thank my friends Dr. Alice Galdi and Dr. Danilo Puggioni for useful discussion about LaMnO_3 , and Prof. Eric Koch for the help in the first steps in studying the KCrF_3 compound. The start-up with the ab-initio theory was very hard, I must thank Dr. Bernard Amadon, Prof. Josef Zwanzinger and Igor Lukacevic for the help in the first steps of the ABINIT code and Dr. Guoren Zhang for the help in the use of the wannier90 code.

This work came from a collaboration among the Department of Physics of the University of Salerno, the CNR-SPIN institute, the Forschungszentrum Jülich and the Department of Physics of University of Naples "Federico II". Finally, I must thank my family for the great support in the last three years.

A Properties of one-dimensional density of state

We demonstrate some useful relation to calculate the analytic thermodynamic functional for the one-dimensional density of state for tight binding approach. We consider the density of state for single spin in equation (41) and calculate the filling $n(\varepsilon_F)$.

$$\begin{aligned}
 n(\varepsilon_F) &= \int_{-2t+\varepsilon_0}^{\varepsilon_F} \frac{d\varepsilon}{\pi \sqrt{(2t)^2 - (\varepsilon - \varepsilon_0)^2}} = \\
 &= \frac{1}{\pi} \int_{-1}^{\frac{\varepsilon_F - \varepsilon_0}{2t}} \frac{dx}{\sqrt{1 - x^2}} = \\
 &= \frac{1}{\pi} [\arcsin(x)]_{-1}^{\frac{\varepsilon_F - \varepsilon_0}{2t}} = \\
 &= \frac{1}{\pi} \left(\arcsin\left(\frac{\varepsilon_F - \varepsilon_0}{2t}\right) + \frac{\pi}{2} \right)
 \end{aligned}$$

The quantity $n(\varepsilon_F)$ is in the range $[0, 1]$. All the simplifications became from the *DOS* integrability. We can use the following trigonometric identity:

$$\arccos(x) + \arcsin(x) = \frac{\pi}{2} \quad (100)$$

to obtain

$$n(\varepsilon_F) = \frac{1}{\pi} \left(\arcsin\left(\frac{\varepsilon_F - \varepsilon_0}{2t}\right) + \arcsin\left(\frac{\varepsilon_0 - \varepsilon_F}{2t}\right) + \arccos\left(\frac{\varepsilon_0 - \varepsilon_F}{2t}\right) \right) = \frac{1}{\pi} \arccos\left(\frac{\varepsilon_0 - \varepsilon_F}{2t}\right) \quad (101)$$

Inverting the previous one

$$\cos(\pi n) = \frac{\varepsilon_0 - \varepsilon_F}{2t} \quad (102)$$

and calculating the sine we have the final formula:

$$2t \sin(\pi n) = \sqrt{(2t)^2 - (\varepsilon_F - \varepsilon_0)^2} \quad (103)$$

B Gibbs free energy of the one-dimensional Hubbard model in mean field approximation

It also possible to obtain the thermodynamic functional for the one-dimensional density of state in an other way. There are four equation to solve self-consistently

$$\begin{aligned}
 h &= \mu_{\uparrow} - \mu_{\downarrow} - 2U \left(\frac{n_{\uparrow} - n_{\downarrow}}{2} \right) \\
 n_{\uparrow} &= \int_{-2t+\varepsilon_0}^{\mu_{\uparrow}} \frac{d\varepsilon}{\pi \sqrt{(2t)^2 - (\varepsilon - \varepsilon_0)^2}} \\
 n_{\downarrow} &= \int_{-2t+\varepsilon_0}^{\mu_{\downarrow}} \frac{d\varepsilon}{\pi \sqrt{(2t)^2 - (\varepsilon - \varepsilon_0)^2}} \\
 n &= \frac{n_{\uparrow} + n_{\downarrow}}{2}
 \end{aligned} \tag{104}$$

where the equation (104) became from mean field approximation.

Using equation (102), it is possible to reduce the 4 equations to 2 equations with just two unknowns: n_{\uparrow} and n_{\downarrow}

$$\begin{cases} h = 2t(\cos(\pi n_{\downarrow}) - \cos(\pi n_{\uparrow})) + U(n_{\downarrow} - n_{\uparrow}) \\ n = \frac{n_{\uparrow} + n_{\downarrow}}{2} \end{cases}$$

We find 4 self-consistently solutions: $n_{\uparrow} = 1$, $n_{\downarrow} = 1$, $n_{\uparrow} = n_{\downarrow}$ and a not analytic solution for the non completely polarized ferromagnet. The first three solutions are extreme points of the thermodynamic functional. The non completely polarized solution is at edge of the domain and can be a relative minimum without be an extreme point. The paramagnetic solution always exist. It is possible to show that all the ferromagnetic solutions appear for

$$U > \begin{cases} \frac{1 - \cos(2n\pi)}{n} & \text{for } n < \frac{1}{2} \\ \frac{1 - \cos(2(1-n)\pi)}{(1-n)} & \text{for } n > \frac{1}{2} \end{cases}$$

The not completely polarized ferromagnetic solution is a maximum of the energy under the Stoner criterion and a minima when the criteria is satisfied, but is never the ground state.

The energy of the solutions can be derived from equation (6),(7) and (104) in the limit of zero temperature:

$$\begin{aligned}
 G(U, n_{\uparrow}, n_{\downarrow}, h) &= \frac{2t}{\pi} (n_{\uparrow} \pi \cos(\pi n_{\uparrow}) - \sin(\pi n_{\uparrow})) + \frac{2t}{\pi} (n_{\downarrow} \pi \cos(\pi n_{\downarrow}) - \sin(\pi n_{\downarrow})) \\
 &\quad - 2t \cos(\pi n_{\uparrow}) n_{\uparrow} - 2t \cos(\pi n_{\downarrow}) n_{\downarrow} + U n_{\uparrow} n_{\downarrow} - h \frac{n_{\uparrow} - n_{\downarrow}}{2}
 \end{aligned}$$

Now, we can insert the values of n_{\uparrow} and n_{\downarrow} found self-consistently to have the Gibbs free energy. We obtain the same result using equation (47) if we set $G(0) = 0$.

References

- [1] M. Imada, A. Fujimori, Y. Tokura Rev. Mod. Phys. **70**, 10391262 (1998).
- [2] E. Dagotto Rev. Mod. Phys. **66**, 763 (1994).
- [3] Heber, J. Enter the oxides. Nature **459**, 2830 (2009).
- [4] H. Y. Hwang, Y. Iwasa, M. Kawasaki, B. Keimer, N. Nagaosa, and Y. Tokura Nature Mat. **11**, 103-113 (2012).
- [5] Y. Maeno, H. Hashimoto, K. Yoshida, S. Nishizaki, T. Fujita, J. G. Bednorz, and F. Lichtenberg, Nature **372**, 532 (1994).
- [6] P. Hohenberg and W. Kohn, Phys. Rev. **136**, B864 (1964), W. Kohn and L. J. Sham, Phys. Rev. **140**, A1133 (1964).
- [7] P. Fazekas, *Lecture notes on electron correlation and magnetism*, Series in Modern Condensed Matter Physics, (World Scientific, Singapore, 1999).
- [8] P. Giannozzi *et al.*, J. Phys.: Condens. Matter **21**, 395502 (2009).
- [9] X. Gonze, G. M. Rignanese, M. Verstraete, J. M. Beuken, Y. Pouillon, R. Caracas, F. Jollet, M. Torrent, G. Zerah, M. Mikami, Ph. Ghosez, M. Veithen, J. Y. Raty, V. Olevano, F. Bruneval, L. Reining, R. Godby, G. Onida, D. R. Hamann, and D. C. Allan., Zeit. Kristallogr. **220**, 558-562 (2005).
- [10] G. Kresse, D. Joubert, Phys. Rev. B **59**, 1758 (1999).
- [11] A. A. Mostofi, J. R. Yates, Y. S. Lee, I. Souza, D. Vanderbilt and N. Marzari, wannier90: a tool for obtaining maximally-localised Wannier functions, Comput. Phys. Commun., **178**, 685 (2008).
- [12] Sugiyama *et al.* J. Phys. Soc. Japan **59**, 3331 (1990).
- [13] E. Stryjewski and N. Giordano, Adv. Phys. **26**, 487 (1977).
- [14] D. Vollhardt Rev. Mod. Phys. **56**, 99 (1984).
- [15] K. Held, M. Ulmke, N. Blümer, D. Vollhardt Phys. Rev. B **56**, 22, 14470 (1997).
- [16] L. Laloux, A. Georges and W. Krauth Phys. Rev. B **50**, 3092 (1994).
- [17] A. Klejnberg and J. Spalek Phys. Rev. B **57**, 12041 (1998).
- [18] R. Z. Levitin and A. S. Markosyan. "Itinerant Metamagnetism" Usp. Fiz. Nauk **155**, 623-657 (1988).

- [19] R. S. Perry, L. M. Galvin, S. A. Grigera, L. Capogna, A. J. Schofield, A. P. Mackenzie, M. Chiao, S. R. Julian, S. I. Ikeda, S. Nakatsuji, Y. Maeno, Phys. Rev. Lett. **86**, 2661 (2001).
- [20] G. Cao, L. Balicas, W. H. Song, Y. P. Sun, Y. Xin, V. A. Bondarenko, J. W. Brill, S. Parkin, and X. N. Lin, Phys. Rev. B **68**, 174409 (2003).
- [21] E. C. Stoner, Proc. R. Soc. London **A165**, 372 (1938).
- [22] S. A. Grigera, R. S. Perry, A. J. Schofield, M. Chiao, S. R. Julian, G. G. Lonzarich, S. I. Ikeda, Y. Maeno, A. J. Millis, and A. P. Mackenzie, Science **294**, 329 (2001).
- [23] B. Binz and M. Sigrist, Europhys. Lett. **65**, 816 (2004).
- [24] S. Ikeda, Y. Maeno, S. Nakatsuji, M. Kosaka, and Y. Uwatoko, Phys. Rev. B **62**, R6089 (2000).
- [25] L. D. Landau, Phys. Z. Sowjetunion **11**, 26 (1937), reprinted in Collected Papers of L. D. Landau, edited by D. ter Haar Pergamon, London, (1965), p. 193.
- [26] Kerson Huang, Statistical Mechanics, (New York, John Wiley and Sons, 1967).
- [27] K. G. Sandeman, G. G. Lonzarich and A. J. Schofield Phys. Rev. Lett. **90**, 16, 167005, (2003).
- [28] R. B. Griffiths, Phys. Rev. Lett. **24**, 715 (1970).
- [29] M. Takahashi, Prog. Theor. Phys. **42**, 1098 (1969).
- [30] T. Oguchi, Phys. Rev. B **51**, 1385 (1995).
- [31] D. J. Singh, Phys. Rev. B **52**, 1358 (1995).
- [32] I. Hase and Y. Nishihara, J. Phys. Soc. Japan, **65**, 3957 (1996).
- [33] C. Noce and M. Cuoco, Phys. Rev. B **59**, 2659 (1999).
- [34] P. K. de Boer and R. A. de Groot, Phys. Rev. B **59**, 9894 (1999).
- [35] I. I. Mazin, D. A. Papaconstantopoulos, and D.J. Singh, Phys. Rev. B **61**, 5223 (2000).
- [36] E. Pavarini and I. Mazin, Phys. Rev. B **74**, 035115 (2006).
- [37] A. P. Mackenzie *et al.*, Phys. Rev. Lett. **76**, 3786 (1996).
- [38] A. Damascelli *et al.* Phys. Rev. Lett. **85**, 5194 (2000).
- [39] R. A. Borzi, S. A. Grigera, R. S. Perry, N. Kikugawa, K. Kitagawa, Y. Maeno, and A. P. Mackenzie, Phys. Rev. Lett. **92**, 216403 (2004).

- [40] A. Tamai, M. P. Allan, J. F. Mercure, W. Meevasana, R. Dunkel, D. H. Lu, R. S. Perry, A. P. Mackenzie, D. J. Singh, Z. X. Shen, and F. Baumberger, *Phys. Rev. Lett.* **101**, 026407 (2008).
- [41] Z. Q. Mao, M. Zhou, J. Hooper, V. Golub, and C. J. O'Connor, *Phys. Rev. Lett.* **96**, 077205 (2006).
- [42] R. Gupta, M. Kim, H. Barath, S. L. Cooper, and G. Cao, *Phys. Rev. Lett.* **96**, 067004 (2006).
- [43] P. B. Allen, H. Berger, O. Chauvet, L. Forro, T. Jarlborg, A. Junod, B. Revaz, and G. Santi, *Phys. Rev. B* **53**, 4393 (1996).
- [44] M. Malvestuto, E. Carleschi, R. Fittipaldi, E. Gorelov, E. Pavarini, M. Cuoco, Y. Maeno, F. Parmigiani, and A. Vecchione, *Phys. Rev. B* **83**, 165121 (2011).
- [45] A. P. Mackenzie, R. K. W. Haselwimmer, A. W. Tyler, G. G. Lonzarich, Y. Mori, S. Nishizaki, and Y. Maeno, *Phys. Rev. Lett.* **80**, 161 (1998).
- [46] R. S. Perry, K. Kitagawa, S. A. Grigera, R. A. Borzi, A. P. Mackenzie, K. Ishida, and Y. Maeno, *Phys. Rev. Lett.* **92**, 166602 (2004).
- [47] Z. Q. Mao, K. D. Nelson, R. Jin, Y. Liu, and Y. Maeno, *Phys. Rev. Lett.* **87**, 037003 (2001).
- [48] Y. Maeno, T. Ando, Y. Mori, E. Ohmichi, S. Ikeda, S. Nishizaki, and S. Nakatsuji, *Phys. Rev. Lett.* **81**, 3765 (1998).
- [49] H. Yaguchi, M. Wada, T. Akima, Y. Maeno, and T. Ishiguro, *Phys. Rev. B* **67**, 214519 (2003).
- [50] M. Sigrist and H. Monien, *J. Phys. Soc. Jpn* **70**, 2409 (2001).
- [51] Y. A. Ying *et al.*, *Phys. Rev. Lett.* **103**, 247004 (2009).
- [52] R. Fittipaldi, A. Vecchione, S. Fusanobori, K. Takizawa, H. Yaguchi, J. Hooper, R. S. Perry, and Y. Maeno, *J. Cryst. Growth* **282**, 152 (2005).
- [53] S. Kittaka, S. Fusanobori, H. Yaguchi, S. Yonezawa, Y. Maeno, R. Fittipaldi, and A. Vecchione, *Phys. Rev. B* **77**, 214511 (2008).
- [54] J. Hooper, M. Zhou, Z. Q. Mao, Y. Liu, R. S. Perry, and Y. Maeno, *Phys. Rev. B* **73**, 132510 (2006).
- [55] R. Fittipaldi, D. Sisti, A. Vecchione, S. Pace, *Cryst. Growth and Design*, **7**, 2495 (2007).
- [56] R. Fittipaldi *et al.*, unpublished.

- [57] R. Fittipaldi, A. Vecchione, R. Ciancio, S. Pace, M. Cuoco, D. Stornaiuolo, D. Born, F. Tafuri, E. Olsson, S. Kittaka, H. Yaguchi, and Y. Maeno, *Europhys. Lett.* **83**, 27007 (2008).
- [58] R. Ciancio, H. Petterson, J. Borjesson, S. Lopatin, R. Fittipaldi, A. Vecchione, S. Kittaka, Y. Maeno, S. Pace, and E. Olsson, *Appl. Phys. Lett.* **95**, 142507 (2009).
- [59] O. Chmaisssen, J. D. Jorgensen, H. Shaked, S. Ikeda, and Y. Maeno, *Phys. Rev. B* **57**, 5067 (1998).
- [60] X. Gonze, *et al.* *Computer Phys. Comm.* **180**, 2582-2615 (2009).
- [61] J. M. Dickey and A. Paskin, *Phys. Rev. B* **1**, 851 (1970).
- [62] M. Strongin, R. S. Thompson, O. F. Kammerer, and J. E. Crow, *Phys. Rev. B* **1**, 1078 (1970).
- [63] S. Bose, P. Raychaudhuri, R. Banerjee, P. Vasa, and P. Ayyub, *Phys. Rev. Lett.* **95**, 147003 (2005).
- [64] W. H. Li, C. C. Yang, F. C. Tsao, and K. C. Lee, *Phys. Rev. B* **68**, 184507 (2003).
- [65] T. Moriya, *Spin fluctuations in itinerant electron magnetism*, Springer Series in Solid State Science.
- [66] E. P. Wohlfarth and P. Rhodes, *Philosof. Mag.* **7**, 1817 (1962).
- [67] M. Kawamura, H. Yaguchi, N. Kikugawa, Y. Maeno, and H. Takayanagi, *J. Phys. Soc. Jpn.* **74**, 531 (2005).
- [68] S. Kittaka, H. Taniguchi, S. Yonezawa, H. Yaguchi, and Y. Maeno, *Phys. Rev. B* **81**, 180510(R) (2010).
- [69] T. Shiroka *et al.*, preprint (2011).
- [70] D. Zola, private communication.
- [71] Goto T. *et al.*, *Solid State Commun.*, **72** (1989) 945; *Physica B*, **300** (2001) 167.
- [72] Grigera S. A. *et al.*, *Int. J. Mod. Phys. B*, **16** (2002) 3258.
- [73] Pfleiderer C., Julian S. R. and Lonzarich G. G., *Nature*, **414** (2001) 427.
- [74] S. A. Grigera, P. Gegenwart, R. A. Borzi, F. Weickert, A. J. Schofield, R. S. Perry, T. Tayama, T. Sakakibara, Y. Maeno, A. G. Green, and A. P. Mackenzie, *Science* **306**, 1154 (2004).
- [75] R. A. Borzi, S. A. Grigera, J. Farrell, R. S. Perry, S. J. S. Lister, S. L. Lee, D. A. Tennant, Y. Maeno, and A. P. Mackenzie, *Science* **315**, 214 (2007).

- [76] A. W. Rost, R. S. Perry, J. F. Mercure, A. P. Mackenzie, and S. A. Grigera, *Science* **325**, 1360 (2009).
- [77] A. M. Berridge, A. G. Green, S. A. Grigera, and B. D. Simons, *Phys. Rev. Lett.* **102**, 136404 (2009).
- [78] A. M. Berridge, S. A. Grigera, B. D. Simons, and A. G. Green, *Phys. Rev. B* **81**, 054429 (2010).
- [79] H. Y. Kee and Y. B. Kim, *Phys. Rev. B* **71**, 184402 (2005).
- [80] H. Yamase and A. A. Katanin, *J. Phys. Soc. Jpn.* **76**, 073706 (2007).
- [81] S. Raghu, A. Paramakanti, E. A. Kim, R. A. Borzi, S. A. Grigera, A. P. Mackenzie, and S. A. Kivelson, *Phys. Rev. B* **79**, 214402 (2009).
- [82] C. M. Puetter, J. G. Rau, and H.-Y. Kee, *Phys. Rev. B* **81**, 081105 (2010).
- [83] W. C. Lee, D. P. Arovas, and C. Wu, *Phys. Rev. B* **81**, 184403 (2010).
- [84] J. Farrell, R. S. Perry, A. Rost, J. F. Mercure, N. Kikugawa, S. A. Grigera, and A. P. Mackenzie, *Phys. Rev. B* **78**, 180409 (2008).
- [85] K. Iwaya, S. Satow, T. Hanaguri, N. Shannon, Y. Yoshida, S. I. Ikeda, J. P. He, Y. Kaneko, Y. Tokura, T. Yamada, and H. Takagi, *Phys. Rev. Lett.* **99**, 057208 (2007).
- [86] Millis A. J. *et al.*, *Phys. Rev. Lett.*, **88** (2002) 217204; Kim Y. B. and Millis A. J., *Phys. Rev. B*, **67** (2003) 085102.
- [87] A. M. Berridge *Phys. Rev. B* **83**, 235127 (2011).
- [88] H. Iwasawa *et al.*, *Phys. Rev. Lett.* **105**, 226406 (2010).
- [89] A. Liebsch, A. Lichtenstein, *Phys. Rev. Lett.* **84**, 1591 (2000).
- [90] D. J. Singh and I. I. Mazin *Phys. Rev. B* **63**, 165101 (2001).
- [91] James M. Rondinelli, Nuala M. Caffrey, Stefano Sanvito, and Nicola A. Spaldin, *Phys. Rev. B* **78**, 155107 (2008).
- [92] K. Maiti and R. S. Singh, *Phys. Rev. B* **71**, 161102 (2005).
- [93] T. Yokoya *et al.*, *Phys. Rev. B* **53**, 8151 (1996).
- [94] D. Zola, R. Fittipaldi, P. Tedesco, M. Polichetti, A. Vecchione, S. Pace, F. Laviano, E. Mezzetti, S. Kittaka, R. S. Parry, Y. Maeno unpublished.
- [95] D. I. Bilc and Ph. Ghosez *et al.*, *Phys. Rev. B* **77**, 165107 (2008).
- [96] Z. Wu and R. E. Cohen, *Phys. Rev. B* **73**, 235116 (2006).

- [97] J. P. Perdew, K. Burke, and M. Ernzerhof, *Phys. Rev. Lett.* **77**, 3865 (1996).
- [98] M. Fuchs, M. Scheffler, *Comput. Phys. Commun.* **119**, 67 (1999).
- [99] Huang *et al.* *Phys. Rev. B* **58**, 8515 (1998).
- [100] C. Piefke and F. Lechermann *Phys. Status Solidi B* **248**, No. 10, 2269-2275 (2011).
- [101] R. Matzdorf *et al.* *Science* **289**, 746 (2000).
- [102] S. Jin *et al.*, *Science* **264**, 413 (1994).
- [103] S. Margadonna and G. Karotsis, *J. Mater. Chem.* **17**, 2013 (2007).
- [104] Y. Xiao *et al.*, *Phys. Rev. B* **82**, 09437 (2010).
- [105] G. Giovannetti, S. Margadonna and J. van den Brink, *Phys. Rev. B* **77**, 075113 (2008).
- [106] H. Sawada, Y. Morikawa and K. Terakura, N. Hamada *Phys. Rev. B* **56**, 12154 (1997).
- [107] V. I. Anisimov, J. Zaanen and O. K. Andersen, *Phys. Rev. B* **44**, 943 (1991).
- [108] V. I. Anisimov, I. V. Solovyev, M. A. Korotin, M. T. Czyzyk and G. A. Sawatzky *Phys. Rev. B* **48**, 16929 (1993).
- [109] A. I. Liechtenstein, V. I. Anisimov, and J. Zaanen, *Phys. Rev. B* **52**, R5467 (1995).
- [110] M. Torrent, F. Jollet, F. Bottin, G. Zerah, and X. Gonze, *Comput. Mat. Science* **42**, 337, (2008).
- [111] B. Amadon, F. Lechermann, A. Georges, F. Jollet, T. O. Wehling, A. I. Lichenstein, *Phys. Rev. B* **77**, 205112 (2008).
- [112] E. Pavarini and E. Koch, *Phys. Rev. Lett.* **104**, 086402 (2010).
- [113] G. Wang, Z. Li, L. Zheng, and Z. Yang *Phys. Rev. B* **84**, 045111 (2011).
- [114] A. Kokalj, *J. Mol. Graphics Modelling*, 1999, Vol. **17**, 176–179. Code available from <http://www.xcrysden.org/>.
- [115] E. Pavarini and E. Koch *Phys. Rev. Lett.* **101**, 266405 (2008).
- [116] M. Cococcioni and S. de Gironcoli, *Phys. Rev. B* **71**, 035105 (2005).
- [117] M. Springer and F. Aryasetiawan *Phys. Rev. B* **57**, 4364 (1998).
- [118] T. Hashimoto, S. Ishibashi and K. Terakura *Phys. Rev. B* **82** 045124 (2010).

- [119] S. W. Cheong and H. Y. Hwang, Colossal Magneto-Resistance Oxides, edited by Y. Tokura, Monographs in Condensed Matter Science (Gordon and Breach, U.K., 2000) and references therein.
- [120] Y. Tokura and N. Nagaosa, *Science* **288**, 462 (2000).
- [121] C. Zener, *Phys. Rev.* **82**, 403 (1951)
- [122] J. Kanamori, *J. Appl. Phys.* **31**, S14 (1960).
- [123] J. B. A. A. Elemans, B. van Laar, K. R. van der Veen, and B. O. Loopstra, *J. Solid State Chem.* **3**, 238 (1971).
- [124] J. S. Zhou and J.B. Goodenough *Phys. Rev. B* **68**, 144406 (2003).
- [125] M. Baldini, D. Di Castro, M. Cestelli-Guidi, J. Garcia, and P. Postorino *Phys. Rev. B* **80**, 045123 (2009).
- [126] B. Vertruyen *et al.*, *Cryst. Eng.* **5**, 299 (2002).
- [127] J. Blasco *et al.* *Phys. Rev. B.* **66**, 174431 (2002)
- [128] M. C. Sanchez *et al.* *Phys. Rev. B* **73**, 094416 (2006).
- [129] D. Vanderbilt, *Phys. Rev. B* **41**, 7892 (1990).
- [130] R. Kovačik and C. Ederer *Phys. Rev. B* **81**, 245108 (2010).
- [131] S. L. Dudarev *et al.* *Phys. Rev. B* **57**, 1505 (1998).
- [132] W. E. Pickett and D. J. Singh *Phys. Rev. B* **53**, 1146 (1996).
- [133] V. I. Anisimov *et al.* *Phys. Rev. B* **65**, 172413 (2002).
- [134] V. I. Anisimov *et al.* *Phys. Rev. B* **81**, 075109 (2010).
- [135] A. Yamasaki, M. Feldbacher, Y.-F. Yang, O. K. Andersen and K. Held *Phys. Rev. Lett.* **96**, 166401 (2006).
- [136] K. Tobe *et al.*, *Phys. Rev. B* **64**, 184421(R) (2001);
- [137] A. Nucara *et al.* *Phys. Rev. B* **77** (6), 064431 (2008).
- [138] J. Rodríguez-Carvajal *et al.*, *Phys. Rev. B* **57**, R3189 (1998).
- [139] T. Hotta *et al.* *Phys. Rev. B* **60**, 22 (1999).
- [140] H. Zenia *et al.* *New Journal of Physics* **7** (2005) 257.
- [141] J. Farrell and G. A. Gehring *New J. Phys.* **6**, 168 (2004).

- [142] I. Solovyev, N. Hamada, and K. Terakura, Phys. Rev. Lett. **76**, 4825 (1996).
- [143] M. Baldini, V.V. Struzhkin, A. F. Goncharov, P. Postorino, and W. L. Mao Phys. Rev. Lett. **106**, 066402 (2011).